Adam Mickiewicz University Poznań

Faculty of Physics

Mgr Klaudia Żebrowska

Multifunctional nanocarriers based on polydopamine for biomedical applications.

Doctoral dissertation conducted at NanoBioMedical Center
under the supervision of dr hab. Emerson Coy, prof. UAM

Supporting supervisor:
dr inż. Bartosz F. Grześkowiak

Poznań, 2022

Acknowledgments

Publications

1. **K. Żebrowska**, E. Coy, K. Synoradzki, P. Torruella, S. Jurga, R. Mrówczyński, Facile and Controllable Growth of β-FeOOH *Nanostructures on Polydopamine Spheres*, The Journal of Physical Chemistry B, 2020

2. A. Jędrzak, B. Grześkowiak, **K. Golba**, E. Coy, K. Synoradzki, S. Jurga, T. Jesionowski, R. Mrówczyński, *Magnetite Nanoparticles and Spheres for Dual Therapy of Hepatocellular Carcinoma in vitro*, International Journal of Nanomedicine, 2020

3. **K. Żebrowska**, M. Grabowska, E. Coy, K. Rolle, B. F. Grześkowiak, *Multifunctional polydopamine nanoparticles for combined chemo-/photo-/gene therapy of glioblastoma multiform* (under preparation)

Table of content

Abstract

The growing incidence of cancer is a problem for modern medicine since the therapeutic efficacy of applied modalities is still unsatisfactory. Chemotherapy is a systemic method affecting both normal and cancer cell, therefore, it can induce side effects. Cancer nanomedicine development aims to improve the efficiency of tumor treatment. Nanoparticles (NPs) are used to deliver and release therapeutic agents in a controlled manner. The large surface area of NPs allows both efficient drug loading and small molecule attachment, like ligands or antibodies, for targeting cancer cells. Furthermore, a method that is still getting attention is photothermal therapy (PTT). The use of PTT assisted by nanoparticles and combining it with various modalities is of great interest in the field of modern nanomaterials for cancer treatment. This thesis presents three types of multifunctional carriers based on polydopamine (PDA) for combined cancer therapy. The carriers can be distinguished into two main parts: preparation of the drug delivery systems and their biological application. For the development of carriers, different properties of PDA were exploited. This work shows that PDA is a highly biocompatible and suitable substrate for further functionalization with dendrimers, doxorubicin loading and RNA attachment, using many functional groups in the PDA structure. Due to the chelating properties of PDA, it is demonstrated that unique metallic structures can be directly grown on the surface of NPs. Finally, it is shown that strong adhesion of PDA can be used to encapsulate hydrophobic drugs and molecules, like curcumin, which may support the efficiency and therapeutic action of other chemotherapeutic agents. Simultaneously, a detailed biological investigation of cytotoxicity and therapeutic efficiency of all obtained drug delivery systems on hepatocellular and glioblastoma cancer cells is shown.

Keywords: polydopamine, dendrimers, iron structures, drug delivery, doxorubicin, curcumin, tenascin C, combined therapy, photothermal therapy, gene therapy

Streszczenie

Rosnąca zachorowalność na raka jest problemem współczesnej medycyny, ponieważ skuteczność terapeutyczna stosowanych metod jest wciąż niezadowalająca. Chemioterapia jest metodą ogólnoustrojową wywołującą wiele skutków ubocznych, gdyż wpływa ona zarówno na komórki nowotworowe, jak i na komórki prawidłowe. Rozwój nanomedycyny onkologicznej ma na celu poprawę jakości i skuteczności leczenia nowotworów. Nanocząstki (NPs) są wykorzystywane do dostarczania i uwalniania środków terapeutycznych w sposób kontrolowany. Duża powierzchnia nanocząstek umożliwia zarówno skuteczny załadunek leków, jak i przyłączanie małych cząsteczek, takich jak ligandy lub przeciwciała, w celu ukierunkowania ich na komórki nowotworowe. Ponadto metodą, która wciąż przyciąga uwagę, jest terapia fototermiczna (PTT). Wykorzystanie PTT wspomaganego nanocząstkami cieszy się dużym zainteresowaniem w dziedzinie nowoczesnych nanomateriałów do leczenia nowotworów. Praca opisuje otrzymywanie wielofunkcyjnych nanonośników opartych na polidopaminie (PDA) oraz ich zastosowanie biologiczne. Nośniki zostały otrzymane poprzez wykorzystanie różnych właściwości PDA. W pracy pokazano, iżże PDA jest biokompatybilnym substratem odpowiednim do dalszej funkcjonalizacji dendrymerami jak również załadunku doksorubicyny i przyłączania RNA, dzięki obecności wielu grup funkcyjnych w jego strukturze. Zdolność PDA do chelatowania jonów metali, wykorzystano do uzyskania unikalnych struktur metalicznych bezpośrednio na powierzchni NPs. Ostatecznie pokazano, iż dzięki silnym właściwościom adhezyjnym PDA może być stosowany do pokrywania leków hydrofobowych i cząsteczek, takich jak kurkumina, które mogą wspierać działanie innych środków chemioterapeutycznych. Równolegle do otrzymywania nośników prowadzona była ich szczegółowa analiza biologiczna pod względem oceny cytotoksyczności i efektywności terapii na komórkach nowotworu wątroby i mózgu.

Słowa kluczowe: polidopamina, dendrymery, sturktury żelaza, dostarczanie leków, doksorubicyna, kurkumina, tenascyna C, terapia łączona, terapia fototermiczna, terapia genowa

Abbreviation list

CA – citric acid

CUR – curcumin

DAPI - 4',6-diamidyno-2-fenyloindol

DD – PAMAM dendrimers

DMEM - Dulbecco's Modified Eagle Medium

DMSO - dimethyl sulfoxide

DOPA – dopamine

DOXO – doxorubicin

EE % - encapsulation efficiency

EELS – electron energy loss spectra

ELNES – energy loss near edge structure

FBS - fetal bovine serum

FTIR – furrier transform infrared

HR-TEM – high resolution transmission electron microscopy

LC % - loading capacity

MEM - Modified Eagle Medium

MTT - methylthiazoyldiphenyl-tetrazolium

NBMC – nanobiomedical center

NIR – near infrared

NPs – nanoparticles

O/N – over night

PBS – phosphate-buffered saline

PDA – polydopamine

PT – photothermal

PTT – photothermal therapy

ROS – reactive oxygen species

rpm - rounds per minute

RT – room temperature

TEM – transmission electron microscopy

TN-C – tenascin C

WST-1 - 5-(2,4-disulfophenyl)-2-(4-iodophenyl)-3-(4-nitrophenyl)-2H-tetrazolium

ξ – zeta potential

I. Introduction

1. State of the art

1.1.Nanotechnology

The definition of nanotechnology contains the design, development and use of materials with at least one dimension in the nanoscale. Due to their limited size, these materials can be designed to provide the required physical, biological, or chemical properties. This means that size manipulation changes the properties of the material. Nanoscale is placed between 1 nm to 100 nm, which is defined between atomic distances (10^{-9} m) and bulk (10^{-7} m). Due to the fact that materials at the nanoscale can exhibit unique properties previously expressed in atoms or bulk, it makes it a promising field of research and creates new scientific discoveries.

Nanostructures can be obtained using mechanical, chemical, or biological synthesis by two main methods. The first one is connected with Richard Feynman and is called bottom-up method. In this approach, the production of the material is based on the self-organization of atoms and particles at the molecular level. On the other hand, the so-called top-down method involves the miniaturization of larger structures into nanosized particles using techniques such as melting or milling. The choice of the most suitable method depends on the possibilities of development and the required properties of nanomaterials.[1]

The classification of the nanostructures is based on the number of dimensions in which their size is measured. It can be distinguished in:

- Three dimensions: dimensions being greater than 100 nm, but are made of multiple nanoscale building blocks

- Two dimensions: two dimensions are on the microscale and one dimension is at nanoscale, here belongs Van Der Waals materials. nanofilms, nanocoatings, and nanolayers

- One dimension: one dimension greater than 100 nm, here belongs nanofibers, nanorods, and nanotubes

- Zero dimension: all dimensions are less than 100 nm, here belongs points nanomaterials like quantum dots, hollow spheres, nanolenses, core shell quantum dots. [2,3]

1.1.1. Nanomedicine

Nanotechnology applied in medicine is a fully interdisciplinary topic. Nanomedicine depends on combining different fields of science like physical, chemical, biological, or medical science with engineering, pharmacy and technology. In the end, the true value of obtained material is based on the best solution between its medical utility and potential adverse effects. The advantages will be different for physicists, chemists and biologists. In general, nanomedicine can be summarized as the science and technology of diagnosing, treating and preventing disease and improving human health using nano-scale materials. Additionally, the progress of nanomedicine development is determined by research collaboration, patenting, commercialization, business development and technology transfer in different application areas. [4]

Researchers are motivated to develop suitable material by administering drugs and therapeutic agents that affect both healthy and diseased cells. For this reason, it is necessary to develop a drug delivery system able to transport a safe therapeutic agent, overcome potential physiological barriers (i.e. blood-brain barrier) and enter diseased cells. The development of targeted delivery systems, will reduce the side effects and enhance therapeutic agents' efficacy and safety. Hence, one of the fastest-growing fields of

17

nanotechnology in medicine are drug delivery systems that modify *in vivo* kinetics of the therapeutic factors.

The use of nanoparticles in targeted drug delivery improved the uptake of poorly soluble drugs, targeting factors to specific cells, and drug bioavailability. [5] The difference between untargeted and targeted drug delivery systems is shown in **Figure 1**. Targeted carriers can enter the specific diseased cells (blue cell) and deliver therapeutic agents without side effects on healthy cells (green cell) (**Figure 1B**). Untargeted carriers can be absorbed by both types of cells and cause an inadvisable reaction in the whole body (**Figure 1 A**). An example of untargeted therapy is traditional chemotherapy. Some anti-cancer drugs have been successfully delivered using nanomaterials, i.e. paclitaxel, doxorubicin, 5-fluorouracil, and dexamethasone. These drug-loaded carriers could release higher doses of the drug for a prolonged period of time only in cancer cells.
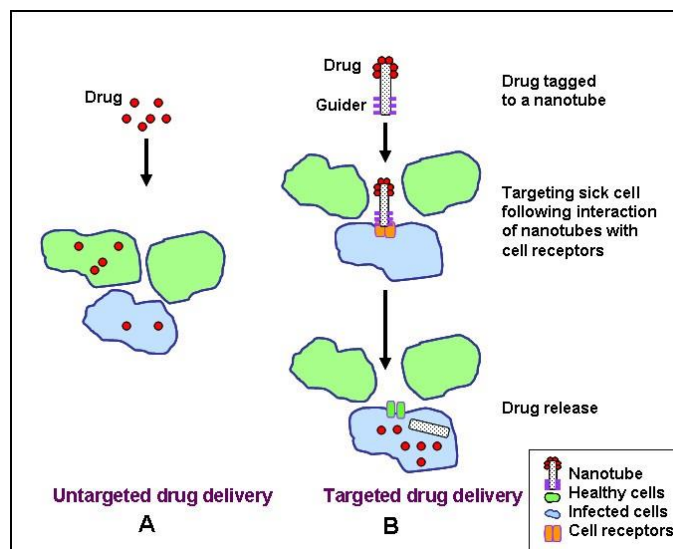
Figure 1. Image showing **A** untargeted and **B** targeted delivery of the drug to the healthy and diseased cells. [5]

Going further, nanoparticle based drug delivery systems (nanocarriers) can be classified by their generation according to the number of exhibited functions. The first

generation of nanocarriers means that the product is focused on one function i.e., targeting, while the higher generation nanocarriers (two or three) exhibits at least two functions i.e., targeting, delivery and imaging. Higher generation materials are characterized by multifunctionality, and they can overcome multiple physiological barriers.

The effectiveness of drug delivery systems is connected with their small size, biocompatibility, controlled release of the drug in time and modification of drug pharmacokinetics and biological distribution. The biggest issue to overcome in chemotherapy is developing of resistance to multiple anticancer drugs (MRD) in some tumor cells. MDR develops when cancer cells begin expressing a protein known as p-glycoprotein. This protein is capable of pumping anticancer drugs out of the cell. Research shows that nanoparticles may be able to introduce anticancer drugs into cells without triggering the p-glycoprotein pump.[6] The use of nanocarrier provides already known therapeutics with new possibilities and expand their potential thanks to the nanoscale.

In summary, from the pharmaceutical point of view, the greatest advantages and benefits obtained by using nanocarriers in drug delivery systems include:

➢ Improving the bioavailability of hydrophobic drugs

➢ Protection of drugs in a biological environment

➢ Controlling drug release in specific conditions

➢ Time extension of drug circulation in a specific targeted tissue

➢ Transporting of drugs by endocytosis through the cell membrane

➢ Inhibition of efflux pumps

➢ Targeted delivery of drugs by receptors

➢ Reduction of toxicity and side effects

➢ Biocompatibility/ biodegradability

➢ High efficiency of drug loading

➢ Extended physico-chemical stability of drugs

Furthermore, the use of nanotechnology in medicine could have economic value for drug manufacturers. Drug delivery systems give the possibility to reduce time-to-market, extend the economic life of proprietary drugs, and generate new sources of income. Nevertheless, all new drug delivery systems must be approved by governmental agencies like Food and Drug Administration (FDA), European Medicines Agency (EMA), World Intellectual Property Organization (WIPO), Patent and Trademark Office (PTO) based on the preclinical development stage/ clinical trials.[4]

1.1.1.1.Nanoparticles in nanomedicine

Common materials and structures used as a drug delivery system can be classified into three important groups: polymeric, inorganic and lipid-based nanoparticles (**Figure 2**). [7] Which type will be the best for delivery of a specific therapeutic agent depends on the required properties like: chemical nature, shape, morphology and the possibility of surface modifications. The large surface-to-volume ratio is the common property of all nanomaterials used for drug delivery. Many unique physical, chemical and biological properties of nanomaterials originate from these two features. The perfect size of NPs for the drug delivery system should be large enough to avoid first-pass kidney elimination and small enough to take advantage of the EPR (Enhanced Permeability and Retention) effect, so the range can be defined between 20 nm to 200 nm. [8]
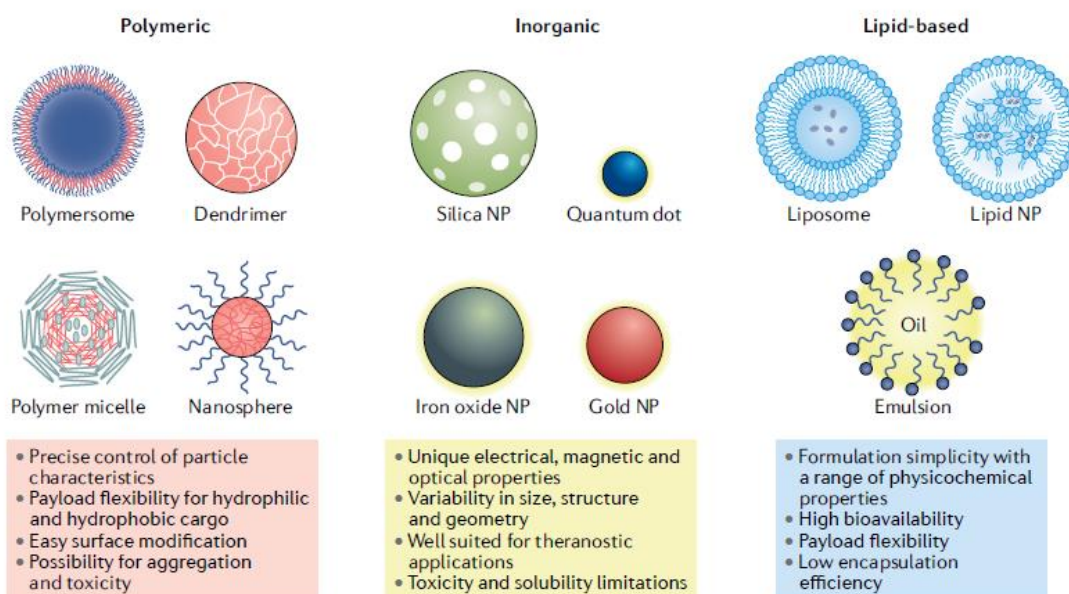
Figure 2. Three most common groups of carriers using in nanomedicine as drug delivery systems. [7]

Inorganic NPs are represented mostly by: metal nanoparticles (i.e. gold), iron oxides, silica and quantum dots. They can take spherical shapes, nanorods, nanocubes, triangles, stars, polyhedrons, nanoshells, nanocages, and other morphologies. Depending on their shape, they can be applied differently, e.g. anisometric NPs such as nanorods easily permeate the cell membrane due to their large aspect ratio and can work very well as drug carriers. [9] Inorganic NPs are especially suited for use in diagnostics, imaging, and photothermal therapy because of their magnetic, radioactive, or plasmonic characteristics. Most have good biocompatibility and stability and fill niche applications that require properties unattainable by organic materials. However, low solubility and toxicity issues, particularly in formulations utilizing heavy metals, limit their practical applicability in clinical research. [9–13]

Lipid-based NPs consist of liposomes, lipid NPs and oils. Phospholipids, which can form unilamellar and multilamellar vesicular structures, make up the majority of the NPs in liposomes. Liposomes can entrap hydrophilic and hydrophobic substances in the same

system, express low toxicity, and allow controlled drug release. The size, surface charge, lipid composition, number of lamellae, and surface modifications (with ligands or polymers) of lipid-based NPs, can be changed during manufacture. However, despite these advantages, lipid systems can still be limited by low drug loading and biodistribution. [14–16]

The polymeric group consist of micelles, solid polymeric NPs and dendrimers. They can be synthesized using natural or synthetic polymers, which allows for a wide variety of possible structures and characteristics. They can be designed to enable precise control of multiple NP features and are good delivery vehicles because they are biocompatible and have simple formulation parameters.

Micelles are formed by amphiphilic block copolymers. These polymers have hydrophobic and hydrophilic parts, which self-assemble in water and at temperature-specific critical micelle concentrations. The big advantage of micelles is their ability for prolonged blood circulation, allowing controlled release of pharmaceuticals over time. [17]

Polymeric nanoparticles are colloidal particles in size between 10 nm to 1000 nm. Their shape can be spherical, branched or core-shell. For their synthesis, synthetic polymers can be used, i.e., polycaprolactones, polyacrylates or copolymers polylactide-polyglycolide, as well as natural polymers i.e., gelatin alginate, collagen or chitosan. Drugs are either entrapped or chemically conjugated to the core of these nanoparticles but can also be covalently bonded to the surface or physically adsorbed. The solid nature of polymeric nanoparticles ensures high stability and allows for drug release in a controlled manner *via* diffusion or degradation of the polymer. The development of polymer science resulted in the production of stimuli-sensitive polymers, which physicochemical properties can change in response to environmental signals. The environmental signals can be: physical factors such as temperature, ultrasound, light, electricity and mechanical stress;

chemical factors i.e. pH and ionic strength; and biological factors, like enzymes and biomolecules. Due to this, the stimuli-sensitive polymeric carrier can be designed for a specific type of cancer cells and applications. Polymeric carriers can be categorized based on the drug incorporation mechanism. The first category is drug conjugation using covalent chemistry (i.e., linear polymers). The second includes hydrophobic interactions between drugs and carriers (i.e., polymeric micelles and block copolymers). [18]

Dendrimers are produced in artificial conditions and characterized by a structure similar to a tree. The diameter grows incrementally in steps, between 1 nm and 10 nm. Their biocompatibility and pharmacokinetics can be easily controlled by chemical structure and presence of functional groups on their surface. Due to the globular structure and cavities, it is possible to encapsulate the drug inside and further provide controlled release from the core. Additionally, it is possible to use covalent bonding or electrostatic interactions to load a drug also on the surface of dendrimers. The functional groups can also be used to attach other ligands to allow targeted drug delivery to specific cancer cells. Dendrimers can be synthesized in two ways, starting from the core or peripheral groups. The first method requires large numbers of steps and equivalents reaction on one single molecule. This synthesis is more complicated because of difficulties with the purification after each step. The second method starts in periphery groups of dendrimer and ends at the core. In this case, each step can be purified separately. A general advantage is that many different types of dendrimers are commercially available. [18,19]

1.1.2. Polydopamine

Polydopamine (PDA) is a polymer easily obtained by the oxidation of dopamine and was first described in 2007. [20,21] It is composed of indole and dopamine units in various oxidation states and, to a lesser extent, of pyrroles. It adheres to all types of

surfaces, even under water, due to its abundant catechol moieties assisted by amino groups. Additionally, PDA exhibits a widespread reactivity to nucleophiles and electrophiles, allowing the linkage of various entities renders. Because of that, PDA found wide applications in biology, biomedicine, membranes, catalysis and materials sciences. [22–24]

However, the detailed structure of PDA is still unknown and represents a wide field of research. The structure depends strongly on the method of preparation and whether it forms a coating on a surface or particles/aggregates in suspensions. [25] Initially, the synthesis was performed only in an alkaline solution, but based on literature reports, the possibilities were developed in many directions. Therefore, the elucidation of the structure of PDA is a long-lasting venture that has not come to its definite end yet and most likely cannot be found out completely. Until now, PDA structures were investigated using: solid nucleic magnetic resonance (NMR), mass spectrometry, X-ray crystallography, Fourier-transform infrared (FTIR) spectroscopy, UV/Vis spectroscopy, contact angle determination, atomic force microscopy (AFM), and chemical degradation, e.g. in alkaline hydrogen peroxide. [26] It was found that PDA is a mix of oligomers with different chain lengths (trimers and tetramers are abundant) and the addition of various monomer units. Very recent findings concluded that PDA-coatings have a predominantly polymeric nature. [27] Much more can be said about the properties of PDA that have found wide application in many fields of science (**Figure 3**).

The possibility to cover different types of materials i.e. polymers, ceramics, metals to improve their properties and stability or to use it as a template for further functionalization.

The presence of many functional groups on the surface of PDA enables a very easy modification.

A wide range of applications in biomedicine due to its high biocompatibility.

PDA as a catechol-like material, exhibits excellent chelating properties for binding various types of metal ions

The wide range of absorption leading to exchange of infrared laser light (808 nm) into heat.

Figure 3. The most valuable properties of PDA for biomedical applications.

One of the characteristic properties of PDA is a wide range of light absorption. It was described in a range from UV to infrared. PDA takes the form of intense and dark black solids insoluble in most solvents. It was found that PDA can exchange the absorbed infrared light into heat, which found application in the photothermal therapy of cancer and photocatalysis. PDA is a strong photothermal agent and its main advantage over other photothermal agents is its superior light-to-heat conversion efficiency (about 40%) at 808 nm. [28] In material science, PDA has found photocatalytic application e.g. in sunscreen gels or as a protective layer from UV light. [29]

Another important ability of PDA is the possibility to cover almost all kinds of surfaces. [30] This adhesive property is attributed to the catechol and aminoethyl groups in the PDA structure. Additionally, PDA layers/coverings, as well as particles, provide good hydrophilicity. It is an advantage, especially in the case of biomedical applications. It allows for the easy functionalization of PDA products in nontoxic solvents. Going further, PDA can interact with substrates by non-covalent interactions like hydrogen bonding, π–π

stacking, charge transfer, and metal coordination or chelation. This is another aspect proves the easy functionalization of PDA surface. It also shows that PDA is an excellent template for further modification of materials. A covalent bonding with the PDA surface is possible by exploiting the Michael-like or carbonyl reactivity. [26,31,32]

From a magnetic point of view, PDA has paramagnetic properties. It is the result of stable π-electron free radical species. Single-line electron paramagnetic resonance (EPR) spectra were obtained with a g-factor of about 2. This is an indication of an irregular, cross-linked polymer network with mixed bonding arrangements and radicals localized at quinone residues. The radical property enables PDA to act as a radical trap and makes it interesting as a therapeutic antioxidant as well as for EPR spatial 2D imaging. [33]

1.2. Application of polydopamine nanoparticles in cancer therapy

Cancers are one of the leading causes of death worldwide and a major civilization disease of our time. Based on the example of liver cancer, the occurrence of cancers increases every year. In 2012, it was ranked 5th in the classification of the most common and deadly cancers. In just six years, it had gone up to the 4th position, according to the World Health Organization data from 2018. Development in the field of nanomedicine is driven by the search for a more effective cancer therapy that does not cause undesirable effects on the body. Given the high risk of cancer disease incidence and mortality, researchers around the world have been struggling to develop more accurate, faster diagnostic strategies and effective therapies to fight cancer. The most traditional cancer therapies include chemotherapy, radiotherapy, and surgery (**Figure 4**), in which patients may suffer from severe side effects and unsatisfactory treatment outcomes. These treatment failures have led to the development of precise and more effective cancer treatment strategies. The emerging therapies in cancer treatment include, but are not

26

limited to, immunotherapy, gene therapy, photodynamic therapy (PDT), and photothermal therapy (PTT), which have improved or can potentially improve therapeutic outcomes.

Figure 4. Graphic showing the most common cancer treatment possibilities. [34]

1.2.1. Chemotherapy

Chemotherapy is a method recognized and used in oncological treatment for many years. It is based on the use of pharmacological agents to destroy or inhibit the development of cancer cells. Drugs used in chemotherapy are called cytostatics and they can be natural and synthetic substances. An appropriate chemotherapy regimen is used for each type of cancer and its development stage. Usually, several treatment regimens for a given tumor are selected in the right order. Treatment of neoplastic diseases is basically a combination therapy. Chemotherapy is therefore used in combination with surgery, radiotherapy or hyperthermia where this is justified and possible.

In research, doxorubicin (DOXO) is often used as a model drug because of its wide field of treatments for various types of cancer, both solid tumors and haematological malignancies, including breast, bile ducts, prostate, uterus, ovary, oesophagus, stomach and liver tumours, childhood solid tumors, osteosarcomas and soft tissue sarcomas,

Kaposi's sarcoma, as well as acute myeloblastic and lymphoblastic leukaemia. [35,36] One of the major mechanism underlying the antineoplastic activity of DOXO relates to its ability to intercalate into the DNA helix and/or bind covalently to proteins involved in DNA replication and transcription. The uptake of DOXO into cancer cells appears by simple diffusion through the cell membrane (**Figure 5**). [37] Further, it binds with high affinity to the proteasome in the cytoplasm (step 1) as a transporter. In this complex, DOXO is delivered into the nucleus through nuclear pores (step 2). DOXO binds to DNA in the nucleus due to its higher affinity for DNA than for proteasome (step 3). Second pathway of DOXO mechanism of action is interaction with mitochondria and binding to cardiolipin. In this case, it blocks the binding of mitochondrial creatine kinase to mitochondrial membranes. In mitochondria, DOXO leads to an increase in reactive oxygen species (ROS) production. Doxorubicin is one of the most potent antineoplastic drugs prescribed alone or in combination with other agents, while remaining the compound with the broadest spectrum of activity in its class. [35]
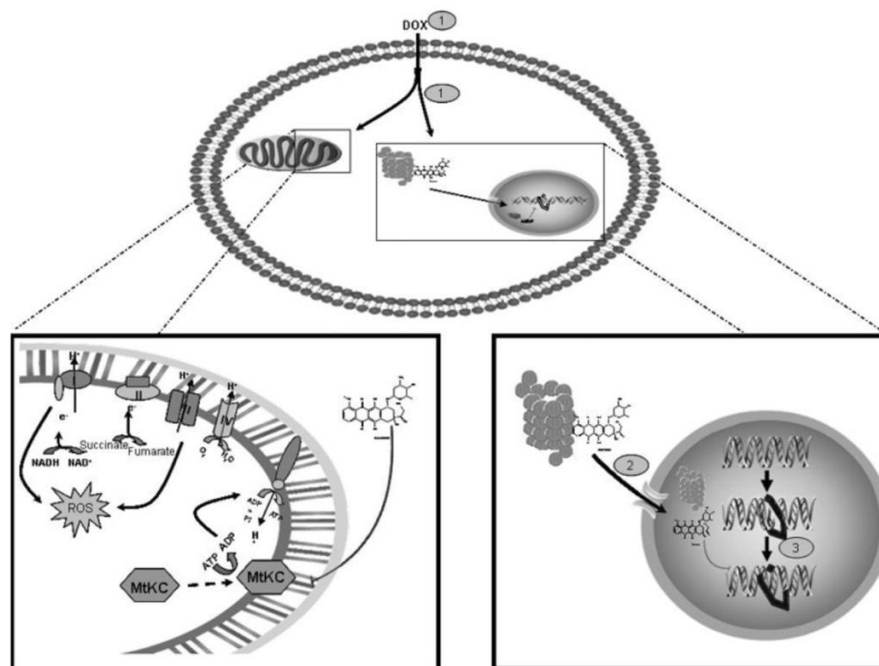

Figure 5. Image showing mechanism of action of doxorubicin in cells in mitochondria (left side) and nucleus (right side). [35]

The therapy with DOXO can be improved by using curcumin (CUR). Curcumin represents only 2−8% of most turmeric compounds. It exhibits e.g., antioxidant, anti-inflammatory, antimicrobial, neuroprotective, anticancer drug supporting, and chelating properties (**Figure 6**). [38] The crystalline orange-yellow powder is an active polyphenolic phytochemical and has been widely used in medicinal purposes for centuries in India and South Asia. [39] Curcumin induces cell cycle arrest and apoptosis in senescent cancer cells to make them more sensitive to chemotherapy with DOXO. [40] In addition, curcumin improves anti-tumor activity of DOXO by enhancing its accumulation in cancer cells. P-glycoprotein (P-gp) is a membrane transporter that undergoes up-regulation in cancer cells to export the cytotoxic agent out of cell. By down-regulation of P-gp, curcumin increases the accumulation of DOXO in cancer cells, increasing its anti-tumor activity. [41,42] ATP binding cassette subfamily B member 4 (ABCB4) is another transporter that ensures the resistance of cancer cells to chemotherapy. Notably, curcumin also inhibits the activity of ABCB4 in sensitizing cancer cells to chemotherapy with doxorubicin. [43,44] These studies are in line with the fact that curcumin can be applied as an adjuvant in chemotherapy. The preventive and therapeutic effect of curcumin was shown in various types of cancer. It has been demonstrated that curcumin prevents cancer formation and spreading as well as reduces tumor size. [45]
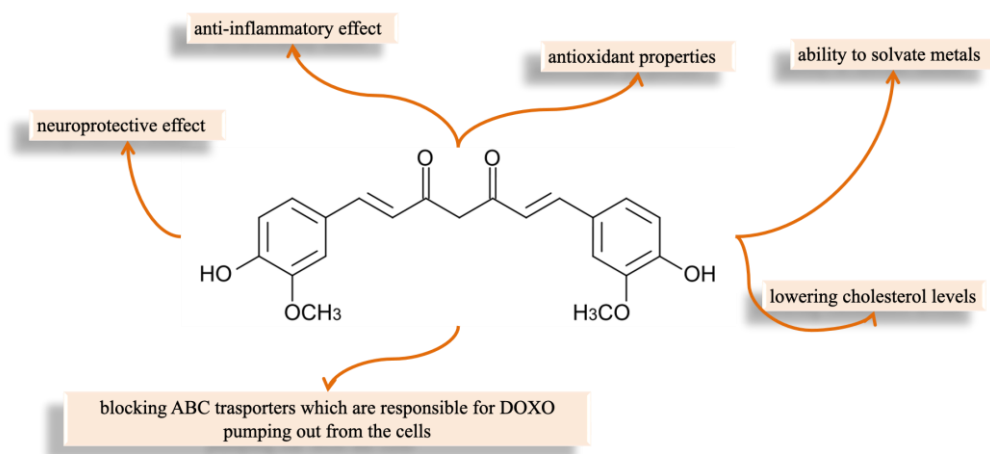
Figure 6. Curcumin chemical structure and some examples of its characteristic properties.

As shown in the literature, polydopamine is very often used as a drug delivery system component. PDA is mainly used in the delivery of DOXO (as a model drug) and the simultaneous delivery of different drugs or therapeutic agents. This is possible due to the ease of PDA surface functionalization or its strong adhesive properties for encapsulating hydrophobic drugs creating core-shell NPs. The first articles presenting loading of CUR in core-shell PDA NPs appeared in 2019. In this approach, the insolubility of CUR in water was used to encapsulate it inside the NPs and deliver the natural form of CUR to the cells. [46,47] PDA can also be used to deliver different chemotherapeutic drugs like paclitaxel. Zhao *et al.* encapsulated paclitaxel in PDA NPs for osteosarcoma targeted therapy. [48] Chemo-photothermal application in cancer treatment has also been found in scaffolds. Meng *et al.* created a drug delivery system based on PDA, CUR and silk fibre for bone tumor therapy. In this case, PDA improved hydrophilicity and mechanic strength of scaffold. [49]

1.2.2. Gene therapy

Gene therapy is an experimental treatment method of cancer, genetic diseases, and infectious diseases by introducing genetic material (DNA or RNA) into cells to induce a specific therapeutic effect. Several mechanisms used in gene therapy can be distinguished: (1) replacing a disease-causing gene with a correct copy of the gene, (2) inactivating a disease-causing gene that is not functioning properly, (3) introducing a new or modified gene into the body to help treat disease. In gene therapy, therapeutic genetic material packaged into a delivery vehicle can be either directly injected into the patient (*in vivo*) or patient-derived cells modified outside the body and readministered to the patient (*ex vivo*). The most frequently studied types of gene delivery carriers are:

- Viral vectors: have a natural advantage which is the ability to deliver genetic material into cells by infection. Viruses can also deliver the gene-editing tools to the nucleus of the cell. Gene therapy with viral vectors has been successful, but it does carry some risk. In general, viruses are modified to remove their ability to cause disease. However, they can trigger a dangerous immune response. In addition, vectors that integrate the genetic material into a chromosome can cause errors that lead to the development of cancer.

- Nanocarriers: nanoparticles can be designed with specific characteristics to target particular cell types. Nanoparticles are less prone to induce immune reactions than viral vectors and are easier to design and modify for specific purposes. [50–53]

Tumor cells express preferentially a number of surface markers that may be exploited as therapeutic targets in gene therapy. One of the interesting candidates that contribute to tumor development is an extracellular matrix glycoprotein tenascin C. It is one of the multimeric peptides belonging to the group of proteins called tenascin. Tenascin

C may have pathological or physiological functions depending on the circumstances and the type of cell in which it is expressed. The expression of tenascin C varies in tissues and depends on the organism's stage of development. The change in its expression is radical in pathological conditions such as cancer, colitis, synovitis, tendon degeneration and interstitial pneumonia. The expression level of tenascin C has been correlated with many malignant types of cancer, including colon, breast, lung, prostate, melanoma, fibrosarcoma, squamous cell carcinoma, and bladder tumor, as well as glioma. Moreover, tenascin C has been shown to have a significant function in the spreading, adherence and proliferation of cells. Tenascin C is highly expressed and accumulated in the cells of the most aggressive brain tumor glioblastoma. [54,55] A down-regulation of TN-C by RNA interference (RNAi) is a very promising gene therapy strategy in cancer treatment. In this experimental approach developed by prof. Barciszewski's group from the Institute of Bioorganic Chemistry (Polish Academy of Sciences) in Poznań, double-stranded interfering RNA (dsRNA) with sequence homologous to TN-C mRNA was used to reduce TN-C expression in tumor cells resulting in the improvement of the therapy efficiency. [56,57]

PDA NPs are widely used in gene delivery because of their easily surface modification to attach nucleic acids. Wang *et al*. loaded siRNA onto mesoporous PDA NPs and inhibited the undesirable early release by overlaying with calcium phosphate. [58] Genes can be attached to the surface of NPs by the linker in the form of i.e. polyethyleneimine as shown by Zhang *et al*. Authors used polyethylene glycol-phenylboronic acid and polyethylenimine for gene attachment based on noncovalent binding and pH responsive release in cells. [59] Zhao *et al*. presented nanocomplex of PDA with DNAzyme and manganese as a degradable structure inside the cell enabling simultaneous gene/PT therapy and imaging.[60]

1.2.3. Photothermal therapy

Photothermal therapy (PTT) was first described in 2003 by Halas and co-workers. [61] PTT has found application as a highly controllable cancer treatment method. The biggest advantages of this therapy are low cost, good specificity, reduced patient pain, shorter treatment time, improved treatment effect, and reduced toxicity and slight side effects on normal tissues. [62]

Biomedical applications where both blood and soft tissues are highly permeable require considerably deeper penetration of near-infrared (NIR) light (**Figure 7**). In the NIR region, two biological transparency windows are located in the range of 650−950 nm (first NIR window) and 1000−1350 nm (second NIR window), with optimal tissue transmission resulting from low scattering and energy absorption, which ensures maximum radiation penetration through tissue and minimizing autofluorescence. The second region between 1000 nm and 1350 nm is recognized to offer more efficient tissue penetration relative to the first region when considering absorption and scattering effects in tissue. For example, haemoglobin has substantially lower absorption at the NIR wavelength, and blood is sufficiently transparent between 1000 and 1350 nm. Materials absorbing radiation in the NIR range are considered suitable agents for the photothermal cancer therapy. [63]

Figure 7. Graphical presentation of the photothermal therapy with the application of different nanomaterials and selection of the proper NIR wavelength using the first and second biological window of absorption. [64]

Photothermal therapy can induce cancer cell death in three ways. The first one leads to necrosis of the cells. Cell necrosis is an unscheduled process of cell death characterized by cytoplasmic expansion, severe organelle damage and plasma membrane rupture. It leads to the release of cell contents and inflammation. The second one is apoptotic cell death by inducing the changes of oxygen free radicals (ROS) and irreversible damage to cells and microvessels. It is characterized by oligonucleosomal DNA fragmentation, chromatin condensation, mitochondrial dysfunction, and translocation of the phosphatidylserine phospholipid to the outer part of the plasmatic cell membrane. Apoptosis is essential for ontogenetic development and adult tissue remodeling. It helps eliminate damaged, infected, or tumor cells. In contrast to necrosis, membrane integrity is preserved during apoptosis due to the presence of a number of molecules known as "eat me" signals in the plasma membrane of dying cells. Thanks to these signals, apoptotic bodies are rapidly cleared by phagocytic cells, including macrophages, epithelial and dendritic cells, avoiding the detrimental effects of necrosis. Moreover, although apoptotic cell death also induces an inflammatory immune response, the mechanism and consequences of this reaction are different than during necrosis. [65,66] The last one is cancer cell death caused by photodynamic stimulation of immunogenic cell death, which gives a number of effects and applications at a later stage. [67]

The schematic representation of the PTT mechanism occurring in some materials, is shown in **Figure 8** using the Jabłoński diagram. As a result of irradiation, excitation to the first excited singlet state is visible. The photosensitizer then moves to the most suitable energetic state of balance. The accumulated energy can be released mostly in a basic way as fluorescence, and it can relax to a more long-lived triplet state. This triplet can interact with molecular oxygen in two pathways, forming reactive oxygen species (ROS) and singlet oxygen, respectively. [68]
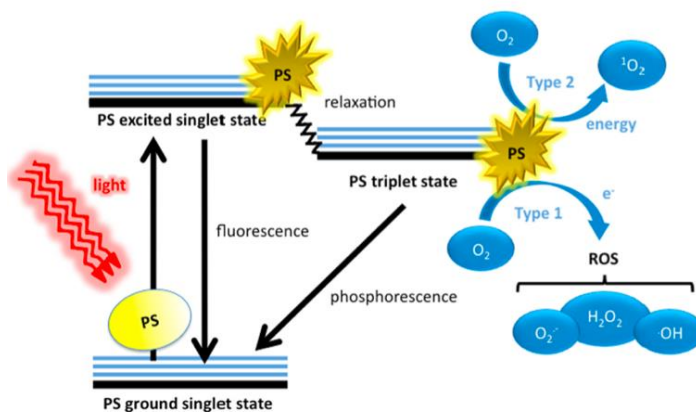
Figure 8. Schematic representation of PTT mechanism of a material based on energetic levels and possibilities of energy release included the biological effect. [68]

Photothermal therapy is based on the use of nanomaterials exhibiting abilities to absorb energy from photons and dissipate it in the form of heat, causing the death of cancer cells. Among various photothermal agents, two-dimensional nanomaterials are interesting candidates for PTT due to their special structure and unique properties. These materials exhibit plasmonic effects upon near-infrared light irradiation, which favors the conversion of light energy into thermal energy. [69,70]

As mentioned above, PDA exhibits a broad absorption spectrum encompassing the NIR region and a light-to-heat conversion efficiency of 40%. PDA can be easily combined with drugs such as DOXO *via* the π- π stacking, thus gaining the extra therapeutic modality. An example of PT properties combined with DOXO delivery was presented by Grześkowiak *et al*., where the authors show a substantial increase in drug release and reactive oxygen species (ROS) generation upon irradiation of PDA NPs, which triggers additional apoptotic mechanisms, thus reducing the cancer cell survival. [71] PDA can also be used as a support of other nanocarriers i.e. iron oxide, gold, and silica NPs to improve their absorption properties and, as a result, increase the emission of heat. Jędrzak *et al*. showed PDA-coated iron oxide nanomaterials for hepatocellular carcinoma treatment. The

use of PDA coating improved PT properties and biocompatibility of the carrier and allowed for further functionalization. [72] PT properties of PDA can be used in combination with photodynamic therapy, which was presented by Poinard *et al.* The authors showed the application of PDA with hydrophobic photosensitizer drug chlorin e6 (Ce6) for bladder cancer treatment. [73] In combination with Mn for MRI or gold NPs for optical imaging, PDA was used as theranostic material for PT therapy together with the imaging of NPs. [74,75] Maziukiewicz *et al.* used PDA to cover nanodiamonds that exhibited optical properties to track fluorescence in cells. The material was successfully delivered to glioblastoma cells with 40% higher efficiency than pure nanodiamonds and improved therapeutic effect due to the addition of laser irradiation. [76]

II.   Objectives and aims

The main aim of the thesis was to synthesize and characterize a new type of nanoparticles based on polydopamine as a potential smart drug carrier for the combined delivery of therapeutic agents and photothermal therapy of cancer cells. For this purpose, different advantages of polydopamine were used, such as: ease of functionalization, chelating properties, high adhesion to hydrophobic materials, and photothermal properties.

In order to distinguish each step needed to develop multifunctional nanomaterial using unique properties of polydopamine, specific goals were determined:

1. Synthesis of pure polydopamine nanoparticles of a specified size and determination of their physicochemical properties.

2. Investigation of the growth of iron structure on the pure polydopamine nanoparticles and determination of their physicochemical properties.

3. Development of the polydopamine coated curcumin core-shell type nanoparticles and determination of their physicochemical properties.

4. Assessment of the chemo/gene/PT therapy efficiency of modified polydopamine nanoparticles on glioblastoma cells.

5. Assessment of the cytotoxicity of iron structure coated polydopamine nanoparticles on hepatocellular carcinoma cells.

6. Assessment of the chemo/PT therapy efficiency of curcumin/polydopamine nanoparticles on glioblastoma and hepatocellular carcinoma cells.

III. Materials and Methods

2. Chemicals/ reagents/ materials

Dimethyl sulfoxide (DMSO), iron chloride (II) and (III), iron sulfate (II), iron acetylacetonate, sodium hydroxide, curcumin, polyamidoamine (PAMAM) dendrimers G 3.0, agarose, ethylenediaminetetraacetic acid (EDTA), Hank's Balanced Salt Solution (HBSS) buffer, Fetal Bovine Serum (FBS), phosphate-buffered saline (PBS) buffer (with or without Ca^{2+} and Mg^{2+}), antibiotic antimycotic solution (10000 units penicillin, 10 mg/ml streptomycin, 25 μg/ml amphotericin B), Tris(hydroxymethyl)aminomethane (TRIS) buffer, Muse Oxidative Stress Kit, Muse Annexin V and Dead Cell Assay Kit were purchased from Sigma-Aldrich. Dopamine hydrochloride was purchased from Alfa Aesar. Ethanol (99.6% purity) and acetone were purchased from Avantor Performance Materials Poland S.A. (formerly POCH S.A.). Fluorescent dyes (calceine AM, ethidium homodimer-1, Hoechst 33342, concanavalin A AlexaFlour 647 conjugate), 16% formaldehyde solution, trypsin-EDTA (0.25%) solution, cell media Dulbecco's Modified Eagle Medium (DMEM 4.5 g/l glucose, L-glutamine and 3.7 g/l sodium bicarbonate, w/o sodium pyruvate), Minimum Essential Medium Eagle (MEM 4.5 g/l glucose, L-glutamine and 3.7 g/l sodium bicarbonate, w/o sodium pyruvate) and Opti-MEM, sodium pyruvate (100 mM), non-essential amino acids solution (100X), MTT cell viability assay were purchased from ThermoFisher Scientific. DNA gel loading dye (6X) and nucleic acid stain Simply Safe were acquired from EurX. WST-1 Cell Proliferation Reagent was purchased from Takara Bio.

Double-stranded RNA (dsRNA) with a length of 200 nucleotides and a sequence homologous to tenascin-C (ATN-RNA) was obtained in cooperation with the Department of Molecular Neurooncology, Institute of Bioorganic Chemistry, Polish Academy of Sciences in Poznań. Sequence of ATN-RNA (US Patent US 8,946.400 B2):

5'-
CAAGCGACAGAGUGGGGUGAACGCCACCCUGCCAGAAGAGAACCAGCCAGU
GGUGUUUAACCACGUUUACAACAUCAAGCUGCCAGUGGGAUCCCAGUGUUC
GGUGGAUCUGGAGUCAGCCAGUCCCCUCUUCUGGACCGGGCGGAAGUCUCG
GGCGCU-3'

3'-
GUUCGCUGUCUCACCCCACUUGCGGUGGGACGGUCUUCUCUUGGUCGGUCA
CCACAAAUUGGUGCAAAUGUUGUAGUUCGACGGUCACCCUAGGGUCACAAG
CCACCUAGACCUCAGUCGGUCACCCCUCUUCUGGACCGGGCGGAAGUCUCGG
GCGCU-5'

3. Synthesis and functionalization protocols

3.1. PDA NPs with 100 nm diameter

200 mg dopamine hydrochloride was dissolved in 100 ml of Milli-Q water in a round-bottom flask. The solution was placed on a magnetic stirrer and heated up to 50 °C. Then, 0.7 ml of aqueous 1M NaOH solution was added at 48 °C, followed by stirring for 3 h. The particles were collected and purified by centrifugation (22 000 rpm, 20 min) and washed three times with Milli-Q water.

3.2. CUR@PDA NPs with a diameter below 100 nm

25 mg of curcumin was dissolved in a 50 ml mixture of 1:1 ethanol/acetone ratio in a flat-bottom flask. The solution was placed on a magnetic stirrer at RT. Then, 125 mg of dopamine hydrochloride and 100 ml of 10 mM TRIS buffer pH 8.5 were added to the flask. After the dissolution of dopamine in TRIS buffer, 0.7 ml of aqueous 1 M NaOH solution was added. Flask was covered with aluminum foil and left for 17 h. The particles

were collected and purified by centrifugation (22 000 rpm, 60 min) and washed three times with Milli-Q water.

3.3. CUR@PDA NPs with a diameter over 500 nm

25 mg of curcumin was dissolved in a 50 ml mixture of 1:1 ethanol/acetone ratio in a flat-bottom flask. The solution was placed on a magnetic stirrer at RT. Then, 125 mg of dopamine hydrochloride and 100 ml of 10 mM TRIS buffer pH 8.5 were added to the flask. Flask was covered with aluminum foil and left for 24 h. The particles were collected and purified by centrifugation (22 000 rpm, 20 min) and washed three times with Milli-Q water.

3.4. CUR@PDA NPs with a diameter around 350 nm

25 mg of curcumin was dissolved in a 35 ml mixture of 1:1 ethanol/acetone ratio in a flat-bottom flask. The solution was placed on a magnetic stirrer at RT. Then, 125 mg dopamine hydrochloride and 100 ml of 10 mM TRIS buffer pH 8.5 were added to the flask. Flask was covered with aluminum foil and left for 17 h. The particles were collected and purified by centrifugation (22 000 rpm, 20 min) and washed three times with Milli-Q water.

3.5. Iron ions deposition on PDA NPs

10 mg of PDA NPs were placed in 30 ml of a water/ethanol mixture at a ratio of 1:2 in a locked flat bottom flask. The solution was sonicated and placed on a magnetic stirrer at RT. During the mixing, 30 mg of $FeCl_2$ was added to the solution. The particles were collected, purified by centrifugation (22 000 rpm, 15 min) and washed three times with Milli-Q water after 24 h, 48 h, 120 h.

3.6. NPs functionalization with PAMAM dendrimers G 3.0

10 mg of NPs (PDA orc CUR@PDA) were placed in 30 ml of 10 mM TRIS buffer (pH 8.5) in a locked flat bottom flask. The solution was sonicated and placed on a magnetic stirrer at RT. During the mixing, 213.6 µl of polyamidoamine (PAMAM) dendrimers G 3.0 were slowly dropped into the solution. Next day, the particles were collected, purified by centrifugation (22 000 rpm, 15 min) and washed three times with Milli-Q water. The obtained nanoparticles were hereafter referred to as PDA@DD NPs or CUR@PDA@DD NPs.

3.7. Doxorubicin loading

1 mg of NPs (PDA@DD or CUR@PDA@DD) was dissolved in a tube containing 1 ml of doxorubicin solution at a concentration of 1 mg/ml in PBS buffer (pH 7.5) and placed in a thermal shaker at 25 °C for 24 h. Next, the particles were collected, purified by centrifugation (13 400 rpm, 4 min) and washed with PBS buffer to obtain a clear solution. PBS buffer was then collected after each centrifugation step and measured using UV-Vis spectroscopy. Each loading experiment was performed in triplicate. The obtained nanoparticles were hereafter referred to as PDA@DD@DOXO NPs or CUR@PDA@DD@DOXO NPs.

The encapsulation efficiency (EE %) and loading capacity (LC %) were calculated, respectively:

$$EE \% = \frac{total\ mass\ of\ added\ drug - mass\ of\ free\ non\ entrapted\ drug}{total\ mass\ of\ added\ drug} x\ 100\ \%,$$

$$LC \% = \frac{mass\ of\ entraped\ drug\ in\ nanoparticles}{mass\ of\ nanoparticles} x\ 100\ \%.$$

3.8. Doxorubicin release

The release of DOXO from the NPs (PDA@DD@DOXO or CUR@PDA@DD@DOXO) sample was tested in three different buffers: citric acid (CA) pH 4.5, CA pH 5.5, and PBS pH 7.5. 1 mg of NPs was dissolved in a tube containing 1 ml of respective solutions with different pH and placed in a thermal shaker at 37 ˚C (human body temperature) for 1 h, 2 h, 3 h, 4 h, 5 h, 6 h, 24 h and 48 h. The particles were then collected by centrifugation (13 400 rpm, 4 min) and supernatant was measured using UV-Vis spectroscopy. All measurements were performed in triplicate.

3.9. Curcumin content in CUR@PDA particles with a diameter over 300 nm

After synthesis of CUR@PDA NPs, particles were separated by centrifugation at 22 000 rpm for 15 min, and the supernatant was placed in the flask for UV-Vis measurements. The particles were washed three times with Milli-Q water by centrifugation (22 000 rpm, 20 min), and their mass concentration was determined. The encapsulation efficiency (EE %) and loading capacity (LC %) were calculated using the formulas presented above.

3.10. Curcumin content in CUR@PDA particles with a diameter below 100 nm

1 mg of CUR@PDA NPs was dissolved in a tube containing 1 ml of ethanol and placed on vortex mixer for few minutes. Next, the particles were collected by centrifugation (13 400 rpm, 5 min) and washed with ethanol to obtain a clear solution. Ethanol was then collected after each centrifugation step and measured using UV-Vis spectroscopy. The encapsulation efficiency (EE %) and loading capacity (LC %) were calculated using the formulas presented above.

3.11. Curcumin release

The release of CUR was investigated in different solutions: CA buffers (pH 4.5 and 5.5), PBS buffer (pH 7.5), TRIS buffers (pH 8.5 and 9.5), PBS buffer (pH 7.5) with 10% SDS, and 1:1 water/ethanol mixture. 1 mg of CUR@PDA NPs was dissolved in a tube containing 1 ml of respective solutions mentioned above and placed in a thermal shaker at 37 °C for 1 h, 2 h, 3 h, 4 h, 5 h, 24 h and 48 h. The particles were then collected by centrifugation (13 400 rpm, 5 min) and supernatant was measured using UV-Vis spectroscopy. All measurements were performed in triplicate.

3.12. Attachment of dsRNA

1 µg of dsRNA was mixed with a series of PDA@DD NPs weight ratios (1:1, 5:1, 10:1, 15:1, 20:1, 30:1 PDA@DD NPs to RNA wt/wt ratio) in 50 µl of water and incubated for 30 min in RT. For biological assays, the water was replaced with Opti-MEM medium.

4. Physicochemical methods

4.1. TEM imaging and HR-TEM analysis

Transmission electron microscopy (TEM) is a common technique for characterizing nanostructures and providing information on their surface morphology and structure. The microscope column consists of electron gun generating (e.g., an electron beam from thermo-emission or field emission). Then the electrons are formed into a beam by the so-called magnetic lenses. The electron beam passes along the optical axis of the microscope and is directed to the condenser, where it is focused and directed at the specimen. The beam then falls on the screen, which allows for indirect observation of the tested specimen. Inside the electron microscope column, there must be a high vacuum. For this purpose, a vacuum system consisting of a rotary pump, ion diffusion pump or molecular pump connected to vacuum valves can be used. A vacuum in the microscope is

necessary to ensure the conditions conducive to the emission and free movement of electrons.

The biggest advantage of electron microscopy is the possibility to investigate the materials even with 1 nm resolution. The resolving power of an electron microscope is influenced by the wavelength of the radiation, which is regulated by the accelerating voltage and the diameter of the beam. Resolution in microscopy is limited to about ½ of the wavelength of the illumination source used to image the sample. The correlation between the voltage and wavelength is described by Louis de Broglie and the formula:

$$\lambda = \frac{h}{\sqrt{2meV}} \quad \text{where:}$$

λ is the wavelength of propagating electrons at a given accelerating voltage, h is Planck's constant (6.626 x 10^{-34} J seconds), m is the mass of an electron (9.1 x 10^{-31} kg), e is electron energy (1.6 x 10^{-19}) and V is accelerating voltage. Using this formula, the wavelength of electrons can be easily calculated when the microscope is operated, i.e. at 100 keV as 3.88 pm or 2.74 pm for 200 keV.

TEM is also able to provide insights into the chemical composition and structure of structural building materials. These methods use the electron beam and their interaction with matter to obtain much important information about the analyzed samples, e.g. a carrier catalyst. EELS is said to be a complement to energy dispersive X-ray spectroscopy (called EDX, EDS, XEDS, etc.), which is another common spectroscopy technique available in many electron microscopes. EDX is excellent at identifying the atomic composition of a material, is relatively easy to use, and is particularly sensitive to heavier elements, while EELS is more sensitive to light elements. The difference is mainly due to the difference in energy resolution between the two techniques (~1 eV or better for EELS, perhaps tens of eV for EDX) and the sensitivity of EELS to valence changes investigated elements. [77]

TEM images presented in this thesis were recorded on a Jeol ARM 200F high-resolution transmission electron microscope (HRTEM) (in cooperation with dr hab. Emerson Coy) and on a Jeol 1400 transmission electron microscope at the NBMC AMU. The typical sample preparation consisted of drop-casting the sample on a copper grid (typically Formvar/Carbon 200 mesh from Ted Pella) after 5–15 min of sonication and drying in a vacuum desiccator. Electron energy loss spectra (EELS) were collected in the same instrument, and energy loss near-edge structure (ELNES) analyses were performed in HyperSpy (in cooperation with dr Pau Torruella – University of Barcelona). The size of NPs was measured using ImageJ software.

4.2. UV-Vis measurements

A UV-vis spectrophotometer is a device that measures how much light is absorbed by a sample. The principle of the method is based on a light beam passing through a prism or a diffraction grating. The wavelength or its range is selected by passing the scattered light through the slit. The light passes through the sample in the cuvette and strikes the detector. The measured spectra are unique for each material. This means that it is possible to measure the so-called spectrometric fingerprint of the sample, depending on the substance contained in it.

Using a spectrophotometer, the concentration of a substance in a sample can be determined. The spectrophotometric determination of the concentration of a substance in a solution from the absorbance of the solution is based on the Beer-Lambert law:

$$A=kcl.$$

Beer Lambert's law determines the relationship between absorption (A) and three factors: concentration of a substance (c), the length of the path that the light travels through the sample (l, determined by the width of the measuring cuvette) and the extinction coefficient of this substance (k). According to this law, the intensity of the light transmitted

(transmittance) through the test solution decreases exponentially if each of the three factors is increased.

The measurements were performed using T60 UV-Visible Spectrophotometer. Samples were placed in a 1 cm square quartz cuvette (High Precision Cell cuvettes made of Quartz SUPRASIL with a 10 mm light path (Hellma Analytics)).

4.3. Photothermal and photostability experiments

Temperature measurements were performed in a 1 cm square quartz cuvette (High Precision Cell cuvettes made of Quartz SUPRASIL with a 10 mm light path (Hellma Analytics)). The distance between the cuvette and the laser was 10 cm. NPs were prepared in five different concentrations: 10 µg/ml, 25 µg/ml, 50 µg/ml, 75 µg/ml, and 100 µg/ml in a total volume of 1 ml of water. 1 ml of pure water was used as control sample. The cuvette was placed above a magnetic stirrer. A temperature sensor and a magnetic dipole were placed inside the cuvette to keep the NPs moving and avoid their sedimentation. The temperature was measured at 10 s intervals over 10 min under irradiation with 808 nm wavelength laser light (Changchun New Industries Optoelectronics Tech. Co., Ltd., China) and laser power of: 3 W, 2 W, 1.5 W, and 1 W. The photostability of irradiated NPs with a concentration of 50 µg/ml was measured using laser power of 2 W. The experiment consisted of five on/off irradiation cycles of the NPs solution for 5 min and reconversion to the initial temperature. The temperature of the solutions was measured by a digital thermometer with a thermocouple sensor and thermal camera. Thermal imaging was performed using a SONEL KT-650 thermal camera (Świdnica, Poland).

4.4. Fourier Transform Infrared measurements

Fourier Transform Infrared (FTIR) spectra were collected using Jasco 4700 spectrometer. Samples were prepared as KBr pellets by applying pressure under a

hydraulic press to improve the signal from the sample. Before each spectral acquisition session, the background was recorded with pure KBr pellets, and the recorded background spectra were subtracted from each spectrum. Water and CO_2 peaks were automatically removed by the Spectra Manager software used to operate the spectrometer. The spectra were recorded with 1 cm^{-1} resolution by 512 scans in the 4000−200 cm^{-1} range.

4.5. Zeta potential measurements

Zeta (ξ) potential determination is a technique that allows estimation of the surface charge, which can be employed to understand the physical stability of nanosuspension. The method uses the difference between the frequency of the sent and recorded waves, i.e. the laser Doppler electrophoresis (LDE) method. It consists in registering the change in the frequency of the laser light wave after passing through the tested sample in relation to the coherent beam coming from the same source and travelling a similar distance. Frequency changes are measured by using optical or interferometric mixing. The zeta potential is a function of the charge on the surface of the molecule, the adsorbed layer adjacent to it, and the composition and nature of the medium. The zeta potential depends on the concentration of ions in the solution and their valence, which affects the thickness of the diffusion layer. In addition, the concentration of hydrogen ions, which translates into the solution's pH, influences the value of the zeta potential. The good physical stability of nanosuspensions due to the electrostatic repulsion of individual particles is a result of the large positive or negative value of the zeta potential of NPs. A zeta potential value lower than −30 mV or higher than +30 mV is generally considered to have a sufficient repulsive force to attain better physical colloidal stability. The ξ-potential value tending to 0 results in physical instability. In that case, the van der Waals attractive forces act upon NPs and their aggregation and flocculation.

The zeta potential was measured using a Malvern Zetasizer Nano Series Nano-ZS ZEN 3600 instrument. All samples were placed in a concentration 10 µg/ml of water 700 µl volume in DTS1070 Malvern Capillary Zeta Cell cuvette. Measurements were performed at RT and repeated 3 times.

4.6. Magnetic properties measurements

Magnetic measurements were performed in cooperation with dr Karol Synoradzki using a vibrating sample magnetometer (VSM) in a physical property measurement system over a temperature range of 4–300 K and applied magnetic field up to 5 T. A vibrating sample magnetometer works by inducing an electric field from a changing magnetic field, according to Faraday's Law of Induction. This electric field can be measured and used to determine how the magnetic field changes. The sample being investigated is exposed to a continuous magnetic field in order for the VSM to work. If the sample is magnetic, the magnetic domains or individual magnetic spins will aline with the field and magnetize. The magnetization will increase with the strength of the constant field.

5. Biological methods

5.1. Cell lines

HepG2 hepatocellular carcinoma cell line isolated from the human liver, U-118 MG glioblastoma cell line derived from a glioblastoma multiform and MRC-5 cell line isolated from the human lung tissue were purchased from American Type Culture Collection (ATCC, Manassas, VA, USA) and maintained at 37 $^\circ$C in a 5% CO_2 humidified environment. HepG2 cells were cultured in a Minimum Essential Medium Eagle (MEM) medium supplemented with 10% Fetal Bovine Serum (FBS), 1% antibiotics (penicillin 100 µg/ml, streptomycin 100 µg/ml), non-essential amino acids, and sodium pyruvate. U118 and MRC-5 cells were cultured in a Dulbecco's Modified Eagle Medium (DMEM)

supplemented with 10% FBS and 1% penicillin-streptomycin antibiotic. The cell lines were stored in liquid nitrogen in the NBMC AMU cell culture bank.

5.2. *In vitro* cell culture

The HepG2, U118 and MRC-5 cell culture was started by defreezing cells stored in a solution composed of 10 % DMSO in FBS. Next, cells were suspended in 5 ml of complete medium and centrifuged for 5 minutes at 1200 rpm at RT. After removing the supernatant, the cells were resuspended in complete medium, placed in 25 cm^2 or 75 cm^2 flasks and grown until the cell confluence reached 80%.

Cell passage was performed by rinsing the cells with HBSS buffer, then adding trypsin solution and placing the flask for 3 min (U118, MRC-5) or 8 min (HepG2) in an incubator. The trypsin action was inhibited by adding a complete medium. The cell suspension was diluted to approximately 30% confluency. Then, 10 ml of the diluted cell suspension was transferred to new culture vessels. All cell-related activities were performed under sterile conditions.

5.3. Cells seeding on plates

After enzymatic detachment of cells from the culture surface of the vessel, cells were resuspended in 10 ml of complete medium. From the obtained cell suspension, 10 µl were taken and introduced into the hemocytometer chamber. The cell concentration was determined by an TC10 Automatic cell counter (BIO-RAD). Then, a cell suspension was prepared at the required concentration: 10 000 cells/well in a 96-well plate for U118 and MRC-5; 20 000 cells/well in a 96-well plate for HepG2.

Cells were seeded in 96-well plates by adding 150 µl of the previously prepared suspension to the well and incubating for 24 h under culture conditions (37 °C, 5% CO_2). After 24 h of cultivation, the increasing concentrations of tested nanoparticles (1.25 µg/ml - 40 µg/ml for CUR@PDA NPs, and PDA@β-FeOOH NPs, and 1.125 µg/ml - 9 µg/ml for

PDA NPs) were added to each well, and the cells were further incubated for a defined period of time.

5.4. Electrophoretic analysis of dsRNA binding

A 1 % agarose gel was prepared by suspending 0.6 g of agarose in 60 ml of 1X TAE buffer in the flat bottom flask. To dissolve the agarose in the solution, the flask was placed in a microwave oven and heated until the agarose was completely dissolved. The flask with the solution was then cooled with cold water, and 3 µl of Simply Safe dye was added.

The dsRNA stock was prepared with an initial concentration of 100 ng/µl, whereas The PDA@DD NPs solution was prepared at an initial concentration of 1 µg/ml. Attachment of dsRNA to PDA@DD NPs was performed in a series of weight/weight ratios (1, 5, 10, 20, 30 µg nanoparticles/1 µg dsRNA) in a volume of 50 µl of water. After 30 minutes of incubation at RT, 15 µl of the complexes solution was mixed with 1 µl of the 6X loading dye solution and loaded to an agarose gel. The electrophoretic separation was carried out at 70 V for 20 minutes. After electrophoresis was completed, the gel was placed in a transilluminator and visualized under UV light.

5.5. mRNA expression measurements

The downregulation of tenascin-C mRNA expression was performed using the quantitative reverse transcriptase real-time PCR (qRT-PCR) with the Light-Cycler480 (Roche) (in cooperation with Małgorzata Grabowska, IBCH, PAS). Primers sequences were: TNC_L CCGGACCAAAACCATCAGT; TNC_R GGGATTAATGTCGGAAATGGT. The qRT-PCR proceeded under the following conditions: an initial 5 min preincubation at 95 °C, 45 cycles of denaturation in 95 °C for 10 s, annealing at 55 °C for 30 s and extension at 72 °C for 10 s. Hypoxanthine phosphoribosyltransferase (HPRT) was used as the endogenous control. The Light-

Cycler480 software allowed for an analysis basing on the E-method (Roche) expression level.

5.6. Confocal imaging

Confocal microscopy uses laser light passing through the objective of a standard light microscope to excite a specimen within a narrow plane of focus. The pinhole, or confocal aperture, rejects any emission of light from out-of-focus planes. As a result, this technique allows to get a very clear image of the sample and reduces the influence of artefacts. In this work, confocal microscopy was used to determine the ability of NPs to deliver DOXO into the cells.

For PDA@DD@DOXO NPs, U118 cells were seeded in a 8-well format culture vessel (Nunc™ Lab-Tek™ Chamber Slide™, Thermo Scientific) at a concentration of 25 000 cells/well. After 24 h, a solution of NPs at a concentration of 9 µg/ml and 4.5 µg/ml and 2.25 µg/ml was added to the cells and incubated for another 24 hours. After this time, the specimen was fixed in 4 % formaldehyde for 15 minutes at room temperature. In the next step, the cell nuclei were stained for 10 minutes with a solution of Hoechst 33342 dye in PBS buffer (5 µM). Between each step, cells were washed with PBS buffer.

For CUR@PDA@DD@DOXO NPs, U118 and HepG2 cells were seeded in a 8 well format culture vessel at a concentration of 25 000 cells/well and 40 000 cells/well, respectively. After 24 h, a solution of NPs at a concentration of 10 µg/ml and 5 µg/ml was added to the cells, and incubated for another 24 hours. After this time, the specimen was fixed in 4 % formaldehyde for 15 minutes at room temperature. A solution of AlexaFluor 647-conjugated concanavalin A in PBS buffer (25 µg/ml) was then added to the cells and incubated for 30 minutes at room temperature to stain cell membranes. In the next step, the cell nuclei were stained for 10 minutes with a solution of Hoechst 33342 dye in PBS buffer (5 µM). Between each step, cells were washed with DPBS buffer.

During imaging, DOXO fluorescence was imaged using 488 nm excitation and 560 –590 nm emission filters. Membrane fluorescence was excited with a 638 nm laser wavelength and collected in the 650−670 nm emission range. The fluorescence from the cell nuclei was excited with a laser wavelength of 405 nm and collected in the emission range of 425 − 475 nm. The obtained images were archived using the FV10-ASW computer software integrated with the Olympus FV1000 microscope system (60x objective, a 1.4 oil immersion lens).

5.7. Proliferation Assays

The proliferation assay is based upon the reduction of the WST-1 or MTT tetrazolium salt to formazan by cellular dehydrogenases. An expansion in the number of viable cells results in an increase in the overall activity of mitochondrial dehydrogenases in the sample, which in turn increases the amount of formazan dye formed. Quantification of the formazan dye produced by metabolically active cells can be performed using a scanning multi-well spectrophotometer.

5.7.1. WST-1 assay

To assess the cytotoxicity of the nanoparticles using WST-1 assay, 10 μl of WST-1 reagent was added to 200 μl of cell culture medium in a 96-well plate, and the cells were incubated for 4 h. To reduce the optical interference of nanoparticles, 100 μl of cell culture medium was transferred to clean multi-well plates before absorbance measuring in a spectrophotometer. The optical density was measured at 450 nm, and the cell viability was expressed as the respiration activity normalized to untreated cells (control). A culture medium (without cells) with the addition of 10 μl of WST-1 reagent was used as a blank. To assay the percent of living cells, obtained results were calculated according to the formula:

$$Living\ cells\ \% = \frac{mesured\ value - medium\ average}{control\ average - medium\ average}\ x\ 100\%$$

5.7.2. MTT assay

To assess the cytotoxicity of the nanoparticles using MTT assay, the cell culture medium was replaced with 100 μl of fresh medium in all wells of a 96-well plate. Then, 10 μl of 1 mg/ml MTT reagent prepared in PBS buffer was added to each well, and the cells were incubated for 4 h. In the next step, 100 μl of SDS (10% in 0.1 N HCl) was added to each well, and the plate was incubated at 37 °C overnight with shaking to dissolve the formazan crystals. The optical density was measured at 570 nm, and the cell viability was expressed as the respiration activity normalized to untreated cells (control). A culture medium (without cells) with the addition of 10 μl of MTT reagent was used as a blank. To assay the percent of living cells, obtained results were calculated according to the formula:

$$Living\ cells\ \% = \frac{mesured\ value - medium\ average}{control\ average - medium\ average}\ x\ 100\%$$

5.8. Live/Dead assay

The measurements for live and dead cell evaluation after incubation with nanoparticles were performed using high content screening (HCS) method. It is a method used in biological research, such as drug discovery to identify substances like small molecules, peptides, or RNA that alter the phenotype of a cell in the desired manner. In high content screening, cells are first incubated with the substance, and after a period of time, the structures and molecular components of the cells are analyzed. The use of labeled proteins with fluorescent tags is the most common analysis, then using the automated image analysis the changes in cell phenotype are calculated. The use of fluorescent tags

with different absorption and emission maxima enables the parallel measurement of several different cell components. Furthermore, imaging allows the detection of changes in cell structure. Therefore, a large number of data points can be collected per cell. In addition to fluorescent labelling, various label-free assays have been used in high-content screening.

Live/Dead assay is a very common cell staining procedure to asses cell membrane integrity. Live cells are stained with calcein and generate green fluorescence upon the excitation of their cytoplasm. Calcein has the ability to penetrate biological membranes freely. The acetoxymethyl modifying group obscures the calcium-binding sites, but since this motif is susceptible to enzymatic degradation, this group is cleaved after the entry of calcein into the cell. This prevents it from returning and allows calcium to bind again. This mechanism works only in living cells - dead cells lack adequate enzymes - so this technique is applicable to determining cell viability. Nuclei of dead cells are labelled with the ethidium homodimer dye (EthD). When cells die, the membrane of cells becomes disrupted. Thank to this, EthD may enter those cells and bind to DNA. Because live cells do not have a compromised membrane, the ethidium homodimer cannot enter the cells. The nuclei of all cells were labelled with Hoechst 33342, because it can pass through intact biological membranes, it can be used to stain both living and dead cells. The dye connects directly with DNA in the nucleus.

After incubation of cells with NPs, 100 μl of a prepared dye mixture containing 2 μM calcein, 2 μM ethidium homodimer, and 8 μM Hoechst 33342 in PBS buffer was added for 30 minutes at 37 °C. Then, the analysis was performed using the InCell Analyzer 2000 apparatus. Live cells were imaged using a green emission filter (FITC), dead cells with a red emission filter (TexasRed), and DAPI filter was used to visualize the blue signal of the nucleus. 20 randomly selected fields within one well were imaged at 20x magnification. Analysis of archived images was performed using the IN Cell Developer

Toolbox software. The images in the DAPI channel determined the total number of cells. The number of live cells was determined by the images in the FITC channel, while the images in the TexasRed channel determined the number of dead cells.

5.9. Flow cytometry assays

Flow cytometry is a laser-based technique used to detect and analyze the chemical and physical characteristics of cells or particles. The general mechanism of flow cytometry is the single-file passage of cells in front of a laser for detection, counting, and sorting. Fluorescently marked cell components are activated by the laser to emit light at various wavelengths. The quantity and kind of cells in a sample can then be determined by measuring the fluorescence. It is possible to analyze up to a thousand particles per second as they move through the liquid stream. Assays were performed using the Guava® Muse® Cell Analyzer.

5.9.1. Oxidative stress assay

The level of reactive oxygen species (ROS) in cells were measured using flow cytometry according to manufacturer protocol. ROS are known to have a broader role in all cell types in functions such as cell signaling and regulation, activation of signaling cascades and apoptosis, and alternate death pathways. The ability to react with a variety of cellular targets, including enzyme active sites, nucleic acids and lipids results in a wide range of pathologies associated with superoxide and ROS generation. Superoxide and ROS have thus been implicated in the pathophysiology of multiple diseases ranging from cancer, Alzheimer, sepsis, diabetes, and cardiovascular disease.

The Muse® Oxidative Stress assay allows for the quantitative measurements of cellular populations undergoing oxidative stress resulting in the detection of reactive oxygen species, namely superoxide. Dihydroethidium (DHE) is a well-characterized reagent that has been widely utilized to find reactive oxidative species in cells, is the

foundation of the Muse® Oxidative Stress Reagent. The reagent is cell permeable, and it has long been postulated that DHE, upon reaction with superoxide anions, undergoes oxidation to form the DNA-binding fluorophore ethidium bromide or a structurally similar product which intercalates with DNA resulting in red fluorescence.

To evaluate the level of reactive oxygen species in cells after incubation with nanoparticles the Muse® Oxidative Stress assay was performed. First, cell media was removed and the cells were washed with 100 μl of PBS buffer. After enzymatic detachment of cells from wells with 50 μl of trypsin, 150 μl of culture medium was added to each well, and cells were transferred to 1.5 ml tube. Next, the cells were centrifuged for 5 min at 1 200 rpm at RT. The cell medium was and the cells were washed with 500 μl of PBS buffer. After the second centrifugation step under the same conditions, the PBS buffer was removed, and cells were suspended in a labelling solution. To prepare the intermediate labeling solution, 1 μl of oxidative stress reagent was dissolved in 99 μl of 1x assay buffer. Next, the working solution in a ratio of 1:80 was diluted again in 1x assay buffer. Then, 190 μl of the mixture was added to cells suspended in 10 μl of PBS buffer and incubated for 30 min in the thermal shaker at 37 °C. In the final step, the stained cells were analyzed using MUSE® Cell Analyzer. Non-treated cells (w/o nanoparticles) and the cells treated with 1 mM menadione were used as a negative and positive control, respectively.

5.9.2. Annexin V and dead cell assay

Apoptotic cell death was measured using flow cytometry according to manufacturer protocol. Using Muse Annexin V & Dead Cell Assay it is possible to determine the number of alive, early and late apoptotic and dead cells in adherent and suspension cell lines. Apoptosis, or programmed cell death, is an important and active regulatory pathway of cell growth and proliferation. Cells respond to specific induction signals by initiating intracellular processes that result in characteristic physiological changes. Among these are

the externalization of phosphatidylserine (PS) to the cell surface, cleavage and degradation of specific cellular proteins, compaction and fragmentation of nuclear chromatin, and loss of membrane integrity (in late stages). Annexin V is a calcium-dependent phospholipid-binding protein with a high affinity for PS, a membrane component normally localized to the internal face of the cell membrane. Early in the apoptotic pathway, molecules of PS are translocated to the cell membrane's outer surface, where Annexin V can readily bind them.

To evaluate the level of apoptotic cells after incubation with nanoparticles the Muse® annexin V and dead cell assay was performed. First, cell media was removed, and the cells were washed with 100 μl of PBS buffer. After the enzymatic detachment of cells from wells with 50 μl of trypsin, 150 μl of the medium was added to each well, and the cells were transferred to 1.5 ml tube. Next, the cells were centrifuged for 5 min at 1 200 rpm at RT. The supernatant was then removed, and the cells were washed with 500 μl of PBS buffer. In the final step, the cells were suspended in a mixture of 100 μl of 1% FBS in PBS buffer and 100 μl of annexin V and dead cell reagent, followed by 20 min incubation at RT in the dark. The stained cells were then analyzed using MUSE® Cell Analyzer. Non-treated cells (w/o nanoparticles) and the cells treated with 5 μg/ml DOXO were used as a negative and positive control, respectively.

5.9.3. Cell viability assay

Cell viability was measured using flow cytometry according to manufacturer protocol. The Muse™ count and viability assay allows the calculation of cell count and viability. It is a rapid and reliable alternative to trypan blue exclusion assay. The Muse™ count and viability reagent provides absolute cell count and viability data on cell suspensions from various cultured mammalian cell lines. The viable and non-viable cells are differentially stained based on their permeability to the DNA-binding dyes in the reagent.

To evaluate the number of live and dead cells after incubation with nanoparticles, the Muse® count and viability assay was performed. First, cell media was removed and the cells were washed with 100 µl of PBS buffer. After the enzymatic detachment of cells from wells with 50 µl of trypsin, 150 µl of media was added to each well, and the cells were transferred to 1.5 ml tube. Next, the cells were centrifuged for 5 min at 1 200 rpm at RT. Cell media was removed and the cells were washed with 500 µl of PBS buffer. Then, 190 µl of the Muse® count and viability reagent was added to cells suspended in 10 µl of PBS buffer and incubated for 10 min at RT in the dark. In the final step, the stained cells were analyzed using MUSE® Cell Analyzer. Non-treated cells (w/o nanoparticles) were used as a negative control.

5.9.4. Irradiation of cells with 808 nm laser light

For tests with 808 nm laser light irradiation, the cells were seeded on 96-well plates at a concentration of 10 000 and 20 000 cells/well for U118 and HepG2 cells, respectively. Irradiations were performed in environmental chamber at 37 °C after 24 h from the addition of PDA@DD@DOXO@RNA NPs to the cells and after 4 h from the addition of CUR@PDA@DD@DOXO NPs to the cells. The source of the laser light was placed below the cell culture plate directly under a specific well. Each well was irradiated with 808 nm laser wavelength over 5 min.

Due to the partial detachment of cells as a result of irradiation, cell culture medium was not removed to collect all cells for flow cytometry analysis.

5.10. Statistics

All experiments were done in triplicate, and the results were presented as mean ± standard deviation. The experimental data were analyzed by ANOVA with post-hoc Tukey HSD test. Statistical significance was marked with asterisks depending on the p-value: *—$p \leq 0.05$, **—$p \leq 0.01$, ***—$p \leq 0.001$, ****—$p \leq 0.0001$.

IV.   RESULTS AND DISCUSSION

The doctoral thesis presents three approaches to develop a multifunctional platform based on polydopamine nanoparticles for cancer treatment. In the following chapters, each approach is described independently, and the general protocols for obtaining reproducible and high-quality PDA nanoparticles are established.

CHAPTER 1

6.   Spherical polydopamine nanoparticles

This chapter is focused on the development of spherical PDA NPs with a specified size. The conditions affecting synthesis process, its efficiency, and the properties of final PDA nanoparticles are described.

6.1. Size determination of polydopamine nanoparticles

According to a previously reported protocol, the PDA nanoparticles were obtained by oxidative polymerization of dopamine hydrochloride under alkaline conditions. [78] The most important aspects of the reaction affecting the size of the nanoparticles are NaOH concentration, dopamine concentration, the temperature of polymerization, and the mixing time (**Figure 9**). It was decided to manipulate the size of NPs by the addition of different NaOH concentrations in the solution. Other parameters were kept at constant values during the whole process of developing the universal protocol for material synthesis. Dopamine hydrochloride (200 mg, 10 mM) was dissolved in 100 ml of Milli-Q water in a round-bottom flask. The solution was placed on a magnetic stirrer and heated up to 50 °C in an oil bath. Carrying out the experiment at 50 °C reduced the synthesis time of the PDA NPs. Faster production of nanoparticles resulted in quicker preparation of the final product, which is especially important when the biological experiments are planned. To develop size dependent protocol of the PDA NPs, different amounts of 1M NaOH were then added

to the DOPA solution. The synthesis was finished after 3 h, when the solution became completely black. Additionally, it was observed that the total amount of the NPs after each synthesis was different. The critical parameter affecting the efficiency of the synthesis was the temperature at which NaOH is added to the solution. It was observed that the biggest amount of nanoparticles can be obtained when NaOH is added to the reaction at 48 °C.

One of the main parameters showing the DOPA polymerization status is the color of the solution. Initially, the mixture of DOPA and water is fully transparent at room temperature. After reaching around 50 °C in the flask, the solution becomes a little pink but still transparent. The addition of NaOH changes the color of the solution to slightly brown. The color of the solution can also be useful indicator to see if NaOH was added at a temperature above or below 48 °C. It will be slightly brown at higher temperatures and yellow at lower temperatures. Based on experience during synthesis optimization, the yellow color of the solution after adding NaOH suggests lower synthesis efficiency. With time the whole mixture in the flask will become completely black and nontransparent.
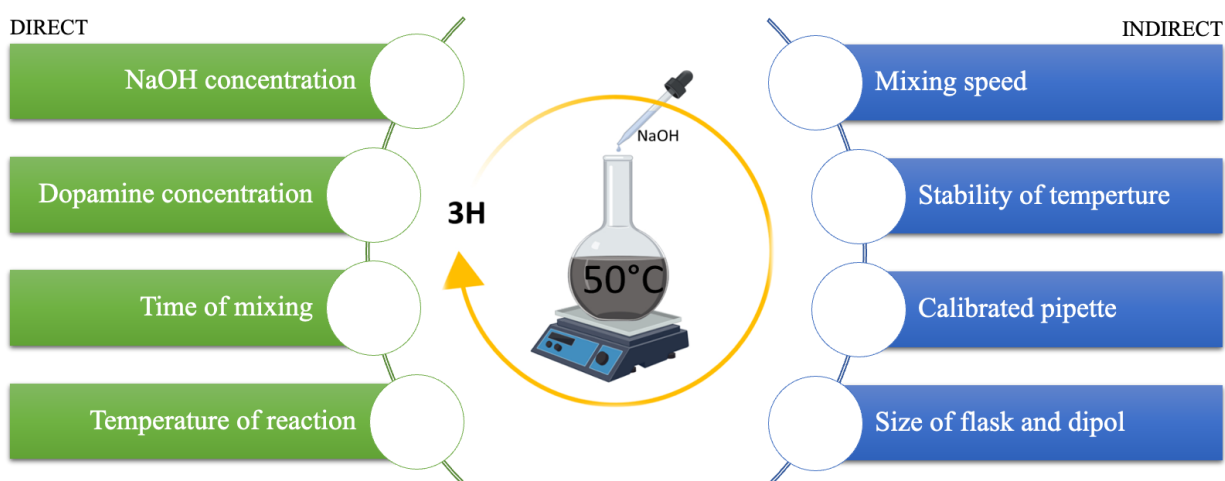
Figure 9. Graphical illustration of the parameters which direct (left side) and indirect (right side) affect the size of PDA NPs.

After imaging the nanoparticles with TEM, the dependence between the amount of NaOH used and the size of nanoparticles was demonstrated. As shown in **Figure 10**, the size of PDA particles ranges between 40 nm and 500 nm in diameter. Higher concentration of NaOH in the solution results in a smaller diameter of NPs (**Figure 10 A, C**) and more homogeneous sample (**Figure 10 B, D**).
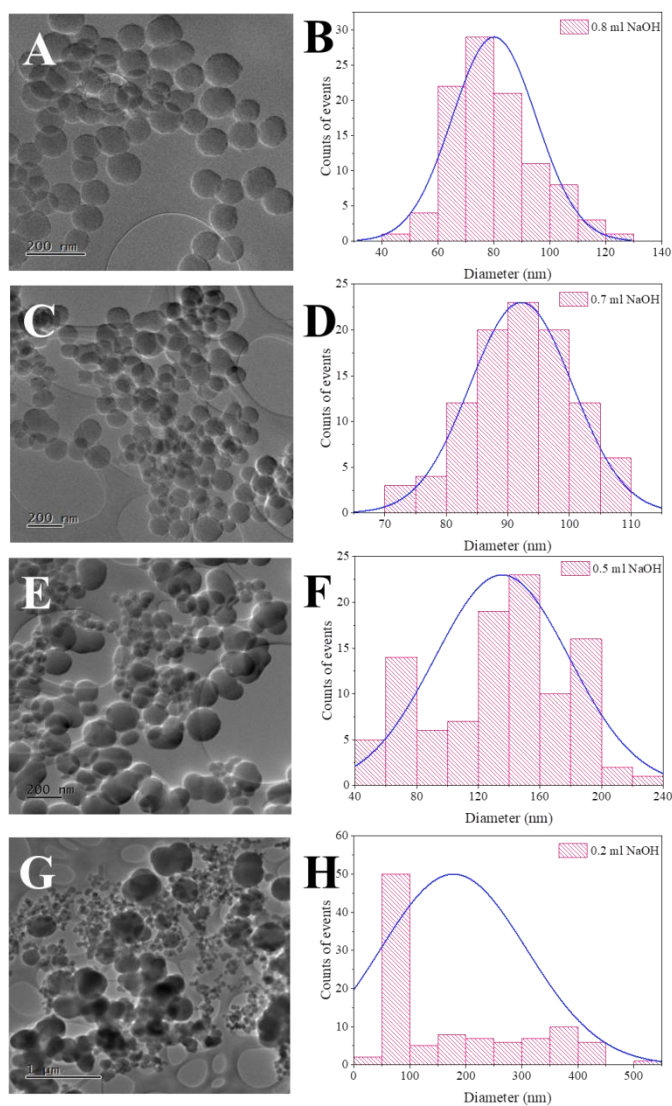
Figure 10. HR-TEM images and histograms showing the morphology and size of PDA particles after synthesis with addition of **A, B** 0.8 ml NaOH, **C, D** 0.7 ml NaOH, **E, F** 0.5 ml NaOH, and **G, H** 0.2 ml NaOH.

TEM analysis revealed differences in the shape of PDA NPs. As the size of particles increases, they are more defined, and their surface is clear and smooth. However, their shape is not clearly spherical (**Figure 10 E, G**), and a wide deviation of NPs sizes is visible (**Figure 10 F, H**). With decreasing size, the surface of the particles became rougher but they are still spherical in shape.

Aggregation of PDA NPs was not visible in the homogeneous samples of NPs (**Figure 10**). There is no visible connection between particles. These results suggest that the aggregation of nanoparticles could be caused by drying during sample preparation for TEM imaging. Well-defined PDA NPs with a size of 100 nm in diameter were selected for further experiments (sample after synthesis using 0.7 ml of NaOH). Lack of aggregation is especially important in the case of their further functionalization.

In the next step, the reproducibility of the PDA NPs synthesis was checked. It was found that the indirect parameters affecting the homogeneity of the PDA NPs were connected with the technological parameters such as mixing speed, the dimension of magnetic dipole and flask, temperature stability, and calibration of the pipettes. It was noticed that using even different magnetic stirrers or older pipettes affected the results. The older devices were not precise enough to add the same amount of NaOH each time or set an accurate mixing speed. It was important to use calibrated pipettes and magnetic stirrers with electronic displays to provide the same synthesis conditions. Another critical parameter affecting the size of nanoparticles was the stability of temperature in the flask. It was not possible to provide stable or isolated temperature conditions for this synthesis in the laboratory. It is known that the temperature, homogeneity, and viscosity of the air in the laboratory change and depend on the season. There is air conditioner in the building in summer and heating in winter. Hence, airwaves in the laboratory affect the environment of

the experiments. It was necessary to use precise temperature sensor. After overcoming all these issues, the synthesis became highly reproducible.

In this study, a well-established protocol for the synthesis of particles of various sizes in the diameter range of 40 nm to 500 nm was obtained. Considering the commercial production of these carriers for biomedical applications, this protocol was highly repeatable. The production of nanoparticles was cheap and effective. The purification of NPs was simple and economical, their separation was very good. The nanocarriers had also the required size in order to be used in cancer therapy.

6.2. Physicochemical characteristics of PDA NPs

Detailed investigation of pure PDA NPs is necessary to characterize the material thoroughly and confirm its further functionalization. The chosen 100 nm PDA NPs were analyzed using the zeta potential measurements, FTIR spectroscopy, and photothermal properties measurements.

6.2.1. Surface charge

Zeta potential measurements were performed in a water solution with a concentration of NPs below 10 μl/ml, repeated three times with an average of 20 numbers of measurements. Obtained pure PDA NPs have zeta potential around –30 mV. The positive or negative surface charge on PDA NPs arises from the reversible dissociation and deprotonation/protonation of amine and catechol groups, featuring PDA zwitterionicity. The defined chemical structure of PDA is still a wide topic of research. Depending on the synthesis method, different chemical groups can be located on the surface (i. e. quinone imine, catechol groups) of PDA NPs, which affect the zeta potential value as well as measurement conditions. There is no general agreement regarding the zeta potential value. The overall value of the PDA surface charge is negative and was reported between −4.58 mV and −39 mV. [79–83] The hydrodynamic diameter measurements using DLS are

difficult in the case of PDA because of the high absorbance of light in broad spectra. DLS measurement is based on the irradiation of the sample with laser light and its scattering. In the case of PDA, the results cannot be relevant. It is impossible to determine how the device detected much-scattered light and how much was absorbed by PDA NPs. That's why the hydrodynamic diameter of PDA NPs is not always presented in the literature. In this work, the hydrodynamic diameter of NPs was different each time, so the measurements were not repeatable, which also proves this theory.

6.2.2. Chemical structure

FT-IR measurements were performed using the powder method in which the PDA NPs were mixed with KBr to improve the signal from the sample. As shown in **Figure 11**, a large signal corresponding to the stretching vibrations of the hydroxylic groups (-OH) and N-H groups in a range of $3700 - 2500$ cm^{-1} with a maximum value of around 3400 cm^{-1} is visible. This broadband results from catechol groups of dopamine on the surface. The bending vibration peak of N-H was located at 1628 cm^{-1}. A peak at 1290 cm^{-1} indicated the presence of a C-O bond. The peak at 1472 cm^{-1} was attributed to the C=C ring starching band overlapping with the -CH$_2$ scissoring band. [84]
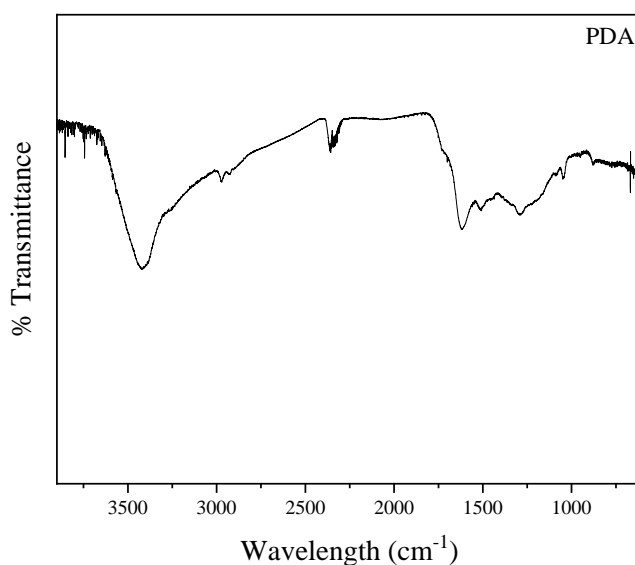
Figure 11. FTIR spectra of PDA NPs.

6.2.3. Photothermal properties

The photothermal properties of the PDA NPs were investigated by measuring the temperature at 10 s intervals over 10 min of irradiation with laser light at 808 nm wavelength and laser power of: 3 W, 2 W, and 1 W (**Figure 12 A, B, C**). The temperature change is evident in a concentration-dependent manner. Even at 10 (g/ml concentration, the temperature increased for all laser powers. The most significant temperature increase was present in the first few minutes of irradiation, further, it reaches slowly to saturation point. The highest temperature was obtained at 100 (g/ml concentration with a laser power of 3 W, and the value of 47 °C was achieved. As shown on each graph, the temperature change in the control sample is barely visible. The time of irradiation was defined as 10 min, because the saturation was achieved after this time. To avoid damage of the collateral tissues cell irradiation cannot be performed for too long, and the temperature increase should be temporary in one specific place. Hence, the PT measurements were also conducted with different laser powers to determine the most effective conditions for PT therapy in cells. Higher laser power allows using a smaller amount of NPs in experiments conducted with cancer cells.

Another critical aspect of PTT is the stability of the material used for temperature increase. The photostability analysis was performed in the same conditions on the PDA sample at a concentration of 50 μg/ml. Results presented in **Figure 12 D** show that this NPs could be used in at least five on/off laser irradiation cycles, proving that the material is highly stable in time. It is also essential when the PT therapy must be performed in cells.

A thermographic camera also confirmed obtained temperature values (**Figure 12 E**). The focus of the camera was placed in the middle of the cuvette containing 50 μg/ml of PDA NPs in water. The photos were taken after each 30 s over 5 min of irradiation with laser light. The temperature increase is visualized based on color intensity according to the

thermal scale, and the specific temperature value in the cuvette is also visible in numbers on the photo. The maximum value after 300 s corresponds to the value presented in **Figure 12 A**. It confirmed that the results are repeatable, and using a different method of investigation, the characteristics of PDA NPs is the same, and the thermographic camera is a good method to visualize the change of temperature during irradiation.
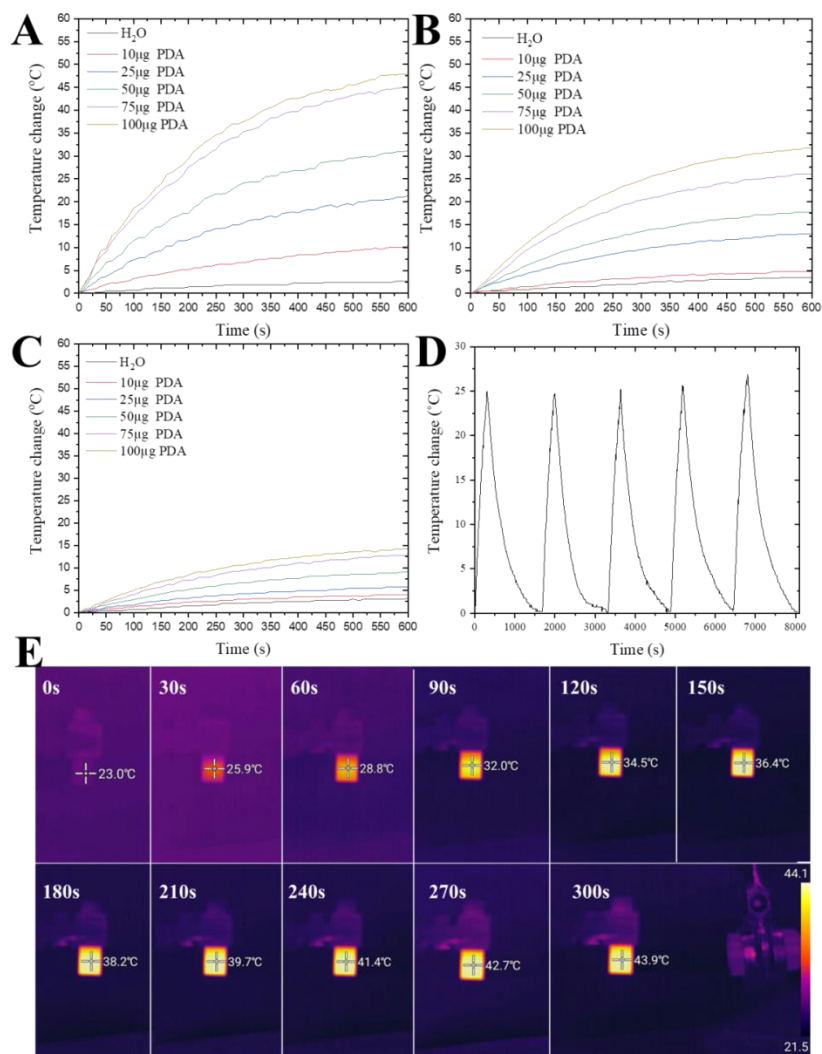
Figure 12. PT properties of PDA NPs after irradiation with **A** 3 W, **B** 2 W, and **C** 1 W. Graph showing **D** PT stability of 50 µg/ml PDA NPs after irradiation,. **E** Thermographic camera images presenting an increase of temperature in the cuvette with PDA nanoparticles in 50 µg/ml concentration over 5 min as a result of laser irradiation (808 nm wavelength).

CHAPTER 2

7. Spherical polydopamine nanoparticles for combined gene/chemo and phototherapy

The 100 nm PDA NPs obtained and described in the previous chapter became the basis for further functionalization in order to develop the multifunctional carrier (**Figure 13).** In this chapter, the functionalization of the surface of particles with PAMAM dendrimers, loading of doxorubicin and attachment of RNA as a therapeutic agents are presented. In the last step, the biological results containing cytotoxicity assessment and combined treatment efficiency evaluation on glioblastoma cells are shown.
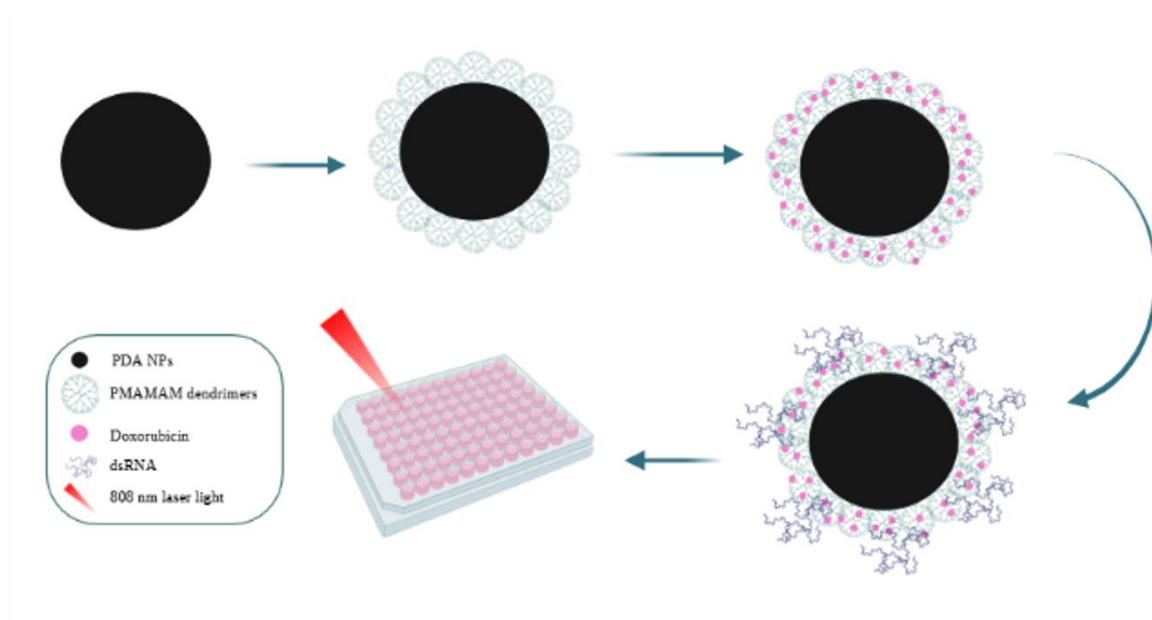
Figure 13. Schematic presentation of the main idea of the use of PDA NPs for combined gene/chemo and phototherapy which contains: PDA NPs functionalization with PAMAM dendrimers, DOXO loading, attachment of RNA and biological investigation of treatment efficiency.

7.1. Functionalization of polydopamine nanoparticles

7.1.1. PAMAM dendrimers attachment

The first step of PDA NPs surface functionalization was dendrimers attachment which serve as containers for hydrophobic drug delivery. Their assignment was to accumulate chemotherapeutics inside their structure and release them depending on pH. It was decided to use commercially available amine groups terminated polyamidoamine (PAMAM) dendrimers (DD). Third generation dendrimers used in this study are characterized by a diameter of 3.2 nm and 32 surface amine group and ethylenediamine core. Dendrimers were connected with PDA NPs surfaces by Michael's reaction between peripheral amine groups present in DD and quinone groups present in the PDA structure. The functionalization process was performed overnight at room temperature in a 1:3 ratio of components (PDA NPs: DD). At the beginning, 100 nm particles were collected by centrifugation and dispersed in a proportional volume of 10 mM TRIS buffer. The buffer volume should be three times bigger than the amount of NPs. In other cases, the functionalization will be ineffective because of the aggregation of the particles. The substrates interact strongly with each other in a small buffer volume. After determining the appropriate concentration of polydopamine in the solution, the flask was placed on a magnetic stirrer, and PAMAM dendrimers were added dropwise. The sample was purified by centrifugation (22 000 rpm, 20 min) and washed three times with Milli-Q water.

To confirm the effectiveness of the functionalization of PDA NPs, zeta potential measurements were performed. Pure PDA NPs had a zeta potential of around −30 mV, and after the reaction, the value increased to +42 mV (**Figure 14 A**). It proves that the PAMAM dendrimers efficiently covered the surface of NPs. The zeta potential increased because of the positively charged amine group in the PAMAM dendrimers structure.

In a further step, a test was performed to check the stability of PDA@DD NPs in different solutions. The exact amount of PDA@DD NPs was placed in four different solutions: water, PBS buffer (pH 7.4), citric acid (CA) (pH 5.5), and 50 % saccharose. Then, the zeta potential of the NPs was measured. The results showed that the best stability of PDA@DD NPs was observed in water (**Figure 14 B**). Their stability was much lower in other solutions, as demonstrated in visible sedimentation.

Additionally, the stability of the sample was measured in time. The zeta potential measurements were repeated on the same sample after one, two and three weeks to check the stability of the interaction between dendrimers and particles. The value didn't change after a week, but after two weeks, it started to decrease (**Figure 14 C**). This observation suggests that it is the beginning of the dendrimers' detachment from the nanoparticles. Therefore, the PDA@DD NPs in this work were used for a maximum of two weeks after preparation.
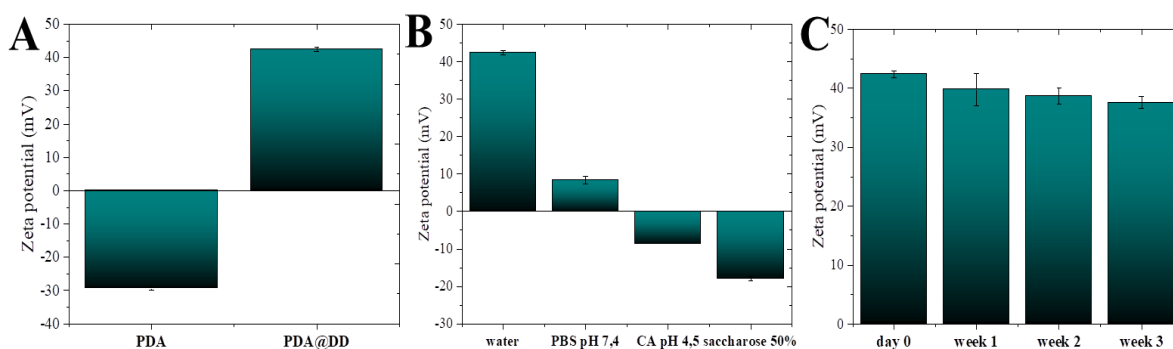
Figure 14. The change of zeta potential value **A** after functionalization of PDA NPs with PAMAM dendrimers, **B** stability of PDA@DD in different solutions, **C** time stability of PDA@DD stored in water.

7.1.2. Doxorubicin loading and release

Doxorubicin (DOXO), a model chemotherapeutic drug used in cancer therapy, was loaded on the PDA@DD NPs at a 1:1 NPs to DOXO ratio. After 24 h of mixing, the sample was centrifuged and washed a few times with PBS buffer until receiving a clear solution. Then, PBS buffer sample was collected to perform UV-Vis measurements and to calculate the total amount of loaded DOXO (EE% and LC%) according to the formula presented in Materials and Methods section. Samples with a known amount of free DOXO were used to prepare a calibration curve.

The EE % and LC % of DOXO on NPs was calculated to be 99 %. The values are the same because of the 1:1 ratio between NPs and DOXO used for loading and high capacity of DD on PDA NPs surface.

The release of DOXO from the PDA@DD sample was tested in three different buffers: CA (pH 4.5 and 5.5), and PBS buffer (pH 7.5). The release was measured every hour for the first six hours and then for 24 h and 48 h using a UV-Vis spectrophotometer. The results are presented in **Figure 15**. It is visible that the most extensive release of DOXO occurs in the first few hours for all samples and then reaches a plateau. The biggest cumulative release of DOXO is present for the sample incubated in CA with a pH 4.5. The middle value of cumulative release is present at pH 5.5 and the smallest at pH 7.4. It is known that weak noncovalent bonds can be destabilized by an acid environment and cause the release of the drug. These experiments proved that the most effective release is present in the lowest pH simulating conditions in cancer cells. Obtained results confirmed that the loading of DOXO was highly efficient and successful release in cancer cells using PDA@DD NPs could be observed.
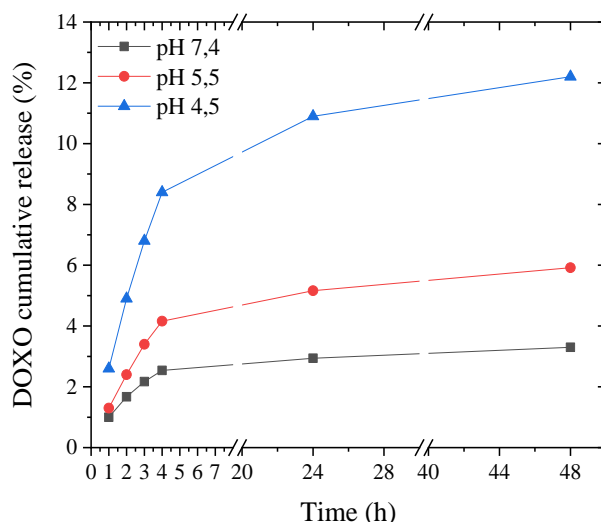
Figure 15. Cumulative release of DOXO from PDA@DD@DOXO over 48 h at 37 °C in different pH values.

7.1.3. Attachment of dsRNA

Double stranded RNA (dsRNA) complementary to tenascin C (TN-C) sequence was used to create complexes with PDA@DD NPs. Negatively charged dsRNA interacts with positively charged NH_2^+ groups on the surface of PAMAM according to electrostatic interactions. Noncovalent binding facilitates the detachment of dsRNA from NPs and silencing the expression of TN-C protein. Different weight ratios between dsRNA and PDA@DD varied from 1:1 to 30:1 were checked using the agarose gel electrophoresis. This test uses a fluorescent dye to visualize unbound strands of dsRNA. The results are presented on **Figure 16 A and B** show a comparison of RNA binding efficiency between PDA@DD and PDA@DD@DOXO NPs. The bright band on the left side is a control sample containing only naked dsRNA. The lower intensity of the band confirms the connection between the dsRNA and NPs. There is no free dsRNA in the sample when the band is not present, which means it is fully attached to the NPs. In the case of PDA@DD, the full binding is present at a ratio of 30:1, whereas in the sample with DOXO full

interaction is observed at a ratio of 1:10. It suggests that the presence of DOXO in dendrimers can improve the amount of dsRNA attached to the carrier. Some of the dsRNA strands can interact with the functional groups of DOXO.
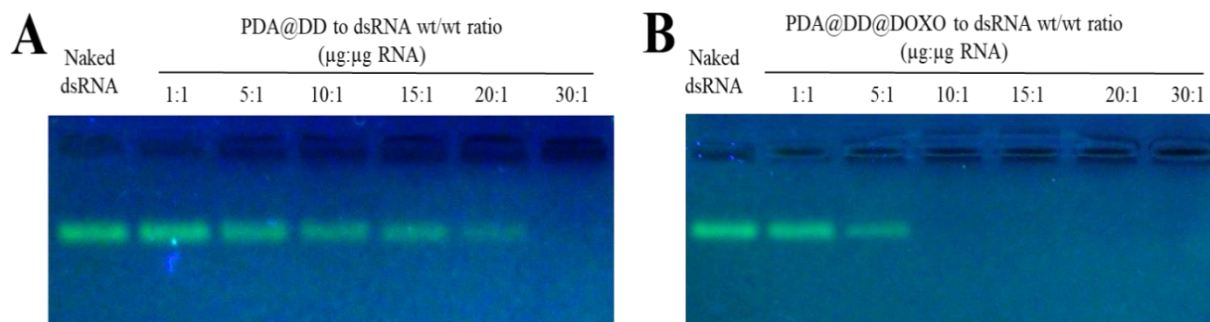
Figure 16. Agarose gel electrophoresis of **A** PDA@DD and **B** PDA@DD@DOXO complexes with dsRNA at different mass ratios.

The effectiveness of each functionalization step was confirmed using zeta potential measurements (**Figure 17**). Pure PDA NPs had a zeta potential value of around -30 mV. After functionalization with PAMAM dendrimers, the value increased to $+44$ mV. The attachment of RNA to NH_2^+ groups caused a decrease in the zeta potential to $+8$ mV. The value change is not that significant in the case of DOXO loading. Due to the DOXO being located inside the structure of dendrimers, the decrease of zeta potential is minimal. The value of the final product (PDA@DD@DOXO@RNA) was around -20 mV.
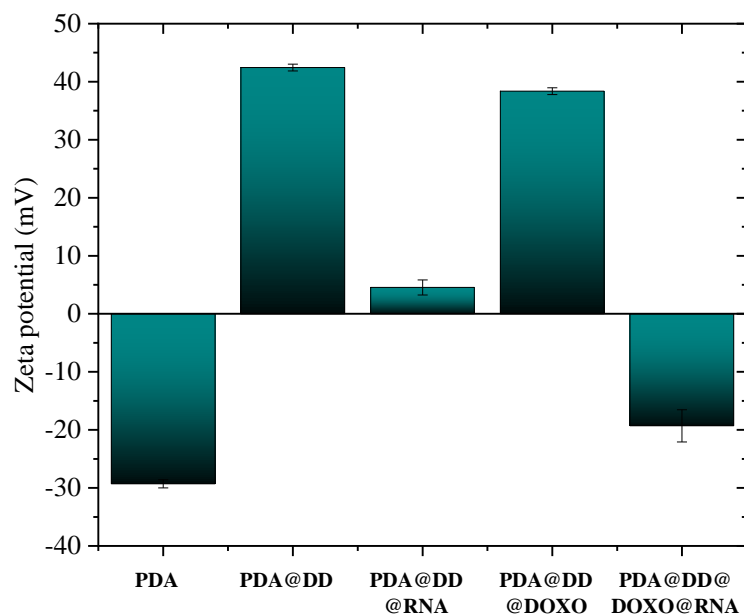
Figure 17. Zeta potential values of each step of complexes preparation.

7.2. Evaluation of the therapy efficiency

7.2.1. Cytotoxicity of polydopamine nanoparticles

To check the influence of PDA@DD NPs on U118 cell viability, WST-1 and live/dead assays as a complementary method were performed with a concentration of NPs at 9 μg/ml, 4.5 μg/ml, 2.25 μg/ml, and 1.125 μg/ml. As a control, assays on MRC-5 fibroblasts were performed to check the influence of carriers on proliferation of normal cell. The WST-1 results show the slight decrease in cell viability of both cell types at the highest concentration of PDA@DD NPs. In this case, cell viability achieved a value of around 70% for U118 cells and 80% for MRC-5 cells.(**Figure 18 A, B**).
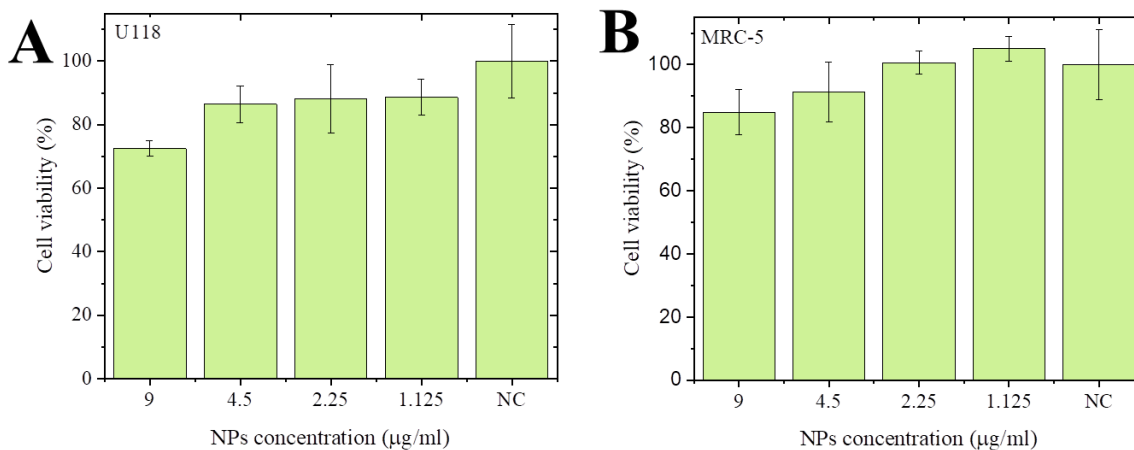
Figure 18. Cell viability results obtained using WST-1 assay for **A** U118 and **C** MRC-5 cells after 48 h incubation with PDA@DD NPs. NC: negative control (cells without NPs)

The results obtained using high content screening with InCell Analyzer show no significant change in the viability of U118 and MRC-5 cells after incubation with PDA@DD NPs (**Figure 19 A, B**). No difference in cell viability is also confirmed on images presented in **Figure 19 C, D**. Mostly green signals from live cells and only a few red spots from dead cells are visible on the images. It confirmed that pure PDA@DD carrier did not exhibit cytotoxicity in all tested concentrations.

In conclusion, this material without therapeutic agents can be described as nontoxic as it does not adversely affect normal and cancer cells.
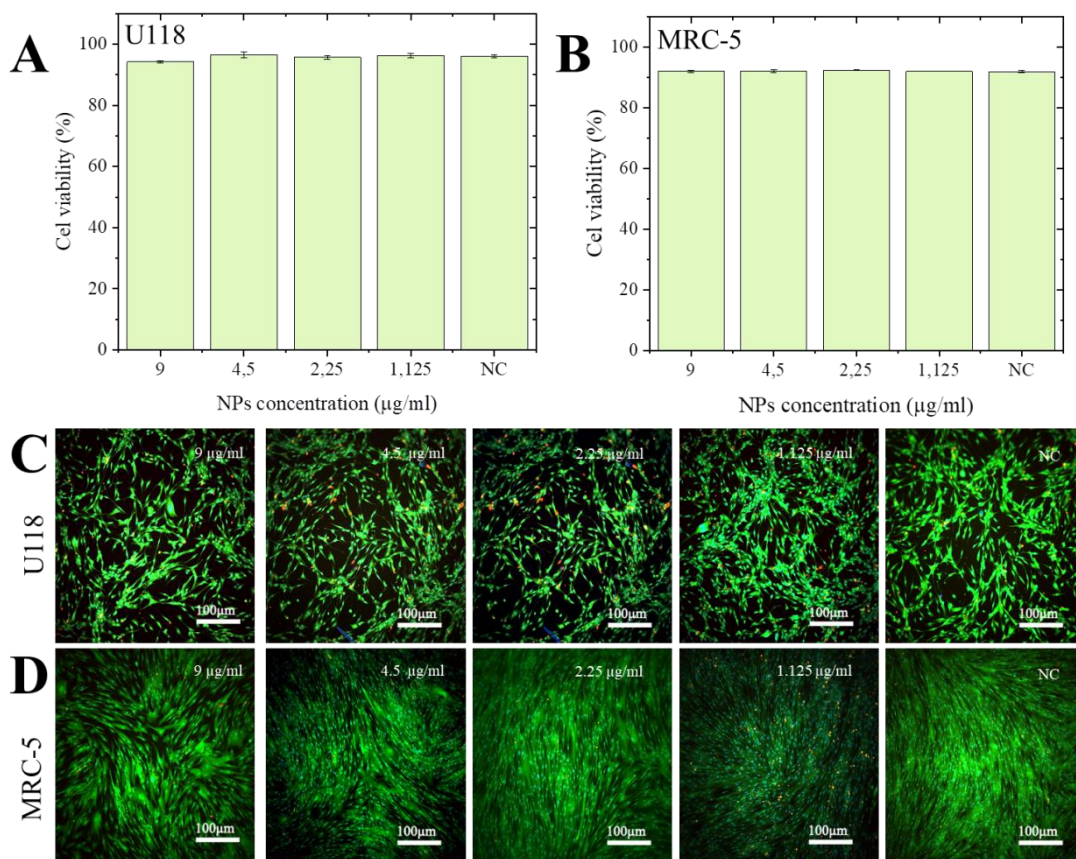
Figure 19. Cell viability results of live/dead assay and images obtained using In Cell Analyzer for **A, B** U118 cells and **C, D** MRC-5 cells after 48 h incubation with PDA@DD NPs. NC: negative control (cells without NPs)

7.2.2. Gene therapy

To reduce expression of tenascin C protein, PDA@DD@DOX NPs with various concentrations of dsRNA (25, 50, 100 nM) at 30:1 NPs to RNA wt/wt ratio were used. The qRT-PCR assay was performed 24 h after delivery of NPs on U118 glioblastoma cell lines to examine the expression level of tenascin C. The down-regulation of tenascin C mRNA expression was analyzed in comparison to NPs without dsRNA. As shown in **Figure 20**, the drop in the tenascin C expression level was visible at higher concentrations. The level of tenascin C was decreased from 20% at a concentration of 50 nM dsRNA to 50% for

cells treated with 100 nM dsRNA, whereas this effect was not observed at 25 nM concentration of dsRNA. There is no visible change in tenascin C expression in case of NPs without dsRNA. It proved that developed NPs are an effective delivery system for dsRNA, which successfully inhibit tenascin C in U118 cells at concentrations above 50 nM dsRNA.
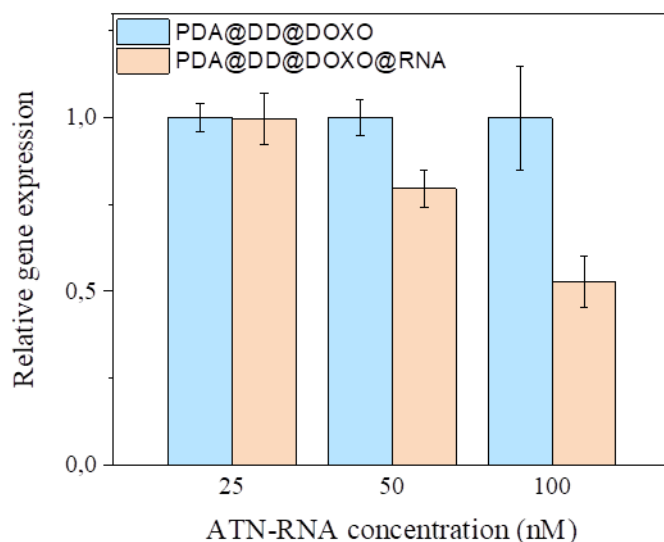
Figure 20. The relative expression level of tenascin C on U118 glioblastoma cells after incubation with PDA@DD@DOXO and PDA@DD@DOXO@RNA NPs.

7.2.3. Chemotherapy

The efficiency of chemotherapy using Annexin V apoptosis assay was investigated. For this purpose, U118 cells were incubated for 48 h with PDA@DD@DOXO@RNA NPs at a concentration range of 9 μg/ml and 1.125 μg/ml. The apoptosis profile of U118 cells was analyzed using flow cytometry. As shown in **Figure 21**, the treatment of glioblastoma cells using this type of NPs is very effective, even in the smallest concentration of NPs. The late apoptotic cell rate induced by the PDA@DD@DOXO@RNA NPs was nearly 100% for the whole concentration range.
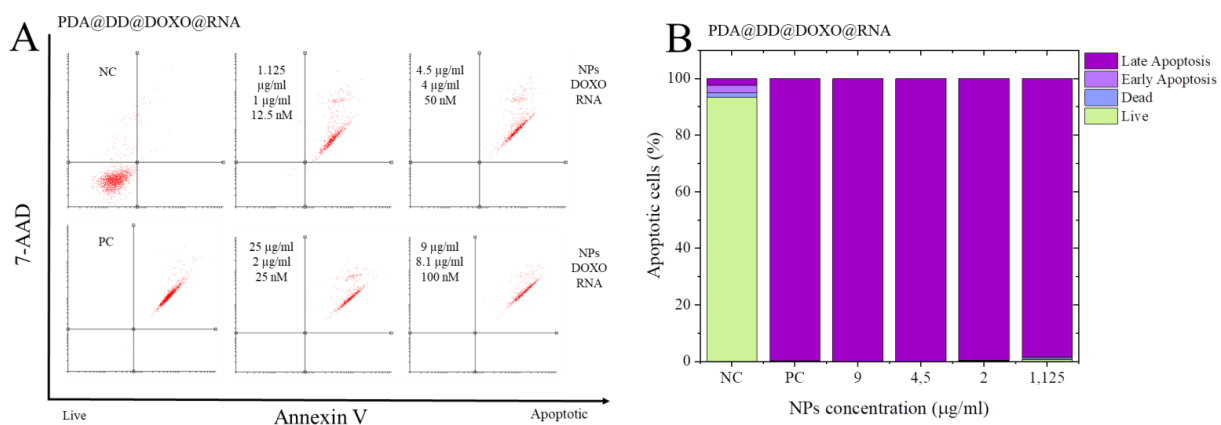
Figure 21. Apoptosis profile of U118 cells after 48 h of incubation with PDA@DD@DOXO@RNA NPs evaluated using Annexin V assay. **A** Dot plots and **B** bar graph showing calculated results from the flow cytometer. NC: negative control (cells without NPs), PC: positive control (DOXO 5 µg/ml)

Confocal imaging was performed to visualize the uptake of DOXO into the U118 cells. Cells were incubated with NPs at concentrations of 9 µg/ml, 4.5 µg/ml and 2.25 µg/ml over 4h. After that time, cells were fixed, and the images were taken using a fluorescence microscope. The intensity of the signal depends on the amount of DOXO in the analyzed NPs. **Figure 22** revealed that the highest intensity was present for the sample with a concentration of 9 µg/ml corresponding to 8 µg/ml of DOXO. In cells without NPs, there is no visible signal in the channel of DOXO. Based on obtained images, it is clearly seen that DOXO enters the cell and accumulates in the nucleus area. It means that DOXO is able to provide effective therapy by intercalating in DNA structure and causing apoptosis-related cell death.
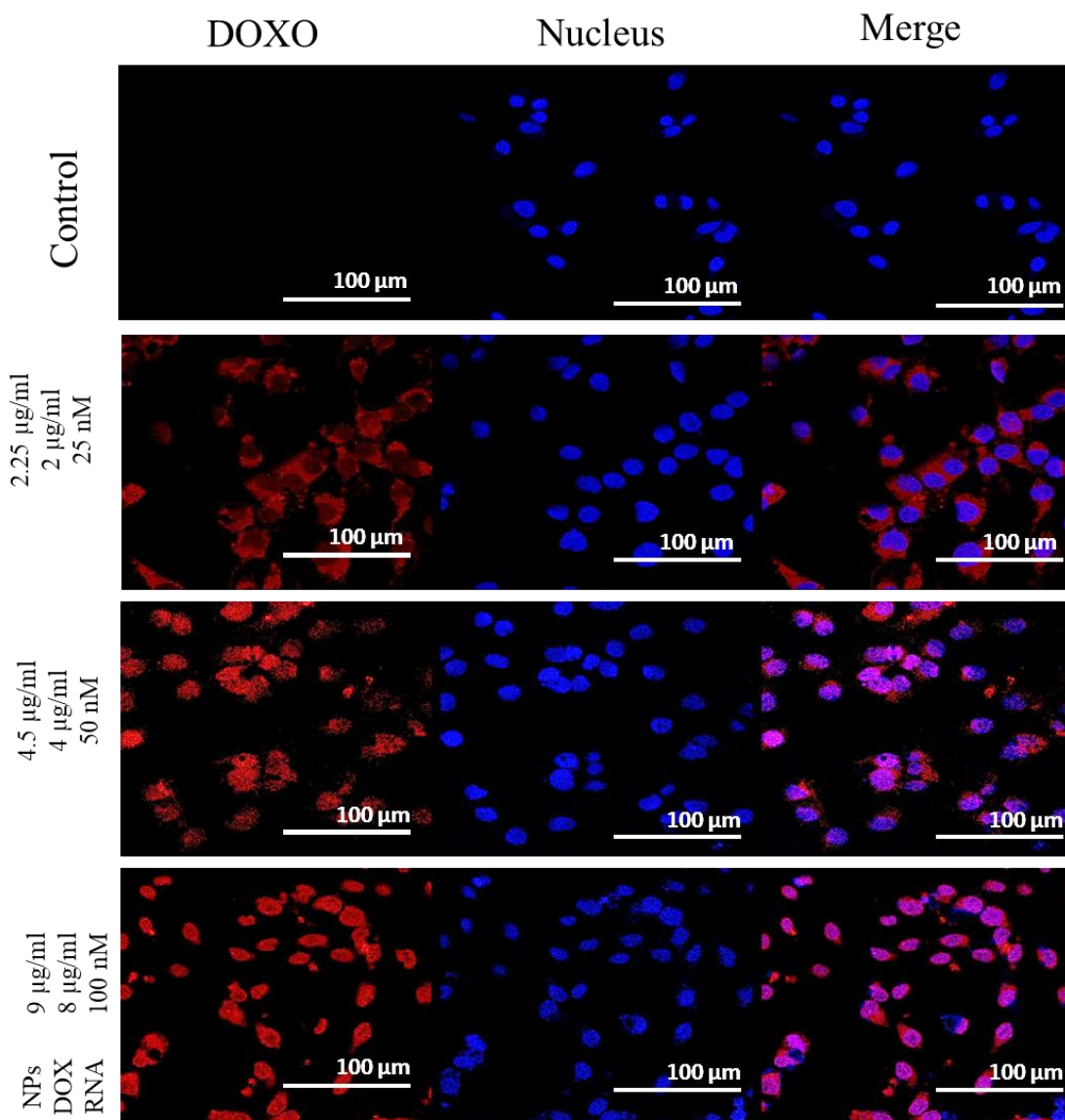
Figure 22. Confocal laser scanning microscopy images showing the location of doxorubicin delivered by PDA nanoparticles into U118 cells. Imaging was performed after 4 h of incubation with at 9 μg/ml, 4.5 μg/ml, and 2.25 μg/ml of PDA@DD@DOXO@RNA NPs. Cells without NPs were used as a control. Hoechst 33342 stained nuclei (blue); DOXO (red).

7.2.4. Phototherapy

In the end, the effectiveness of photothermal therapy using live/dead cell viability assay was checked. To avoid the influence of DOXO on the cell viability results, U118 cells were incubated for 24 h with PDA@DD@RNA NPs at a concentration range of 9 µg/ml and 1.125 µg/ml and 808 nm laser irradiation with a laser power of 3 W was applied. The number of live and dead cells was analyzed using flow cytometry after another 24 h. **Figure 23 A, B** presents that without laser irradiation, there is no difference in cell viability as compared to control cells and the cells remain vital. After irradiation with the laser at the two highest concentrations, a highly significant difference was present. It confirmed the high effectiveness of PT therapy which reduced the amount of living cells to 20% in the case of the highest concentration. The influence of PTT is also shown in the form of microscope images (**Figure 23 C**).
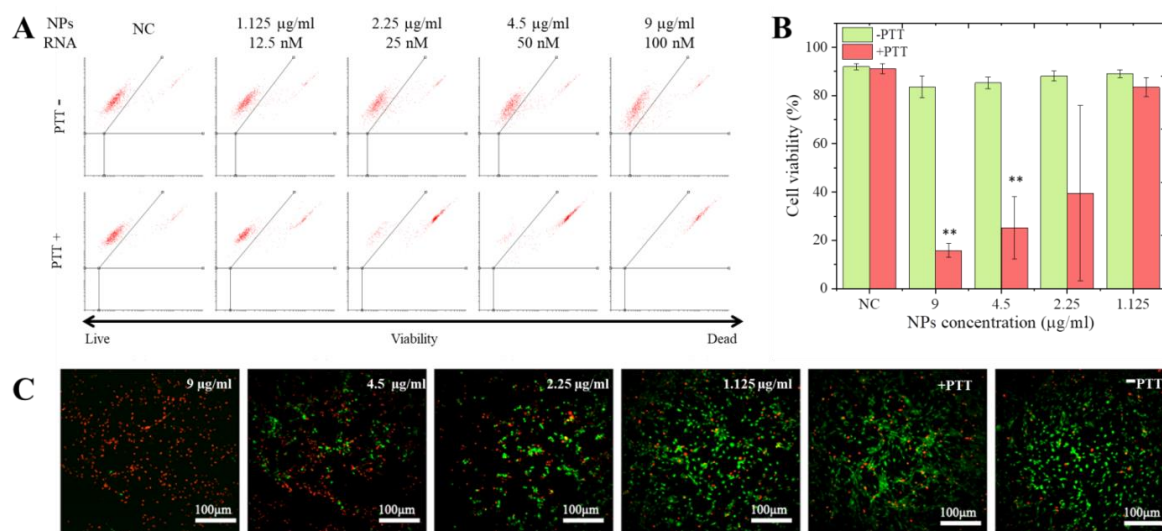
Figure 23. Live/Dead assay of U118 cells after 48 h of incubation with PDA@DD@RNA NPs with (+PTT) and without (-PTT) 808 nm laser irradiation. **A** Dot plots, **B** bar graph showing calculated results from the flow cytometer, and **C** microscope images of live (green) and dead (red) cells. NC: negative control (cells without NPs)

Red signal corresponds to dead cells, and the green signal shows living cells. From the left side, the concentration of NPs is the highest, and on the image are visible mostly dead cells. To the right side, the concentration of NPs decreases, and the number of living cells (green) increases.

The result of combined chemo- and photothermal therapy was investigated using Annexin V assay. For this purpose, the final PDA@DD@DOXO@RNA carrier in combination with 808 nm laser irradiation was used. U118 cells were incubated for 24 h with PDA@DD@RNA NPs at a concentration range of 9 μg/ml and 1.125 μg/ml and 808 nm laser irradiation with a laser power of 3 W was applied. The apoptosis profile of U118 cells was analyzed using flow cytometry after another 24 h. As shown in **Figure 24,** the final form of the carrier is characterized by the high effectiveness of synergistic treatment of glioblastoma cells. As it was described, even without PTT, the amount of apoptotic cells was almost 100% in all samples. DOXO was successfully delivered into the cells and caused the apoptotic death of cells. The late apoptotic cell rate induced by the PDA@DD@DOXO@RNA NPs after laser irradiation was nearly 100% for the whole concentration range. The cells incubated without NPs but irradiated with the laser remained vital.
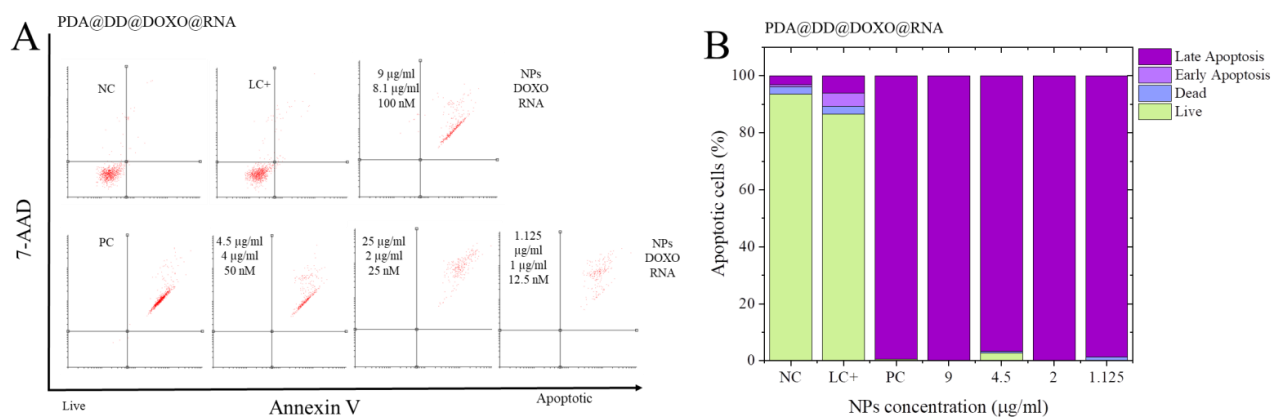
Figure 24. Apoptosis profile of U118 cells after 48 h of incubation with PDA@DD@DOXO@RNA NPs with (+PTT) and without (-PTT) 808 nm laser irradiation evaluated using Annexin V assay. **A** Dot plots and **B** bar graph showing calculated results from the flow cytometer. NC: negative control (cells without NPs), PC: positive control (DOXO 5 µg/ml), LC+: laser control (cells without NPs after laser irradiation)

CHAPTER 3

8. Spherical polydopamine nanoparticles as a base of iron structure growth for potential imaging and cancer therapy

In this chapter, the growth of a iron structure on the PDA NPs surface is described. The required conditions to obtain such structures, and its identification will be described in detail. The influence of iron on the photothermal as well as magnetic properties of PDA NPs is shown. Due to the fact that iron can be used as a contrast agent by T_1 relaxation, the obtained iron-structured NPs can find application in bioimaging. In addition, this type of NPs can serve as a potential therapeutic material for cancer treatment. For this purpose, at the end of the chapter, the cytotoxicity of these NPs on hepatocellular carcinoma cells, is shown. Part of these results were published in the Journal of Physical Chemistry B 2020 "Facile and Controllable Growth of β-FeOOH Nanostructures on Polydopamine Spheres". [85]

8.1. Analysis of iron structure growth on polydopamine nanoparticles

8.1.1. Deposition of iron on polydopamine nanoparticles

A unique iron structure on the surface of 100 nm PDA particles was first acquired at the 1:3 PDA NPs to $FeCl_2$ weight ratio in a water/ethanol mixture after 24 h. To fully understand the formation process of sharp iron structures on PDA NPs, reaction conditions such as the amount of iron, type of solution, and source of iron ions used were investigated.

First, different amounts of $FeCl_2$ were used to determine how much iron is needed to obtain this kind of structure. For this purpose, four samples with different PDA NPs to $FeCl_2$ weight ratios of 3:1, 1:1, 1:3, and 1:5 were prepared. TEM images of PDA NPs with iron structure formation depending on the amount of $FeCl_2$ in the samples are shown in **Figure 25** A-D. **Figure 25 A** presents a sample with the dominance of PDA NPs (weight

ratio 3:1). There is no visible and significant deposition of iron ions on the surface of NPs. At a weight ratio of 1:1, the iron became visible on the TEM image. Still, in the typical shape of the pellet on the NPs surface (**Figure 25 B**). Very well-defined structure in the form of needles is visible in the sample with the dominance of $FeCl_2$ ratio of 1:3 (**Figure 25 C**). With the addition of a larger amount of iron, the structure is even more extended (**Figure 25 D**).

In the next step, the influence of the type of solution on the shape and presence of the iron structure was tested. Two samples were prepared, one in pure ethanol and the second in pure water. In the experiment with ethanol, the nanoparticles were firstly washed a few times with ethanol to remove the whole water in which they were stored. **Figure 25 E and F** show the TEM images of iron-deposited PDA NPs after synthesis in ethanol and water. Deposition in pure ethanol (**Figure 25 E**) affects the iron ions deposition similarly to the sample shown in **Figure 25 B** at 1:1 ratio. It confirms that the deposition was successful but without a unique iron structure formation. In the case of the sample after iron deposition in water (**Figure 25 F**), there are no visible iron ions on the surface of PDA NPs. It suggests that it was essential to use the mixture of water and ethanol to deposit iron ions on PDA NPs to obtain the required unique structure (**Figure 25 G**). In other cases, iron deposition occurs in the form of a pellet.

Next, it was investigated if it was possible to obtain iron structures using other sources of iron. Tests were performed in a previously determined mixture of water and ethanol and a ratio of 1:3 with $FeCl_3$, iron (II) sulfate heptahydrate ($FeSO_4$), and iron (III) acetylacetonate ($C_{15}H_{21}FeO_6$) as a source of iron ions. The TEM images of PDA NPs with iron structures formed depending on the iron source are shown in **Figure 25 H-J**. In the sample with $FeSO_4$ as an iron source (**Figure 25 I**), the results are very similar to the sample with the dominance of PDA, which means that the deposition was not very

effective. Using $C_{15}H_{21}FeO_6$, the presence of iron is not visible on the NPs (**Figure 25 J**). That suggests that the iron from the chloride source is easier to depose on the PDA surface than from other reagents. The literature described only similar structures that authors developed for photocatalytic applications. However, its preparation protocols required higher temperature (30-60 °C), vacuum, hydrochloric acid and, the most important difference, $FeCl_3$ as iron source.[86,87] Comparatively, the protocol developed here of obtaining spiky iron structure on PDA NPs surface required basic conditions, is easy to recreate and nontoxic.
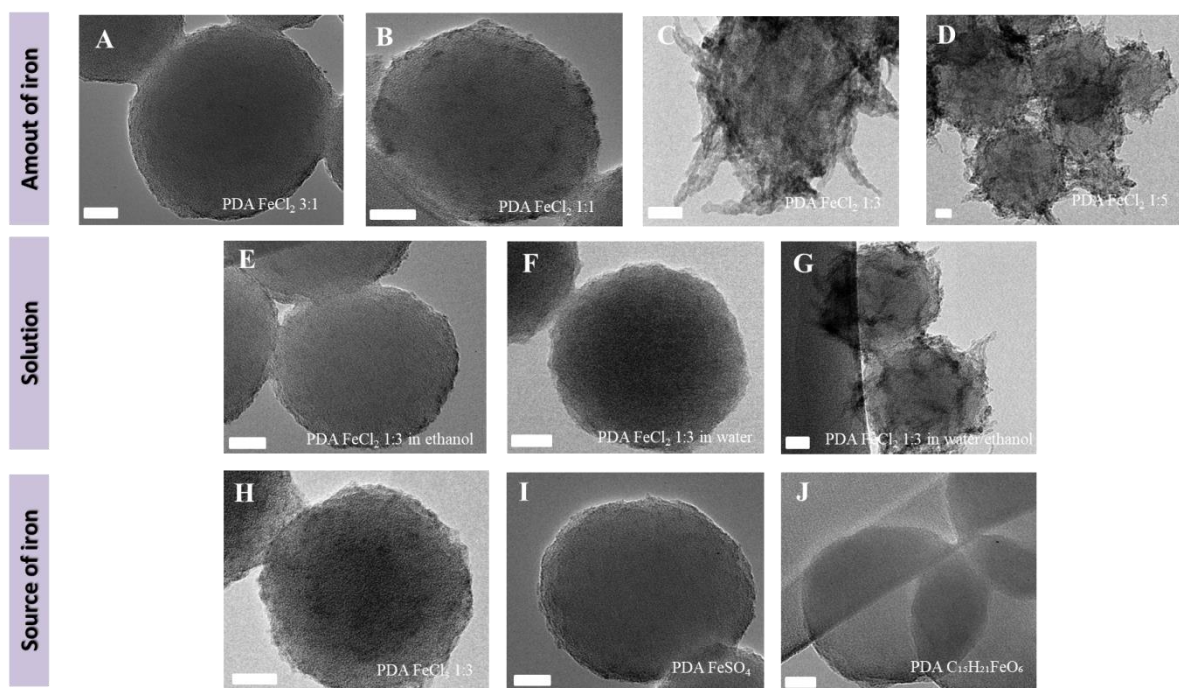
Figure 25. TEM images of PDA nanoparticles obtained after iron deposition using different: amount of iron **A** PDA:$FeCl_2$ 3:1, **B** PDA:$FeCl_2$ 1:1, **C** PDA:$FeCl_2$ 1:3, **D** PDA:$FeCl_2$ 1:5, solutions **E** PDA:$FeCl_2$ 1:3 only in ethanol, **F** PDA:$FeCl_2$ 1:3 only in water, **G** PDA:$FeCl_2$ 1:3 in water/ethanol, and source of iron **H** PDA:$FeCl_3$ 1:3, **I** PDA:$FeSO_4$, **J** PDA:$C_{15}H_{21}FeO_6$. Scale bar, 20 nm. [85]

Zeta potential measurements also confirmed iron deposition as a more sensitive method to detect changes in the charge on the surface of NPs. Values presented in **Table 1** prove that the iron deposition appeared even in the sample at ratio of 3:1 (**sample A**), in water (**sample F**), with the use of $FeSO_4$ (**sample H**) and $C_{15}H_{21}FeO_6$ (**sample I**), even though that iron structures are not visible on the TEM images. The most significant correlation can be observed in the case of samples investigating the influence of the amount of $FeCl_2$ (**sample A, B, C, D**). It shows the general dependence that the increase of zeta potential value is proportional to the amount of iron used and its deposition on PDA NPs. These results suggest that the structure's growth is more effective in an environment with a higher concentration of iron ions in the solution. The highest value (+40 mV) is obtained for the sample at a ratio of 1:5, with the biggest amount of iron used.

Table 1. Zeta potential value of PDA nanoparticles obtained after iron deposition using different: amount of iron **A** PDA:$FeCl_2$ 3:1, **B** PDA:$FeCl_2$ 1:1, **C** PDA:$FeCl_2$ 1:3, **D** PDA:$FeCl_2$ 1:5, solutions **E** PDA:$FeCl_2$ 1:3 only in ethanol, **F** PDA:$FeCl_2$ 1:3 only in water, **G** PDA:$FeCl_2$ 1:3 in water/ethanol, and source of iron **H** PDA:$FeCl_3$ 1:3, **I** PDA:$FeSO_4$, **J** PDA:$C_{15}H_{21}FeO_6$. [85]

	A	B	C	D	E	F	G	H	I	J
Zeta potential (mV)	+16.5	+20.5	+38.0	+39.5	+21.5	-12.5	+38.0	+34.0	+14.0	-23.0
Sample	PDA $FeCl_2$ 3:1	PDA $FeCl_2$ 1:1	PDA $FeCl_2$ 1:3	PDA $FeCl_2$ 1:5	PDA $FeCl_2$ 1:3 in ethanol	PDA $FeCl_2$ 1:3 in water	PDA $FeCl_2$ 1:3 in water/ ethanol	PDA $FeCl_3$ 1:3	PDA $FeSO_4$ 1:3	PDA $C_{15}H_{21}FeO_6$ 1:3

8.1.2. Time-dependent growth of the iron structure and iron content analysis

After identifying the essential conditions of the synthesis of iron on PDA NPs, an investigation of the specific growth of the spiky iron structure was performed. For this

purpose, a time-related experiment was conducted by collecting a part of the solution from the primary synthesis after 3 h, 6 h, 12 h, 24 h, 48 h, and 120 h. All samples were visualized using HR-TEM and characterized by energy-dispersive spectroscopy (EDS).

HR-TEM images shown in **Figure 26** present the iron corona growth on the NPs. In the sample collected after 3 h (**Figure 26 A**) some tiny seeds of iron (marked with red circles) are visible. The growth of these seeds as well as their increased number in the following samples, is observed with time (**Figure 26 B**). After 12 h (**Figure 26 C**), the structure started to be defined in a more spiky shape. After 48 h, iron covered the whole surface of the NPs. Furthermore, the form of iron became very similar to the crystal structure (red arrows) (**Figure 26 E, F**). The growth was also investigated using zeta potential measurements. In the **Table 2** are presented values corresponding to the TEM images samples. It is visible that with time, the zeta potential increases proportionately to the amount of iron deposited on the surface.

In the next step, EDS characterization of the same samples was performed. Iron (red) and carbon (green) atoms were detected. Carbon is the most common element of PDA structure. EDS also allows the iron concentration to be estimated. Results were presented as a combination of the calculated amount of iron and an EDS map of the iron distribution. As shown in **Figure 26 G**, an increase of iron ions with time and deposited ions growth in a specific spiky shape was observed. The images also confirmed that iron ions were present only on the surface of NPs. The measured concentration of iron in samples increased from 5% to around 35% after 120 h of deposition.
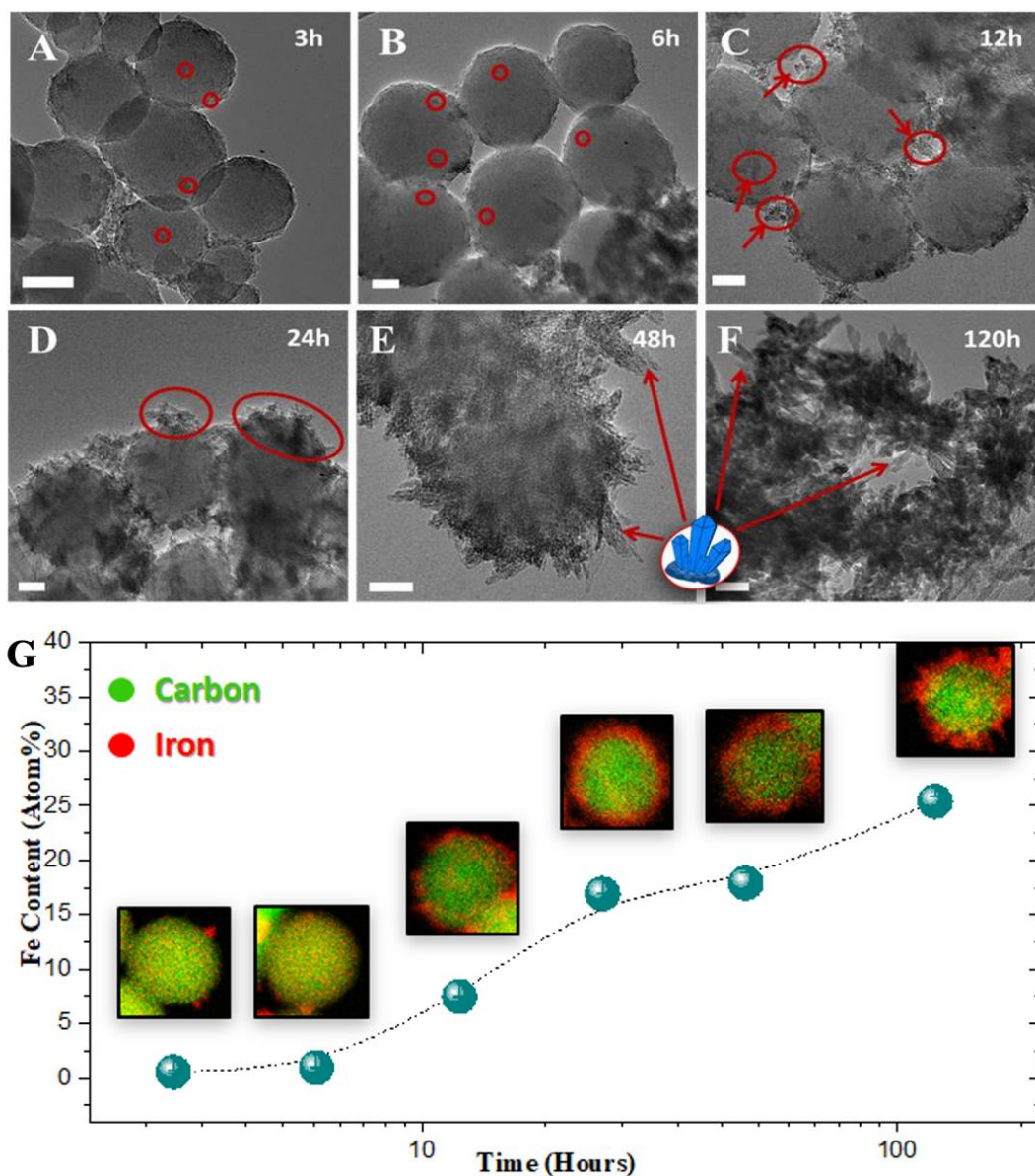
Figure 26. A-F HR-TEM images showing growth of iron structure on PDA NPs surface.

G The iron content change over time. [85]

Table 2. Zeta potential value change corresponds to the time of growth of iron structure at day of synthesis (day 0) and day 7. [85]

Sample		A 3h	B 6h	C 12h	D 24h	E 48h	F 120h
Zeta potential (mV)	Day 0	-25.0	-16.0	-6.5	+38.0	+38.0	+40.0
	Day 7	-31.0	-30.5	-26.0	-22.5	-20.0	-15.0

8.1.3. Stability of iron structure in time

To assess the stability of the obtained iron structure, TEM imaging was performed after one week. For this purpose, on pure PDA NPs (**Figure 27 A**) were deposited with iron ions using $FeCl_2$ in a ratio of 1:3 over 24 h (**Figure 27 B**). After one week of storage in a fridge, the sample was centrifuged and investigated. It is visible in **Figure 27 C** that the spiky iron structure disappeared. On the surface of NPs are present only some seeds of iron. It proved that characteristic iron structure degraded in time, which can be used as an advantage in the treatment by ferroptosis. Additionally, the degradation is also visible in decreasing zeta potential values presented in the second part of **Table 2**. Each sample characterized by time presents a high decrease of zeta potential value; after 7 days, all achieved values below zero. Sample after 3 h, 6 h, 12 h of deposition rich around –30 mV, which is the value of pure PDA NPs surface charge and confirmed complete disconnection of iron from the surface.
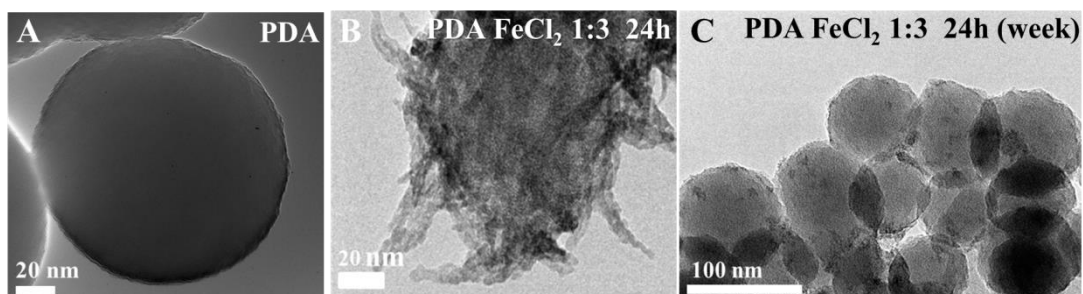
Figure 27. TEM images showing stability of iron structure on PDA NPs: **A** pure PDA NPs, **B** sample after 24 h of growth, **C** sample after 7 days. [85]

8.1.4. Iron structure identification

The next step was to identify the iron structure obtained on PDA NPs. HR-TEM imaging and performed EELS signal quantification were performed to investigate the

elements and iron distribution on the surface of PDA NPs. The obtained data was analyzed, and the structure of iron hydroxide was identified.

First, the energy distance between oxygen and iron peaks was analyzed. The position of the L3 peak doesn't change like an edge between oxygen and iron, which confirms the single valence state of iron. Then the average spectrum was compared with the reference spectra. [88] Iron was identified as Fe^{3+}, which corresponded to hematite or goethite. The identification of iron crystallographic structure was evaluated based on collected SAED patterns. For this purpose, several electron diffraction patterns were collected from different areas of the sample after 120 h of iron deposition. They were then examined using the DiffTools program. The crystalline spots were gathered and tabulated on a Cu-based diffractogram (= 1.5406) according to their interplanar distance (d) and equivalent 2 angles. This led to identifying the Fe nanostructure as β-FeOOH with a minor amount of β-FeOOH. In β-FeOOH, the chain of 4 $FeO_3(OH)_3$ octahedra is entangled to form a nanoporous channel (about 0.25 nm^2).

The porous structure is partially filled by Cl^- ions, which are attracted by the H^+. This is not the case for the γ-FeOOH. Thus, this suggests that $FeCl_2$ as a precursor promotes the stabilization of β-FeOOH on the PDA surfaces, but in contrast, the use of $FeSO_4$ promotes the growth of the γ-FeOOH phase.

8.2. Magnetic properties

The magnetic response of composite materials is crucial in determining their potential future applications. Pure PDA frequently exhibits paramagnetic properties, and in the investigated temperature range, the magnetization value does not exceed 0.12 emu/g in a magnetic field of 0.1 T. **Figure 28** displays the outcomes of the magnetic measurements for the PDA@-FeOOH 120 h sample, where magnetization is based on the total weight of the entire sample. As the temperature dropped, the magnetization in each sample rose

gradually, as is typical of paramagnets. The zero-field-cooled (ZFC) and FC curves overlap without a bifurcation, and no signs of long-/short-range magnetic order or anomalies related to the superparamagnetic effect were seen. All this may indicate the paramagnetic properties of the tested materials. Based on further analysis and published in a paper, it can be concluded that magnetic measurements agree with the previously presented literature for nanosized β-FeOOH. [89,90]
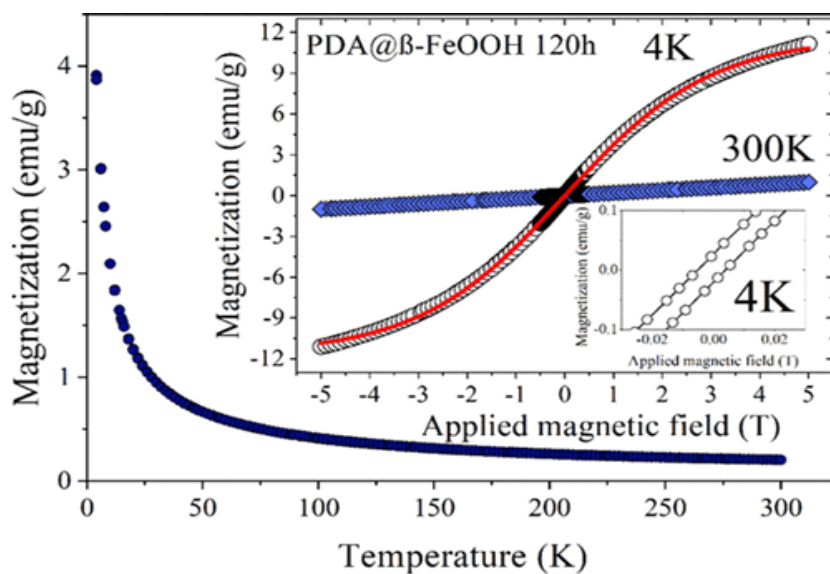
Figure 28. Temperature dependence of the zero-field-cooled (ZFC) magnetization of the PDA@β-FeOOH 120 h sample was measured in the applied magnetic field of 0.1 T. The inset shows magnetization curves collected at 4 and 300 K. [85]

8.3. Influence of iron structure on photothermal properties of polydopamine nanoparticles

One of the most significant advantages of PDA is its wide absorption range which leads to the conversion of infrared laser light (808 nm) into heat. It is known that metal ions can also emit heat due to irradiation with laser light. It was expected that the presence of the β-FeOOH structure on the surface of nanoparticles could further improve their PT properties.

PT measurements were performed under the same conditions as pure PDA NPs in a quartz cuvette and irradiated using 2 W laser power. Due to visible differences in the shape of iron samples after 24 h, 48 h, and 120 h, their PT properties were analyzed. NPs were prepared in five different concentrations: 10 μg/ml, 25 μg/ml, 50 μg/ml, 75 μg/ml, and 100 μg/ml in 1 ml of water. 1 ml of pure water was used as a control. Each sample was irradiated for 10 min with a laser wavelength of 808 nm. As shown in **Figure 29 A, B, C** the improvement of PT properties was observed for all samples containing iron (PDA@β-FeOOH NPs) in the whole concentration range tested compared to pure PDA NPs. The highest temperature change in the case of pure PDA NPs after irradiation with 2 W laser power was around 35 °C. In the case PDA@β-FeOOH NPs the highest temperature change achieved value over 40 °C. It proved the improvement of PT properties because of presence β-FeOOH on the NPs surface. Additionally, an interesting conclusion is that there is no visible difference in temperature change between samples with different times of iron structure growth (**Figure 29 A, B, C**). The results confirmed that as it was shown that the morphological shape of the iron structure, i.e. more rank in space in the sample after 120 h of iron growth, does not affect the PT properties. It can be a result of containing the same amount of iron on nanoparticles after 24 h, 48 h, and 120 h of iron deposition.

Therefore, the photostability measurements were only performed on the sample after 24 h of iron deposition at a concentration of 50 μg/ml. The experiment consisted of five five-minute irradiation cycles of each sample and reconversion to the initial temperature. **Figure 29 D** shows that the highest temperature amplitude was observed in the first cycle. The second cycle maximum consisted of only half the value of the first increase. With each subsequent cycle, the temperature change was also decreasing. Due to, changing concentration of PDA@β-FeOOH in the solution because of sedimentation (**Figure 29 D**). It should also be emphasized that in the case of samples with β-FeOOH on

the surface, the sedimentation process and NPs accumulation appeared on the magnetic dipole.
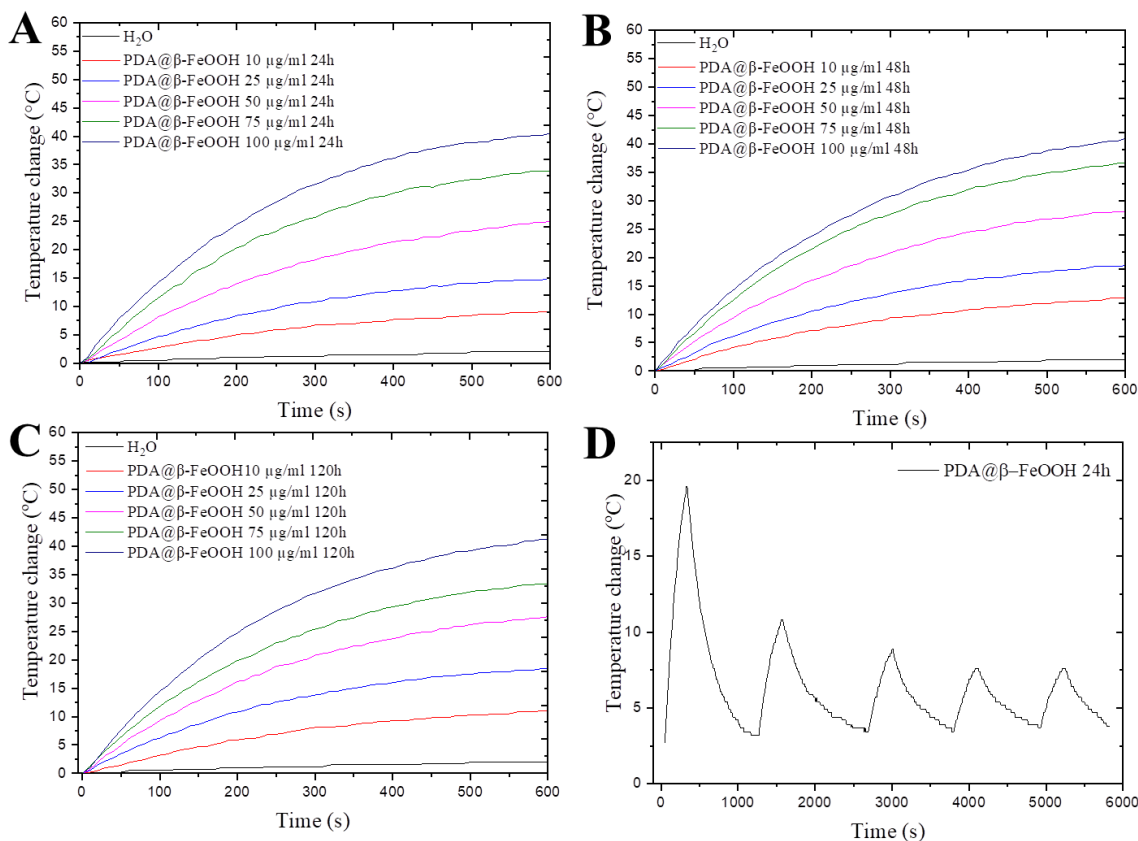
Figure 29. **A** Temperature change and **B** stability (50 µg/ml) of PDA NPs after irradiation with 808 laser light with a power of 2 W. **C** Temperature change and **D** stability (50 µg/ml) of PDA@β-FeOOH 24h NPs after laser irradiation with a power of 2W. Temperature change after irradiation with 2W **E** PDA@β-FeOOH 48h NPs and **F** PDA@β-FeOOH 120h NPs.

8.4. Cytotoxicity of nanoparticles

The research was focused on investigating if cell death can be caused by ferroptotic cell death mechanism. Based on stability experiment results, the β-FeOOH disappeared in less than 7 days. Ferroptosis is a recently identified form of cell death that is iron-

dependent and characterized by rising levels of lipid peroxides. It has been identified as a mechanism of cell death in Parkinson's and Huntington's diseases, as well as in sepsis. It plays an important role in the treatment of cancer and may contribute to tissue degradation in brain injury, kidney disease, and asthma. Due to the most important aspect of the use of this mechanism is its control and appearance only in specific cells. Ferroptosis is interesting to scientists but is still a poorly understood process.[91–93]

Cell viability assays were performed to investigate the general influence of iron structure on PDA NPs and the subsequent therapeutic effect. Cytotoxicity of PDA@β-FeOOH NPs was evaluated on HepG2 cells after 24 h and 48 h of incubation using WST-1 calorimetric assay. As shown in **Figure 30 A, B**, even after incubating cells with PDA@β-FeOOH for 48 h, there is no visible and statistically significant decrease in cell viability. It proved that the cells were still metabolically active and proliferating.
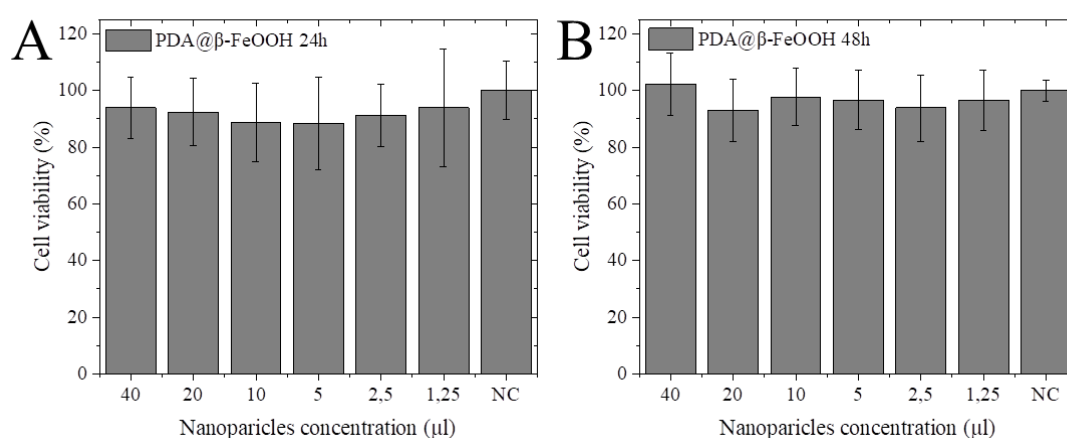
Figure 30. Cell viability of HepG2 cells after incubation with PDA@β-FeOOH NPs for **A** 24 h and **B** 48 h. NC: negative control (cells incubated without NPs)

Lipid peroxidation in ferroptosis can be initiated by radicals: hydroxy (• OH), hydroperoxide (HO •) being the protonated form of O •, oxide nitrogen (NO •), perferryl, and lipids radicals: peroxide (LOO •), alkoxy (LO •) and alkyl (L •). The initiation result is

free alkyl radicals which react with oxygen in the prolongation (propagation) reactions to form peroxide free radicals. Peroxide radicals located at the end of the system of double bonds react with subsequent molecules of polyunsaturated fatty acids to give peroxides (hydroperoxides) of fatty acids (LOOH). Singlet oxygen can also form LOOH, but by the addition of an oxygen molecule to a double bond. The hydroperoxides thus formed are the first lipid peroxidation products to be relatively stable in the absence of transition metal ions. [91,93,94] To test whether the iron on the nanoparticles can generate reactive oxygen species (ROS), an oxidative stress assay was carried out using flow cytometry. The HepG2 cells were incubated with PDA@β-FeOOH NPs for 24 h and 48 h. As shown in **Figure 31**, there is no significant change in ROS generation by cells exposed to PDA@β-FeOOH NPs over the entire concentration range as compared to nontreated cells.

More detailed experiments have to be performed to confirm the possibility of inducing ferroptosis using PDA@β-FeOOH NPs by lipid radicals.
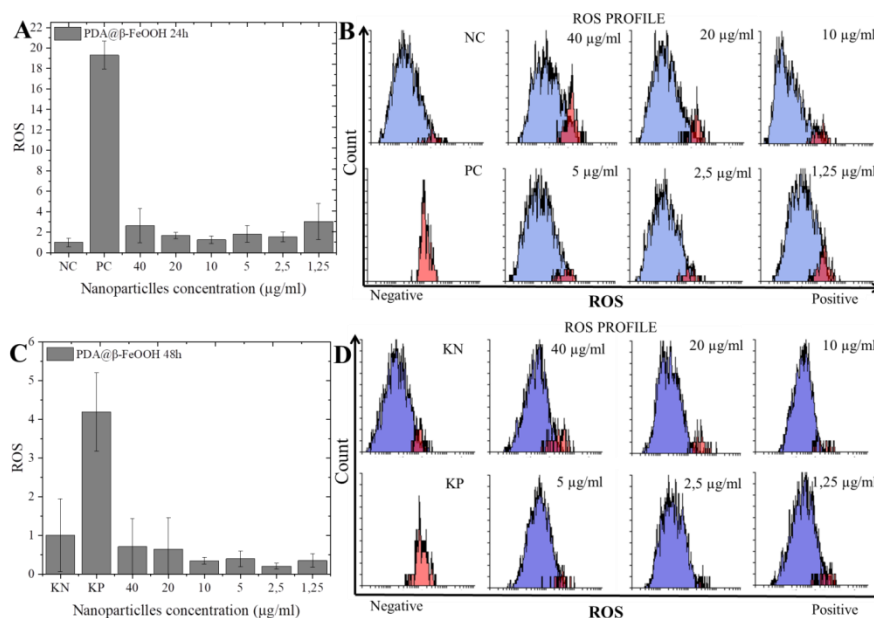
Figure 31. Relative ROS production (**A, C**) and ROS profiles (**B, D**) for HepG2 cells incubated with PDA@β-FeOOH NPs evaluated by flow cytometry (blue—ROS negative cells; red—ROS positive cells). NC: negative control (non-treated cells), PC: positive control (cells treated with 1 mM menadione)

CHAPTER 4

9. Spherical core-shell nanoparticles using polydopamine as a transporter of hydrophobic curcumin

In this chapter, the approach taking advantage of the water insolubility of curcumin and the excellent adhesive properties of PDA is demonstrated. Curcumin is used as a core of the NPs and PDA as a shell. The result of this research is the development of core-shell NPs susceptible to CUR delivery to the cell in combination with DOXO and PTT.

9.1. Development of core-shell nanoparticles

To obtain core-shell NPs based on curcumin crystals and PDA coating, a modified protocol of Junhui Xue *et al* was used. [95] In the original study, the authors used CUR crystals as a template to get PDA tubes. The protocol was based on dissolving CUR in a 1:1 mixture of ethanol and acetone, followed by the addition of water and DOPA. Because of the insolubility of CUR in water, the addition of water induces crystallization. To start DOPA polymerization, TRIS buffer was added to the solution. After 24 h, CUR was efficiently removed using ethanol. This suggests that CUR was not covalently bound to PDA.

First, the original protocol was repeated with slight modification, and the only difference was the CUR crystallization time. The authors waited a specific amount of time to form CUR crystals. In this research were needed NPs, with the size in range between 20 nm to 200 nm. To achieved that the smallest size of CUR crystals were required. Due to, time of CUR was reduced to a minimum and TRIS buffer was added to the solution just after DOPA was dissolved to reduce the time of crystallization. After 24 h of the synthesis process, the NPs were purified with water by centrifugation several times. As shown in **Figure 32 A**, the size of obtained NPs was over 500 nm in diameter.
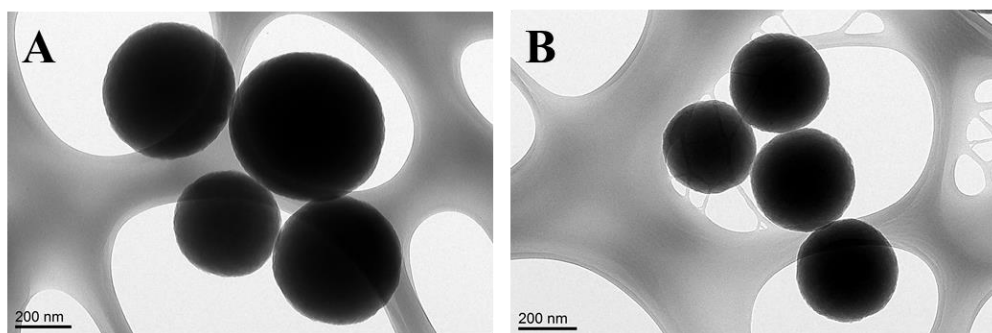
Figure 32. TEM images of CUR@PDA particles **A** after repeating synthesis protocol, **B** after reducing volume of alcohol in the solution to 35 ml.

During the optimization of this protocol, the biggest issue in obtaining particles in the nano-size range was the presence of alcohol in the polymerization solution. The influence of alcohol on DOPA polymerization was investigated by Xue *et al*. [95] For this purpose, the authors tested different ratios between water:ethanol:aceton in the mixture to obtain PDA tubes with very smooth surfaces. In this work, the obtained particles visible in **Figure 32** were also characterized by a very smooth surface, and defined spherical structure. A further study by Jiang *et al* demonstrated that the presence of alcohol affects not only the structure of the particles but also their size.[96] Based on this research, it was noticed that to obtain smaller NPs it's necessary to use the smallest possible amount of alcohol in the solution.

In this study, the use of alcohol was necessary to dissolve CUR and cover it with PDA. The essential aspect was to determine the smallest amount of ethanol:acetate mixture in the solution. Therefore, experiments were conducted with a constant volume of water (100 ml) in the solution and different volumes of ethanol:aceton mixture. The volume of 35 ml of the alcohol mixture was determined as the lowest volume allowing the successful dissolution of the CUR during the synthesis. Once the CUR was well dispersed, the solution turned yellow (honey) and transparent. The addition of fewer than 35 ml of

alcohol caused the CUR to crystallize rapidly upon the addition of water, which was clearly seen by the change in color (orange juice) and turbidity of the solution. The synthesis of CUR@PDA NPs was performed for 17 h with 35 ml of alcohol. As a result, particles with a 350 nm diameter were obtained (**Figure 32 B**), which is still over the required size of the carrier for the drug delivery system.

The next step was to test the correlation between the amount of curcumin and DOPA in the solution. However, it resulted in no change in the size of the nanoparticles. Therefore, it was decided to further modify the protocol in order to obtain NPs below 100 nm in diameter. For this purpose, NaOH solution was used as previously described for pure PDA NPs. To investigate the influence of NaOH on the synthesis of core-shell NPs 4 flat bottom flasks were prepared. Each flask was filled with the same amount of water/ethanol mixture, curcumin, dopamine, and Tris buffer. The difference was the quantity of NaOH added to the solution just after the dissolution of CUR and DOPA. The selected values were 0.4 ml, 0.5 ml, 0.7 ml, 1 ml, and without 1M NaOH (as previously described). Synthesis was carried out for 17 h with constant mixing on a magnetic stirrer at RT. After that, NPs were purified by centrifugation (22 000 rpm, 40 min). It was observed that purification was successful in the case of samples with 0.4 ml and 0.5 ml NaOH (**Figure 33 C, D**). In other samples, the centrifugation was not sufficient to collect all NPs. A fraction of particles could be separated for a sample with 0.7 ml of NaOH, but the color of the solution was intensely black after centrifugation. This means that the solution was very stable and contained small NP (**Figure 33 A**). In the case of the sample with 1 ml of NaOH added, it was not possible to collect NPs after centrifugation, by extending the centrifugation time or using dialysis. Even after 2 months, the sample was left in the laboratory in a stable vertical position at room temperature, and no sedimentation was

observed. A deep investigation of this sample morphology is expected in future stages and continuation of this work.
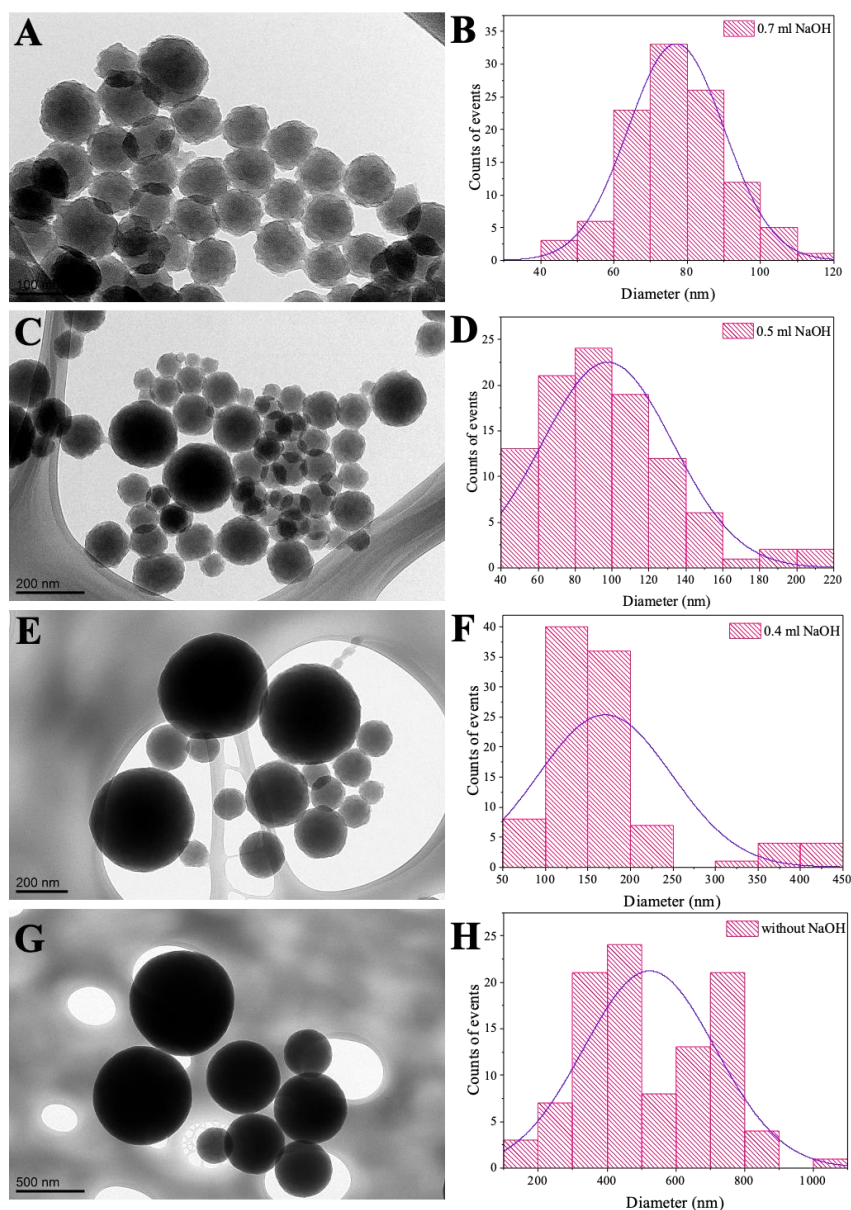
Figure 33. TEM images and histograms showing the morphology and size of CUR@PDA particles after synthesis with addition of **A, B** 0.7 ml NaOH, **C, D** 0.5 ml NaOH, **E, F** 0.2 ml NaOH, and **G, H** without NaOH.

HR-TEM was used to perform an investigation of the possible structure of CUR in the CUR@PDA NPs. Due to the synthesis protocol based on the addition of water to the

solution mixture, it was possible that part of the CUR could create crystals entrapped in the PDA shell. High magnification of a specific area of the CUR@PDA NPs can show the crystal patterns in the structure of NPs. Based on the obtained images (**Figure 34**), no visible crystallographic patterns, which would confirm that CUR did not form crystals during synthesis. Also, electron diffraction experiments showed no crystallinity in the samples. Thus, it is also possible that CUR cannot be placed only in the core of NPs. It is possible that CUR can be present through whole NPs and also on the surface, but most definitely in an amorphous phase.
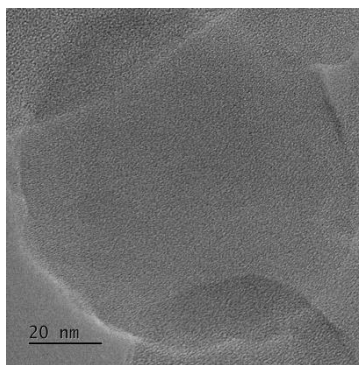
Figure 34. HR-TEM image of CUR@PDA NPs confirming the absence of the CUR crystal pattern in the structure of NPs.

9.1.1. Confirmation of curcumin presence in nanoparticles structure

FTIR spectra were collected to confirm the presence of CUR in CUR@PDA NPs and its influence on PDA structure. **Figure 35** shows the spectra of CUR@PDA NPs and curcumin itself. The CUR spectrum shows a stretching vibration at 1628 cm^{-1} attributed predominantly to overlapping alkenes (C=C) and carbonyl (C=O) stretching vibrations. The O-H groups shows stretching vibration at 3200–3500 cm^{-1}. Further, at 1512 cm^{-1} is visible high intensity signal connected to vibrations ν(C=O), vibrations around aliphatic δ CC-C, δ CC=O. Carbon bonds from aromatic ring shows C=C stretching vibration at 1427 cm^{-1}. At 1512 cm^{-1} are visible also vibrations from aromatic ring δ CC-H of keto and enol

configurations and stretching vibrations around aromatic vCC bonds. In the end, a significant intense bond at 1277 cm^{-1} which is representing vibration of the phenolic bond (C-O). [97,98]

The FTIR spectrum of CUR@PDA NPs shows the signals from the polydopamine described in Chapter 1 and the FTIR spectrum characteristic for CUR. On the first side is the visible complexity of the CUR compared to PDA, which was less detailed. In the spectrum of CUR@PDA NPs, sharp signals from bonds corresponding to aromatic rings (1427 cm^{-1}, 1512 cm^{-1}) and phenolic bond (1277 cm^{-1}) derived from CUR are visible. This confirmed the presence of CUR in the CUR@PDA NPs. These signals were also visible in the structure of PDAs due to the presence of similar components in their chemical composition. Both elements (CUR and PDA) are mainly composed of carbon, hydrogen and oxygen, which create aromatic structures. However, in the case of PDA, the signals were much wider, and their intensity was lower. This may be due to the unpredictable structure of the PDA that has not been fully described, and ultimately it is a mix of different connection possibilities presented in the introduction. On the other hand, the chemical structure of CUR is well-defined, its composition is homogeneous, and its spectrum is very distinct. The obtained spectrum of CUR@ PDA nanoparticles confirmed the presence of CUR in their structure due to the increase in the intensity of specific bonds in the form of sharp peaks, which were not present in the pure PDA spectrum. [99] The CUR spectrum has one additional peak of around 3560 cm^{-1} corresponding to the phenolic hydroxyl stretching vibration. According to literature data, the disappearance of this signal indicates a non-covalent hydrogen bond between CUR and PDA. [100] It may also indicate that the CUR is entrapped in the inner core of CUR@PDA NPs and may be susceptible to release.
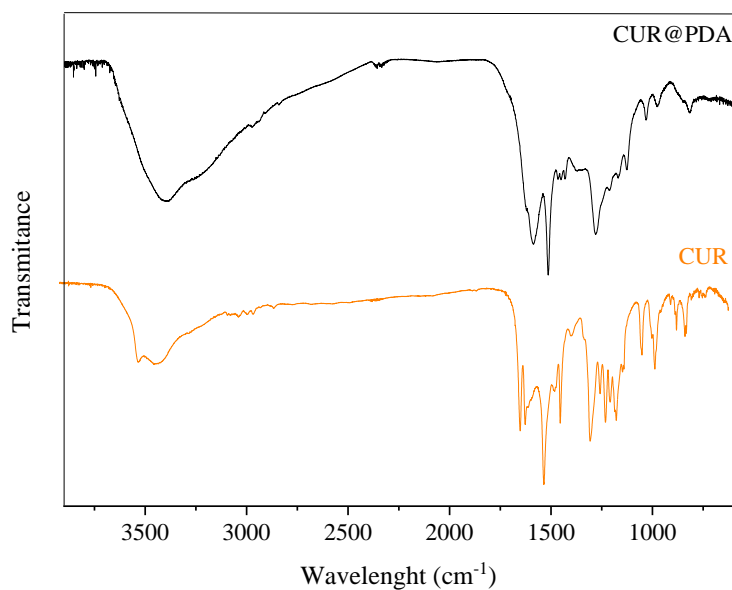
Figure 35. FTIR spectra of pure CUR and CUR@PDA NPs.

9.1.2. Curcumin contents

CUR was measured using UV-Vis method. First, calibration curve was performed by measuring the known concentration of CUR in the reaction. This curve shows a correlation between the concentration of CUR and measured absorption and can be used to determine CUR concentration based on the absorption value.

➢ Curcumin content in CUR@PDA particles with a diameter over 300 nm after synthesis without NaOH addition:

The procedure used to calculate the CUR content in particles with a diameter over 300 nm is presented in **Figure 36**, which is also a graphical interpretation of EE % and LC %. Knowing the mass of the CUR used for synthesis and calculated mass of CUR in the solution after synthesis using a calibration curve, the total amount of the CUR in CUR@PDA NPs was calculated.
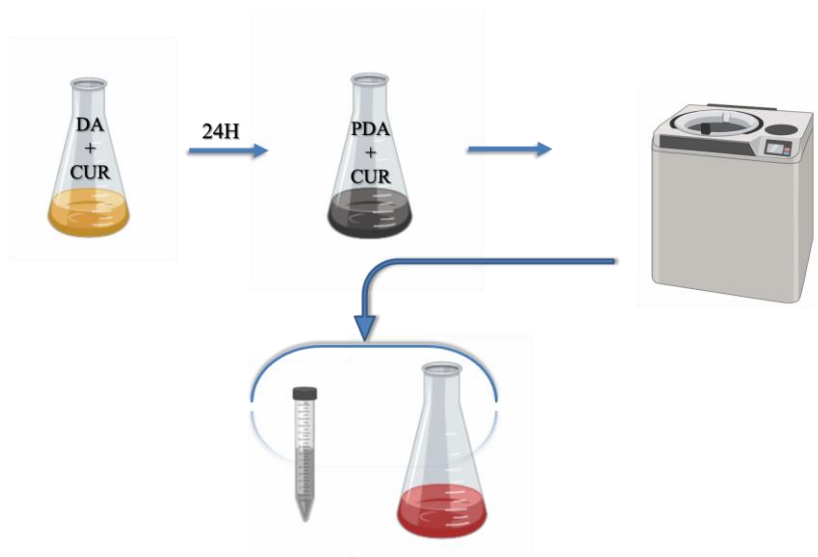
Figure 36. Schematic presentation of the procedure used to calculate CUR content in CUR@PDA particles.

Obtained results showed high repeatability of the CUR content of 0.8. mg CUR in 1 mg of CUR@PDA (LC % = 80, EE % = 74). The content of CUR in these NPs was checked each time to investigate if size manipulation by the amount of alcohol added affected the amount of CUR. These results show that the total content of CUR was an independent value, and particles with 500 nm and 350 nm diameter had the same amount of CUR per 1 mg of material. These particles were not used in further research because of their size.

➤ Curcumin content in CUR@PDA NPs with a diameter below 100 nm after synthesis with NaOH addition:

The calculation method of CUR content was developed for chosen CUR@PDA NPs with diameters below 100 nm after synthesis with the addition of NaOH. The problem was separating NPs after synthesis from the solution, as described above. It was not possible to separate whole NPs from the solution. The only way to determine the amount of CUR was a dissolution of the known amount of CUR@PDA NPs (1 mg) in ethanol to

remove CUR from the structure (**Figure 37**). The ethanol solution was exchanged to receive a clear transparent solution. Released CUR was measured using UV-Vis spectroscopy and calculated using the prepared calibration curve. In this synthesis, the contents of CUR are 0.2 mg in 1 mg of NPs (LC % = 30). It was a smaller value than in the case of bigger particles.

Figure 37.   Image showing the release of CUR from 1 mg of CUR@PDA NPs after placing NPs in ethanol.

9.1.3.   Curcumin Release

The small release was observed only in samples placed at pH 9.5, which can be explained by PDA degradation in a highly alkaline solution. [101] The possibility of CUR release from CUR@PDA NPs was proven by placing NPs in ethanol to calculate the CUR content. For this reason, the addition was performed under artificial conditions in a 1:1 water/ethanol mixture. Obtained results are shown in **Figure 38**. The biggest release is seen in the first few hours and decreases over time. The most important fact is that it was confirmed that CUR is in the available form to be removed from NPs structure. In the literature, there are examples of the release of CUR in mixtures of water and alcohols, with the addition of Tween to support the release or using a very high amount of carrier. [102,103] The most effective release can be observed in biodegradable materials like alginate. [104] However, all these results can prove that CUR is transported in available form and can be easily released in appropriate conditions, which was also proved in this

work. It is known that cell environment is more complex than chemical buffers. Therefore, the release in cells can be different and requires further analysis using biological assays.
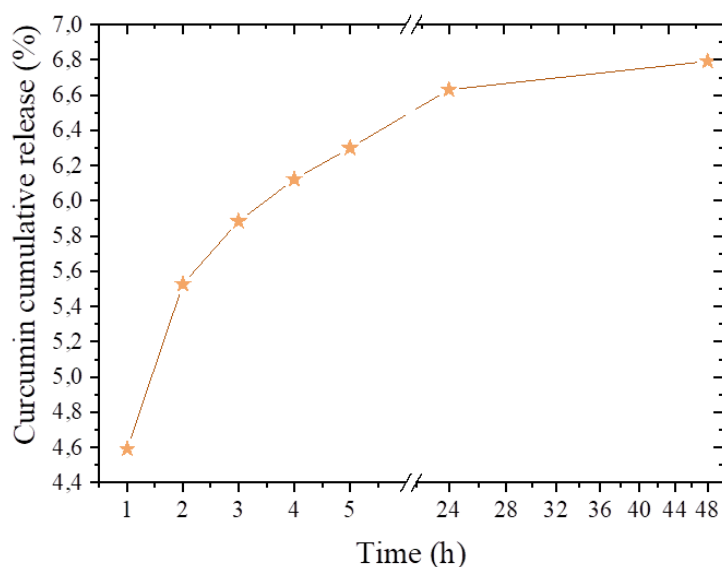
Figure 38. The release of CUR from CUR@PDA NPs in a water/ethanol mixture over 48 h.

9.2. Photothermal properties of core-shell nanoparticles

To investigate photothermal properties of 90 nm diameter CUR@PDA NPs, temperature increase was measured in the samples after irradiation with infrared laser light. NPs were prepared in five different concentrations: 10 µg/ml, 25 µg/ml, 50 µg/ml, 75 µg/ml, and 100 µg/ml in 1 ml of water. Pure water was used as a control sample. Constant conditions allowed to compare the obtained results with pure PDA NPs and to analyze the influence of the CUR present in the structure on PT properties. CUR@PDA NPs were measured over 10 min under irradiation with laser light of 808 nm wavelength and laser power of 3 W, 2 W, and 1 W (**Figure 39 A, B, C**). As shown in **Figure 39 C**, the highest temperature change was recorded for the 100 µg/ml sample after irradiation of 3 W. The achieved value of around 50 °C was even higher than it was observed for pure PDA NPs. It confirmed that CUR does not decrease PT properties of NPs and can be successfully used

in PT therapy. Additionally, there is no visible change in the photostability of the NPs (**Figure 39 D**) after five cycles of irradiation with a laser power of 2 W. It proved that NPs are also stable in solution over time.
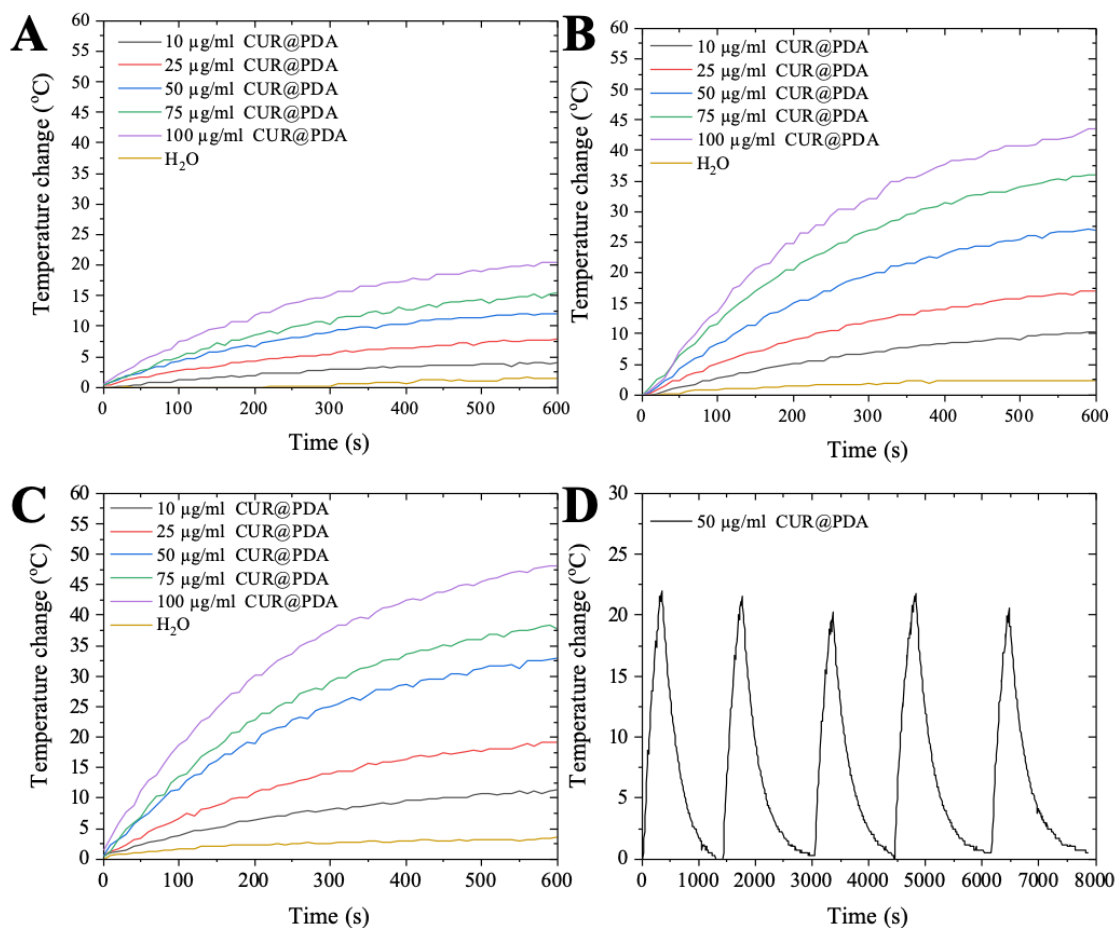
Figure 39. Temperature change after CUR@PDA NPs laser irradiation (808 nm) over 10 min with a laser power of **A** 1 W, **B** 2 W, **C** 3 W. **D** Temperature change in photostability measurements under irradiation with a laser power of 2 W.

CHAPTER 5

10. Core-shell type nanoparticles with a curcumin core and polydopamine shell for enhanced chemo/phototherapy

This chapter presents the surface functionalization of the 90 nm CUR@PDA NPs with PAMAM dendrimers and doxorubicin. The CUR@PDA NPs are examined for their cytotoxicity and combined treatment efficiency on cancer cells. A graphical presentation of the procedure used to functionalize and apply the combined chemo- and photothermal therapy is shown in **Figure 40** .
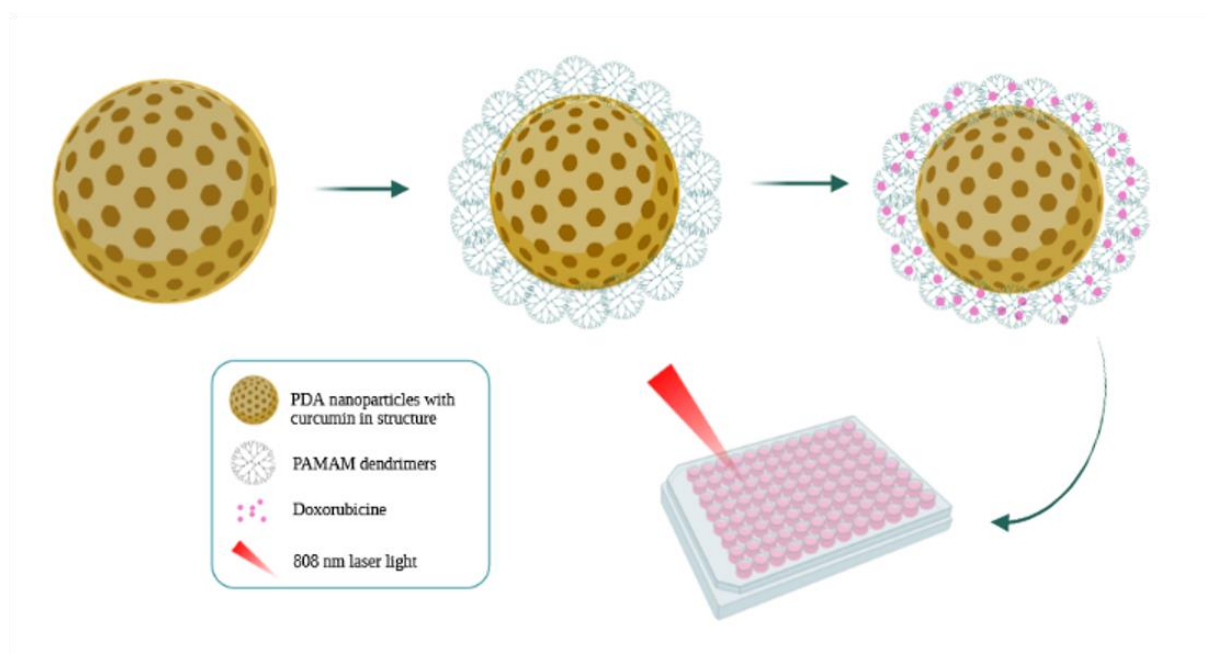
Figure 40. Schematic presentation of the use of PAMAM dendrimers and DOXO functionalized CUR@PDA NPs for combined chemo and phototherapy of cancer cells.

10.1. Surface functionalization of core-shell NPs with PAMAM dendrimers

Because of the presence of CUR in the entire structure of CUR@PDA NPs, it was possible that it could affect further surface functionalization. Functionalization of CUR@PDA NPs with PAMAM dendrimers was performed at the same parameters as for pure PDA NPs. This process was conducted overnight at RT at a 1:3 CUR@PDA NPs to

PAMAM dendrimers ratio. The next day, the sample was purified by centrifugation (22 000 rpm, 20 min) and washed three times with Milli-Q water.

Zeta potential values showed that CUR@PDA NPs had higher surface charge (−20 mV) than pure PDA NPs (−30 mV). This confirmed the earlier hypothesis that CUR is present in the entire structure of NPs, even on their surface. ξ potential value of the CUR@PDA@DD NPs increased to +36 mV (**Figure 41**). This result confirmed that the functionalization with PAMAM dendrimers was successful despite the presence of CUR in surface structure. The CUR@PDA@DD NPs were further subjected to DOXO loading, which is the next step in the preparation of the drug delivery system.
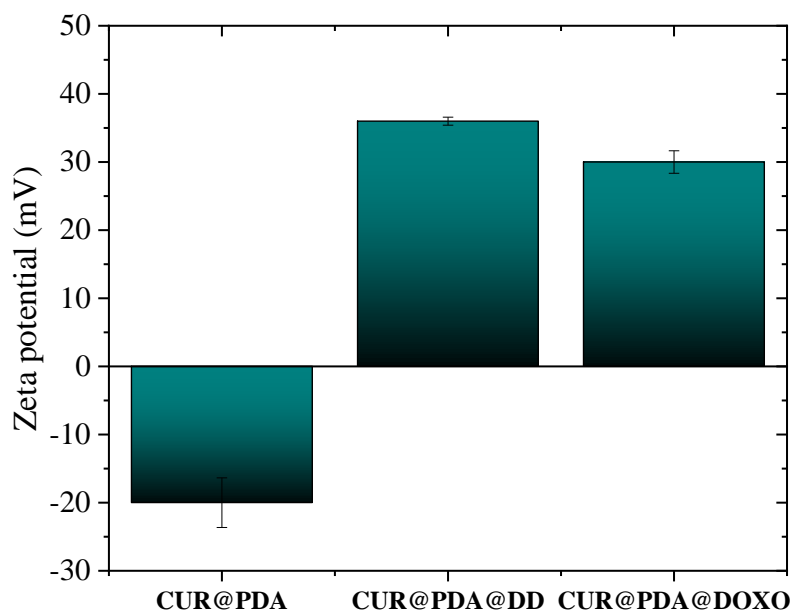
Figure 41. Zeta potential value of pure CUR@PDA NPs, CUR@PDA NPs after functionalization with PAMAM dendrimers and after loading of CUR@PDA NPs with DOXO.

10.1.1. Doxorubicin loading and release

Doxorubicin loading procedure was similar to that of PDA@DD nanoparticles. DOXO was dissolved in PBS buffer pH 7.5 and mixed with CUR@PDA NPs in a 1:1 NPs to DOXO ratio. The sample was incubated for 24 h, at RT in a shaker with a mixing speed of around 300 rpm. The sample was then centrifuged and washed several times with PBS buffer until a clear solution was obtained.

Doxorubicin loading on the CUR@PDA@DD NPs was investigated as previously by UV-Vis spectroscopy method. The amount of DOXO loaded on the CUR@PDA@DD NPs was calculated similarly for the PDA@DD NPs.

Obtained values showed that the loading efficiency of doxorubicin on CUR@PDA@DD NPs is 90% and is slightly lower than for PDA@DD NPs. It was expected because of the smaller value of the zeta potential CUR@PDA. It could affect the attachment of DD on the surface and further smaller volumes for DOXO loading. Also, the zeta potential value of the CUR@PDA@DD nanoparticles compared to the PDA@DD NPs is lower. As with pure PDA@DD NPs, the loading was highly repeatable.

Doxorubicin release experiments from CUR@PDA@DD NPs were performed under artificial conditions using several buffer solutions with pH values between 4.5 – 7.4. First, nanoparticles with a concentration of 1 mg/ml were placed in tubes and then centrifuged. The water in tubes was replaced with 1 ml of the specified buffer, and the samples were collected after 6 h, 24 h and 48 h. All probes were measured using UV-Vis spectroscopy. Based on the calibration curve, the amount of released drug was calculated. The total amount of drug released was calculated as a sum of all measurements for each solution.

CUR@PDA@DD NPs released DOX in a sustained, pH-responsive manner for up to 48 h. The most intense release of DOXO was observed in the first few hours for all

samples, and then reaches equilibrium (**Figure 42**). The cumulative release rate of DOXO at pH 4.5 (11%) was significantly higher than that at pH 5.5 (nearly 4%) and pH 7.4 (3%). This experiments showed that the most effective release occurs in an acidic environment which is present in cancer cells.
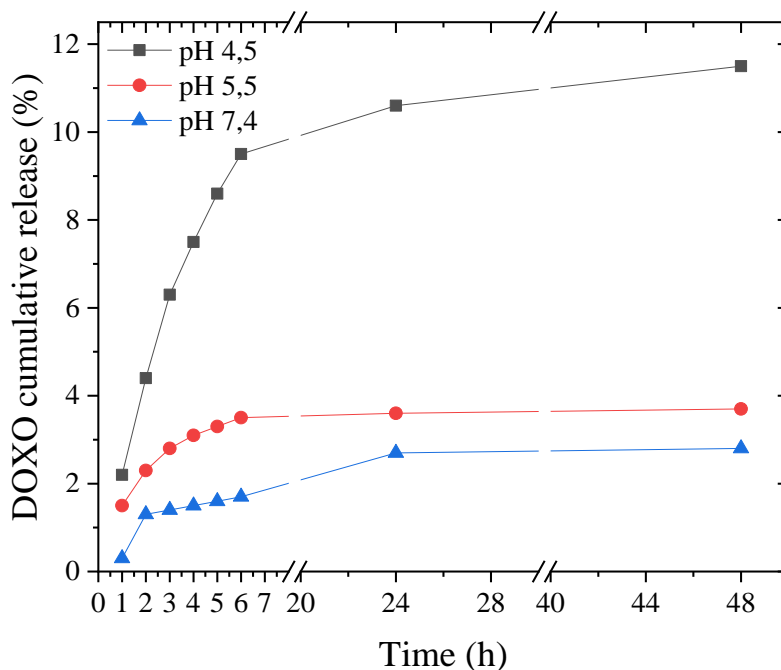
Figure 42. The cumulative release of DOXO from CUR@PDA@DD NPs in pH 4.5, pH 5.5 and pH 7.5 over 48 h at 37 °C.

10.2. Therapy efficiency evaluation

10.2.1. Cytotoxicity

To investigate the applicability of CUR@PDA in tumor therapy, their cytotoxicity after 48 h against HepG2, U118 and MRC-5 cells using the MTT assay was evaluated. The MTT assay was selected to avoid overlapping of signal from CUR and dye. Based on obtained results, it can be conclude that CUR@PDA NPs did not affect the viability of cancer cells. A slight decrease in cell viability was seen only at the highest concentration

for U118 cells, but this change is not statistically significant (**Figure 43 A**). Whereas, HepG2 cell viability remains high for all nanoparticle concentrations (**Figure 43 B**).
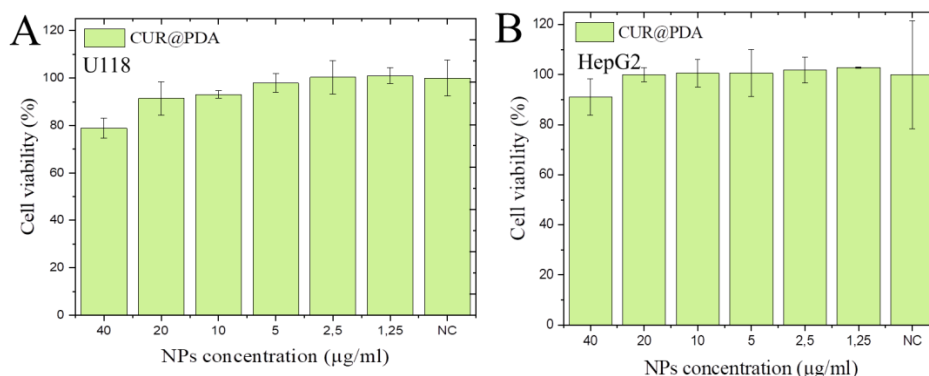
Figure 43. Cell viability results of **A** U118 cells and **B** HepG2 cells after 48 h incubation with pure CUR@PDA NPs obtained using MTT assay. NC: negative control

In addition, MTT assay was also performed on fibroblast cells to check if the pure carrier could affect normal cells in the human body. Based on the obtained results, the carrier itself showed no cytotoxicity in MRC-5 cells (**Figure 44**) at entire concentration range.
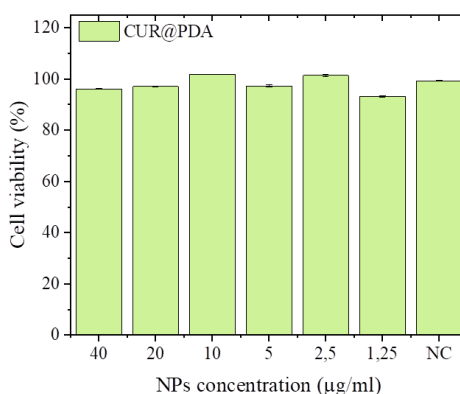
Figure 44. Cell viability results of MRC-5 cells after 48 h incubation with pure CUR@PDA NPs obtained using MTT assay. NC: negative control

To further confirm biocompatibility of pure CUR@PDA NPs and CUR@PDA@DD NPs, fluorescent live/dead assay was performed using high content analysis. This method is complementary to the MTT assay. Tests were performed after 48

h of incubation of U118 (**Figure 45 A, B, C, D**) and HepG2 (**Figure 45 E, F, G, H**) cancer cells with nanoparticles. Images show live (green) and dead (red) cells depending on the concentration of NPs. The cells were counted and the results are presented on the graphs. High cell viability was observed at all concentrations of nanoparticles. This shows that pure carrier is not toxic and the future effect of therapy will result from the therapeutic agent used.
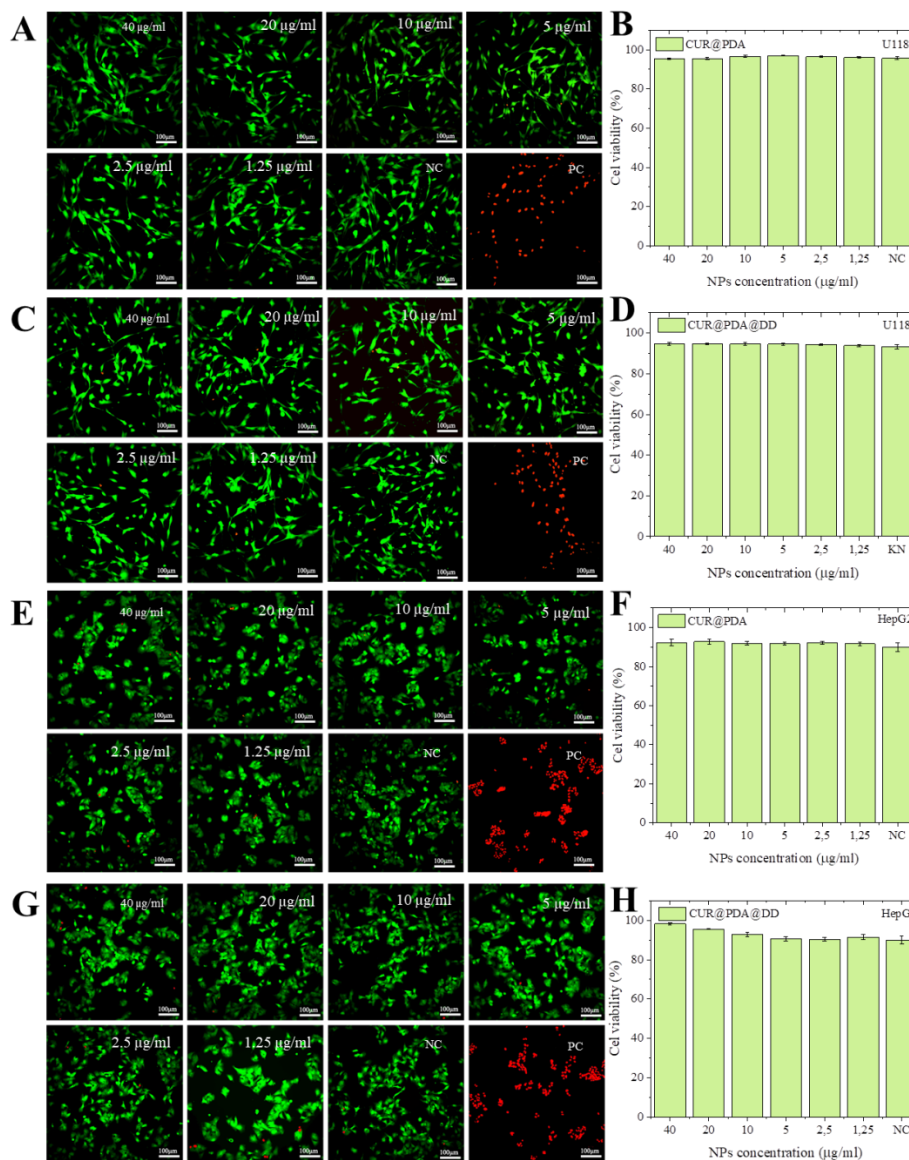
Figure 45. Cell viability of **A, B, C, D** U118 cells and **E, F, G, H** HepG2 cells after 48 h incubation with CUR@PDA NPs and CUR@PDA@DD NPs. NC: negative control (cells without nanoparticles); PC: positive control (cells treated with 0.1% Triton X-100).

10.2.2. Chemotherapy

To investigate the effectiveness of the therapy with CUR@PDA@DD@DOX NPs and quantify live, early, and late apoptosis and cell death, Annexin V assay was performed. The obtained results are presented in **Figure 46** in the form of flow cytometric dot plots and the corresponding graphs.

The results for U118 cells incubated with CUR@PDA@DD@DOXO NPs show dominance of late apoptotic cells, which achieved between 70% and 98% (**Figure 46 A, B**). In contrast, the amount of live cells was significantly decreased. This confirmed that the DOXO was successfully delivered into the cell and the therapy was effective.

In the case of HepG2 cells, after the incubation with CUR@PDA@DD@DOXO, the number of apoptotic cells increased and was proportional to the NPs concentration. The dominance of late and early apoptotic cells was visible, except for the lowest concentration (**Figure 46 C, D**). This may suggest that HepG2 cells are more resistant to therapy with CUR@PDA@DD@DOXO NPs than U118 over the tested concentration range.
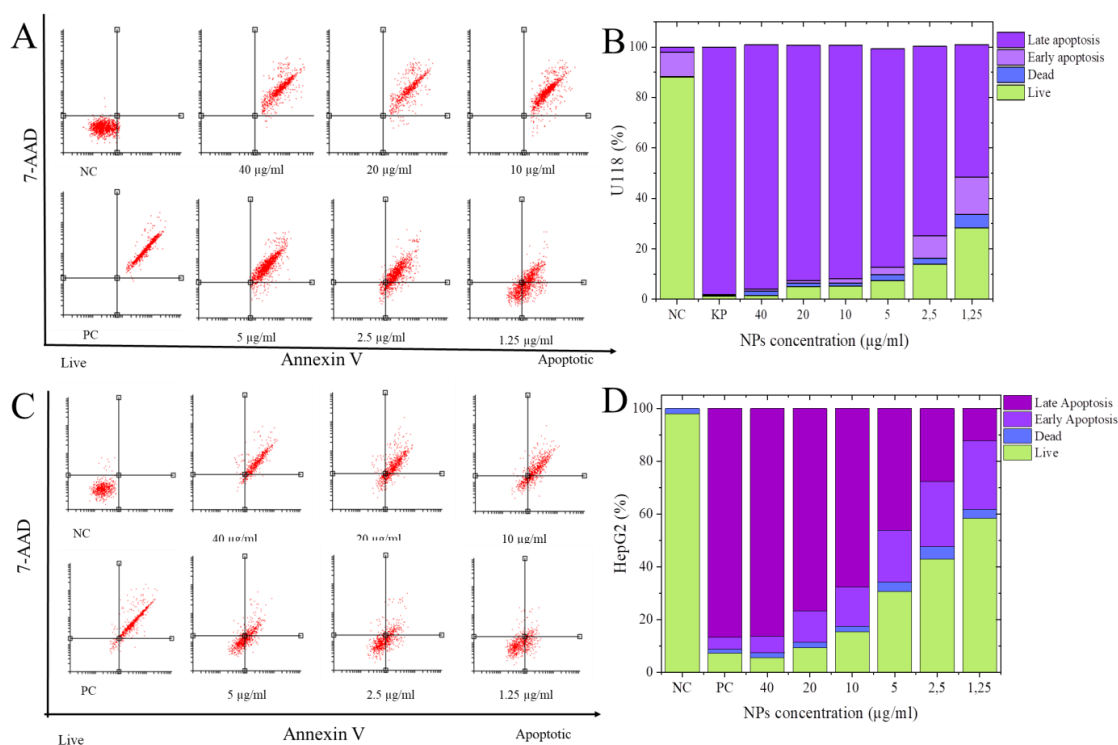
Figure 46. The effectiveness of the therapy with DOXO investigated using Annexin V assay, for U118 cells **A, B** and HepG2 cells **C, D** incubated with CUR@PDA@DD@DOXO over 48 h presented in form of flow cytometer dot plots and corresponding graphs. NC: negative control (cells without nanoparticles), PC: positive control (cells treated with 5 µg/ml DOXO).

In the last step, the uptake of NPs was investigated using confocal imaging. Pure CUR@PDA NPs were used at 10 µg/ml concentrations, while CUR@PDA@DD@DOXO NPs were tested at 10 µg/ml and 5 µg/ml after 4 h of incubation. In cells incubated with CUR@PDA NPs, the signal from the curcumin in the green channel was expected to be seen, which overlaps the doxorubicin signal. However, fluorescence was not visible on the images obtained for both cell lines (**Figure 47, 48**). This may be due to the coating of curcumin by polydopamine, which has a high light absorption capacity. This shows that NPs cannot be followed by fluorescence from CUR in cells as expected.
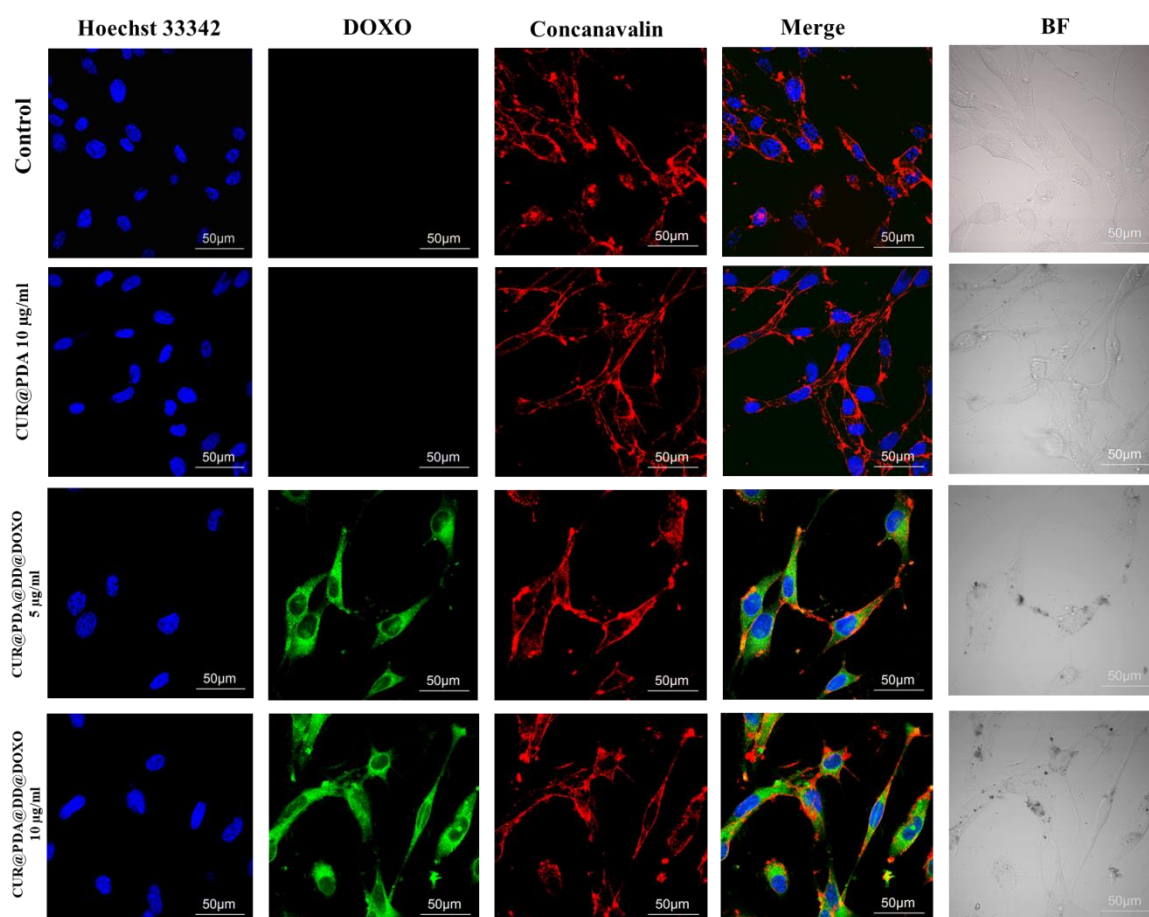
Figure 47. Confocal images showing U118 cells after 4 h incubation with CUR@PDA NPs (10 µg/ml) and CUR@PDA@DD@DOXO NPs (5 µg/ml and 10 µg/ml).

On the other hand, the signal from DOXO was very intense at both concentrations, which confirms very effective delivery by the carrier (**Figure 47, 48**). This may suggest that CUR@PDA@DD NPs efficiently deliver DOXO. The images in bright field mode shows the location of NPs in the cell body.
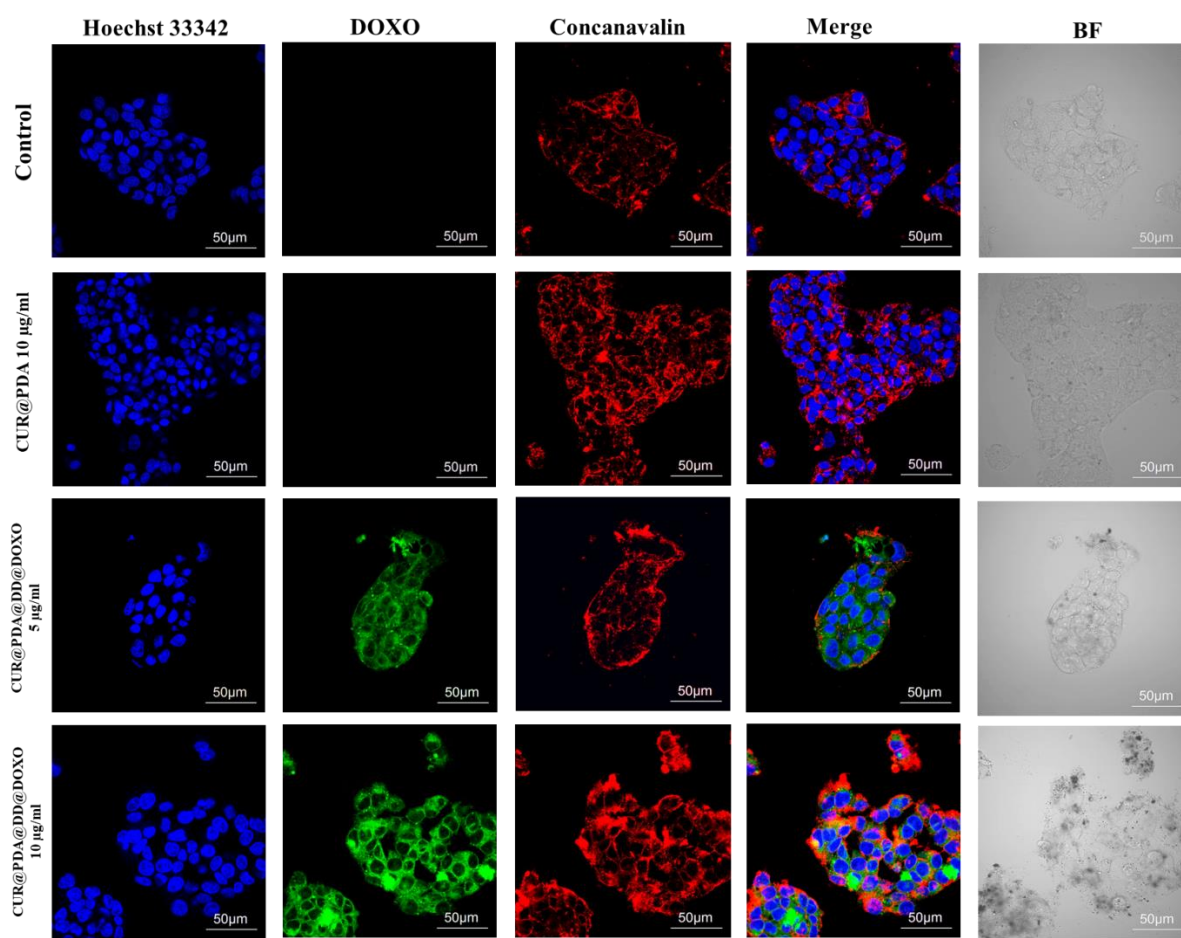
Figure 48. Confocal images showing HepG2 cells after 4 h incubation with CUR@PDA NPs (10 µg/ml) and CUR@PDA@DD@DOXO NPs (5 µg/ml and 10 µg/ml).

10.2.3. Phototherapy

In the last step, the effect of the combined chemo and photothermal therapy was checked. For this purpose, Annexin V assay was used to quantify the number of apoptotic cells. In this case, it was perceived that essential sensitivity on PTT seems to exhibit HepG2 cells (**Figure 49 A, B**). The percent of apoptotic cells is visibly higher in all concentrations than in U118 (**Figure 49 C, D**). After combining the influence of DOXO and PTT the cell viability was reduced almost to 0% in the case of U118 (**Figure 49 G, H**). While in HepG2 the live cells were present in the smallest concentration of NPs (**Figure 49 E, F**).
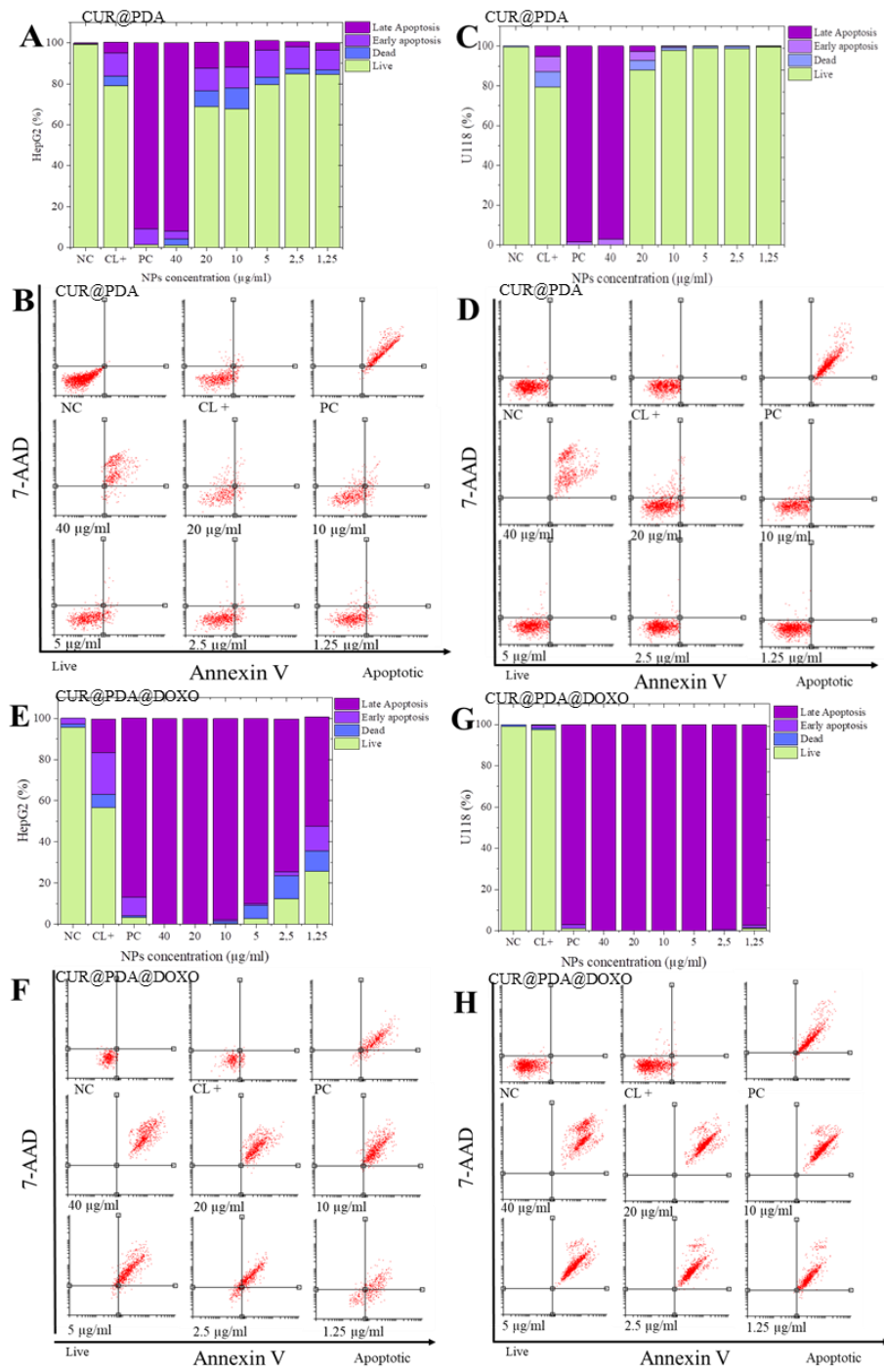
Figure 49. The effectiveness of the PTT therapy and combined therapy with DOXO investigated using Annexin V assay on U118 and HepG2 over 48 h, for **A, B, C, D** CUR@PDA NPs as a control and **E, F, G, H** CUR@PDA@DD@DOXO presented in the form of dot plots from cytometer and calculated data on graphs. NC: negative control (cells without nanoparticles), PC: positive control (cells treated with DOXO), LC+: laser control (cells without nanoparticles after irradiation).

It can be concluded that a carrier with a very high efficiency of DOXO delivery was obtained. However, to fully investigate and understand the effect of CUR on therapy of cancer, a more detailed biological analysis is required. Especially detailed analysis of the pathways, proteins, and ABC transporters involved in the processes that may be affected by curcumin has to be performed. The studies of CUR@PDA nanoparticles presented here have proved that it is a biocompatible carrier with high application potential in multifunctional therapy of cancer.

Conclusions

1. The size of the PDA NPs can be easily controlled by NaOH concentration in the solution. The synthesis of PDA NPs is cheap, fast and highly reproducible.

2. Polydopamine is an effective template for β-FeOOH structure growth under basic conditions as well as for functionalization with PAMAM dendrimers.

3. Polydopamine can be successfully used to coat curcumin and create core-shell nanoparticles.

4. The use of PAMAM dendrimers on PDA and CUR@PDA NPs is characterized by the high efficiency of DOXO loading.

5. PAMAM dendrimers functionalized PDA nanoparticles can efficiently bind nucleic acids (dsRNA). DOXO presence on PDA@DD NPs additionally improves dsRNA attachment.

6. The biggest cumulative release of DOXO from PDA@DD and CUR@PDA@DD NPs is at the pH 4.5, similar to the environment inside the cancer cells. The release of DOXO is extended in time, which can improve treatment efficiency.

7. Curcumin is non-covalently encapsulated in a polydopamine structure and can be easily removed in the presence of ethanol.

8. All synthesized NPs are characterized by high photothermal properties (PT), proving they are sufficient for PT therapy. The presence of β-FeOOH on PDA NPs can additionally improve the PT properties of pure PDA NPs.

9. PDA and CUR@PDA NPs are characterized by high PT stability over 5 on/off cycles of irradiation, which proved that they could be irradiated multiple times.

10. PT stability of PDA@β-FeOOH NPs could not be fully determined because of the low stability of the sample over time and the accumulation of NPs on the magnetic dipole.

11. Confocal imaging confirms the efficient delivery of DOXO using PDA@DD and CUR@PDA@DD NPs into the U118 and HepG2 cells. The accumulation of DOXO is observed in the vicinity of the nuclei.

12. The fluorescence emission from CUR is not visible in cells after incubation with CUR@PDA NPs using confocal microscopy. It can suggest that amount of CUR is not enough to observe the emission or that PDA absorbs the emission.

13. Obtained PDA and CUR@PDA NPs do not exhibit significant cytotoxicity effects in normal (MRC-5) and cancer (HepG2 and U118) cells after incubation over 48 h.

14. The chemotherapeutic effect of PDA@DD@DOX and CUR@PDA@DD@DOX NPs is confirmed by the decrease in cell viability of U118 and HepG2 cells.

15. The phototherapeutic effect of PDA@DD and CUR@PDA@DD NPs is confirmed by a decrease in cell viability of U118 and HepG2 cells, especially at the highest concentration of nanoparticles.

16. The effect of gene therapy of PDA@DD NPs is confirmed by the decrease in tenascin C expression in U118 cells.

17. PDA@β-FeOOH NPs can be a potential material for cancer treatment and imaging. Due to the presence of iron ions, these NPs can be used as contrast agents in MRI and for ferroptosis-dependent cancer cell death. However, both approaches require further investigation.

18. The influence of the synergistic effect of curcumin in combination with doxorubicin using CUR@PDA@DD@DOXO NPs require further investigation.

19. PDA-based carriers are promising drug delivery systems that can be used in combined anticancer therapies.

Bibliography

[1]   M.G. R.W. Kelsall, I.W. Hamley, Nanotechnologie, PWN, Warszawa, 2012.

[2]   Bharat Bhushan, ed., Springer Handbook of Nanotechnology, n.d.

[3]   M. Rafique, M.B. Tahir, M.S. Rafique, N. Safdar, R. Tahir, Nanostructure materials and their classification by dimensionality, Elsevier Inc., 2020. https://doi.org/10.1016/b978-0-12-821192-2.00002-4.

[4]   R. Bawa, What's in a Name? Defining "Nano" in the Context of Drug Delivery, 2020. https://doi.org/10.1201/b19915-14.

[5]   G.E. Naoum, F. Tawadros, A.A. Farooqi, M.Z. Qureshi, S. Tabassum, D.J. Buchsbaum, W. Arafat, Role of nanotechnology and gene delivery systems in TRAIL-based therapies, Ecancermedicalscience. 10 (2016). https://doi.org/10.3332/ecancer.2016.660.

[6]   S.S. Suri, H. Fenniri, B. Singh, Nanotechnology-based drug delivery systems, J. Occup. Med. Toxicol. 2 (2007) 1–6. https://doi.org/10.1186/1745-6673-2-16.

[7]   M.J. Mitchell, M.M. Billingsley, R.M. Haley, M.E. Wechsler, N.A. Peppas, R. Langer, Engineering precision nanoparticles for drug delivery, Nat. Rev. Drug Discov. 20 (2021) 101–124. https://doi.org/10.1038/s41573-020-0090-8.

[8]   H. Kobayashi, R. Watanabe, P.L. Choyke, Improving conventional enhanced permeability and retention (EPR) effects; What is the appropriate target?, Theranostics. 4 (2014) 81–89. https://doi.org/10.7150/thno.7193.

[9]   W. Yang, H. Liang, S. Ma, D. Wang, J. Huang, Gold nanoparticle based photothermal therapy: Development and application for effective cancer treatment, Sustain. Mater. Technol. 22 (2019) e00109. https://doi.org/10.1016/j.susmat.2019.e00109.

[10] J. Wang, A.M. Potocny, J. Rosenthal, E.S. Day, Gold Nanoshell-Linear Tetrapyrrole Conjugates for near Infrared-Activated Dual Photodynamic and Photothermal Therapies, ACS Omega. 5 (2020) 926–940. https://doi.org/10.1021/acsomega.9b04150.

[11] L.S. Arias, J.P. Pessan, A.P.M. Vieira, T.M.T. De Lima, A.C.B. Delbem, D.R. Monteiro, Iron oxide nanoparticles for biomedical applications: A perspective on synthesis, drugs, antimicrobial activity, and toxicity, Antibiotics. 7 (2018). https://doi.org/10.3390/antibiotics7020046.

[12] J.J.M. Cheng Xu†, Jutaek Nam, Hao Hong, Yao Xu, Positron Emission

Tomography-Guided Photodynamic Therapy with Biodegradable Mesoporous Silica Nanoparticles for Personalized Cancer Immunotherapy, ACS Nano. 176 (2019) 139–148. https://doi.org/10.1021/acsnano.9b06691.Data.

[13] B.B. Manshian, J. Jiménez, U. Himmelreich, S.J. Soenen, Personalized medicine and follow-up of therapeutic delivery through exploitation of quantum dot toxicity, Biomaterials. 127 (2017) 1–12. https://doi.org/10.1016/j.biomaterials.2017.02.039.

[14] M. Sarfraz, A. Afzal, T. Yang, Y. Gai, S.M. Raza, M.W. Khan, Y. Cheng, X. Ma, G. Xiang, Development of dual drug loaded nanosized liposomal formulation by a reengineered ethanolic injection method and its pre-clinical pharmacokinetic studies, Pharmaceutics. 10 (2018) 1–22. https://doi.org/10.3390/pharmaceutics10030151.

[15] M. Sedighi, S. Sieber, F. Rahimi, M.A. Shahbazi, A.H. Rezayan, J. Huwyler, D. Witzigmann, Rapid optimization of liposome characteristics using a combined microfluidics and design-of-experiment approach, Drug Deliv. Transl. Res. 9 (2019) 404–413. https://doi.org/10.1007/s13346-018-0587-4.

[16] L. Sercombe, T. Veerati, F. Moheimani, S.Y. Wu, A.K. Sood, S. Hua, Advances and challenges of liposome assisted drug delivery, Front. Pharmacol. 6 (2015) 1–13. https://doi.org/10.3389/fphar.2015.00286.

[17] G.S. Kwon, T. Okano, Polymeric micelles as new drug carriers, Adv. Drug Deliv. Rev. 21 (1996) 107–116. https://doi.org/10.1016/S0169-409X(96)00401-2.

[18] T. Matoba, J. ichiro Koga, K. Nakano, K. Egashira, H. Tsutsui, Nanoparticle-mediated drug delivery system for atherosclerotic cardiovascular disease, J. Cardiol. 70 (2017) 206–211. https://doi.org/10.1016/j.jjcc.2017.03.005.

[19] A. Santos, F. Veiga, A. Figueiras, Dendrimers as pharmaceutical excipients: Synthesis, properties, toxicity and biomedical applications, 2020. https://doi.org/10.3390/ma13010065.

[20] H. Lee, S.M. Dellatore, W.M. Miller, P.B. Messersmith, Mussel-Inspired Surface Chemistry for Multifunctional Coatings, 318 (2008) 426–430. https://doi.org/10.1126/science.1147241.Mussel-Inspired.

[21] N.F. Della Vecchia, A. Luchini, A. Napolitano, G. Derrico, G. Vitiello, N. Szekely, M. Dischia, L. Paduano, Tris buffer modulates polydopamine growth, aggregation, and paramagnetic properties, Langmuir. 30 (2014) 9811–9818. https://doi.org/10.1021/la501560z.

[22] R. Mrowczynski, Polydopamine-Based Multifunctional (Nano)materials for Cancer

Therapy, ACS Appl. Mater. Interfaces. 10 (2018) 7541–7561.
https://doi.org/10.1021/acsami.7b08392.

[23] J.H. Ryu, P.B. Messersmith, H. Lee, Polydopamine Surface Chemistry: A Decade of Discovery, ACS Appl. Mater. Interfaces. 10 (2018) 7523–7540. https://doi.org/10.1021/acsami.7b19865.

[24] S. El Yakhlifi, V. Ball, Polydopamine as a stable and functional nanomaterial, Colloids Surfaces B Biointerfaces. 186 (2020). https://doi.org/10.1016/j.colsurfb.2019.110719.

[25] H.A. Scheidt, C. Filip, R. Turcu, A. Bende, S. Beck, Structure of Polydopamine: A Never-Ending Story?, (2013).

[26] J. Liebscher, Chemistry of Polydopamine – Scope, Variation, and Limitation, European J. Org. Chem. 2019 (2019) 4976–4994. https://doi.org/10.1002/ejoc.201900445.

[27] P. Delparastan, K.G. Malollari, H. Lee, P.B. Messersmith, Direct Evidence for the Polymeric Nature of Polydopamine, Angew. Chemie. 131 (2019) 1089–1094. https://doi.org/10.1002/ange.201811763.

[28] Y. Liu, K. Ai, J. Liu, M. Deng, Y. He, L. Lu, Dopamine-melanin colloidal nanospheres: An efficient near-infrared photothermal therapeutic agent for in vivo cancer therapy, Adv. Mater. 25 (2013) 1353–1359. https://doi.org/10.1002/adma.201204683.

[29] S. Mei, X. Xu, R.D. Priestley, Y. Lu, Polydopamine-based nanoreactors: Synthesis and applications in bioscience and energy materials, Chem. Sci. 11 (2020) 12269–12281. https://doi.org/10.1039/d0sc04486e.

[30] N.F. Della Vecchia, R. Avolio, M. Alfè, M.E. Errico, A. Napolitano, M. D'Ischia, Building-block diversity in polydopamine underpins a multifunctional eumelanin-type platform tunable through a quinone control point, Adv. Funct. Mater. 23 (2013) 1331–1340. https://doi.org/10.1002/adfm.201202127.

[31] C.C. Ho, S.J. Ding, Structure, properties and applications of mussel-inspired polydopamine, J. Biomed. Nanotechnol. 10 (2014) 3063–3084. https://doi.org/10.1166/jbn.2014.1888.

[32] G. Shu, M. Chen, J. Song, X. Xu, C. Lu, Y. Du, M. Xu, Z. Zhao, M. Zhu, K. Fan, X. Fan, S. Fang, B. Tang, Y. Dai, Y. Du, J. Ji, Sialic acid-engineered mesoporous polydopamine nanoparticles loaded with SPIO and Fe3+ as a novel theranostic agent for T1/T2 dual-mode MRI-guided combined chemo-photothermal treatment of

hepatic cancer, Bioact. Mater. 6 (2021) 1423–1435.
https://doi.org/10.1016/j.bioactmat.2020.10.020.

[33] R. Mrówczyński, L.E. Coy, B. Scheibe, T. Czechowski, M. Augustyniak-Jabłokow, S. Jurga, K. Tadyszak, Electron Paramagnetic Resonance Imaging and Spectroscopy of Polydopamine Radicals, J. Phys. Chem. B. 119 (2015) 10341–10347. https://doi.org/10.1021/acs.jpcb.5b01524.

[34] Cancer treatment options, (n.d.). https://www.houstonmethodist.org/cancer/treatment-options/.

[35] C. Carvalho, R. Santos, S. Cardoso, S. Correia, P. Oliveira, M. Santos, P. Moreira, Doxorubicin: The Good, the Bad and the Ugly Effect, Curr. Med. Chem. 16 (2009) 3267–3285. https://doi.org/10.2174/092986709788803312.

[36] G.N. Naumov, J.L. Townson, I.C. MacDonald, S.M. Wilson, V.H.C. Bramwell, A.C. Groom, A.F. Chambers, Ineffectiveness of doxorubicin treatment on solitary dormant mammary carcinoma cells or late-developing metastases, Breast Cancer Res. Treat. 82 (2003) 199–206. https://doi.org/10.1023/B:BREA.0000004377.12288.3c.

[37] B. Gnapareddy, S. Reddy Dugasani, T. Ha, B. Paulson, T. Hwang, T. Kim, J. Hoon Kim, K. Oh, S.H. Park, Chemical and Physical Characteristics of Doxorubicin Hydrochloride Drug-Doped Salmon DNA Thin Films, Sci. Rep. 5 (2015) 1–9. https://doi.org/10.1038/srep12722.

[38] K. Mansouri, S. Rasoulpoor, A. Daneshkhah, S. Abolfathi, N. Salari, M. Mohammadi, S. Rasoulpoor, S. Shabani, Clinical effects of curcumin in enhancing cancer therapy: A systematic review, BMC Cancer. 20 (2020) 1–11. https://doi.org/10.1186/s12885-020-07256-8.

[39] A. Goel, A.B. Kunnumakkara, B.B. Aggarwal, Curcumin as "Curecumin": From kitchen to clinic, Biochem. Pharmacol. 75 (2008) 787–809. https://doi.org/10.1016/j.bcp.2007.08.016.

[40] A.H. El-Far, N.H.E. Darwish, S.A. Mousa, Senescent Colon and Breast Cancer Cells Induced by Doxorubicin Exhibit Enhanced Sensitivity to Curcumin, Caffeine, and Thymoquinone, Integr. Cancer Ther. 19 (2020). https://doi.org/10.1177/1534735419901160.

[41] S. Shaker, J. Sang, X.L. Yan, R.Z. Fan, G.H. Tang, Y.K. Xu, S. Yin, Diterpenoids from Euphorbia royleana reverse P-glycoprotein-mediated multidrug resistance in cancer cells, Phytochemistry. 176 (2020) 112395.

https://doi.org/10.1016/j.phytochem.2020.112395.

[42] L. Yang, D. Li, P. Tang, Y. Zuo, Curcumin increases the sensitivity of K562/DOX cells to doxorubicin by targeting S100 calcium-binding protein A8 and P-glycoprotein, Oncol. Lett. 19 (2020) 83–92. https://doi.org/10.3892/ol.2019.11083.

[43] M.J. Hsieh, C.W. Lin, S.C. Su, R.J. Reiter, A.W.G. Chen, M.K. Chen, S.F. Yang, Effects of miR-34b/miR-892a Upregulation and Inhibition of ABCB1/ABCB4 on Melatonin-Induced Apoptosis in VCR-Resistant Oral Cancer Cells, Mol. Ther. - Nucleic Acids. 19 (2020) 877–889. https://doi.org/10.1016/j.omtn.2019.12.022.

[44] C. Wen, L. Fu, J. Huang, Y. Dai, B. Wang, G. Xu, L. Wu, H. Zhou, Curcumin reverses doxorubicin resistance via inhibition the efflux function of ABCB4 in doxorubicin-resistant breast cancer cells, Mol. Med. Rep. 19 (2019) 5162–5168. https://doi.org/10.3892/mmr.2019.10180.

[45] M. Ashrafizadeh, A. Zarrabi, F. Hashemi, E.R. Moghadam, F. Hashemi, M. Entezari, K. Hushmandi, R. Mohammadinejad, M. Najafi, Curcumin in cancer therapy: A novel adjunct for combination chemotherapy with paclitaxel and alleviation of its adverse effects, Life Sci. 256 (2020) 117984. https://doi.org/10.1016/j.lfs.2020.117984.

[46] S. Wong, J. Zhao, C. Cao, C.K. Wong, R.P. Kuchel, S. De Luca, J.M. Hook, C.J. Garvey, S. Smith, J. Ho, M.H. Stenzel, Just add sugar for carbohydrate induced self-assembly of curcumin, Nat. Commun. 10 (2019) 1–9. https://doi.org/10.1038/s41467-019-08402-y.

[47] H. Pan, X. Shen, W. Tao, S. Chen, X. Ye, Fabrication of Polydopamine-Based Curcumin Nanoparticles for Chemical Stability and pH-Responsive Delivery, J. Agric. Food Chem. 68 (2020) 2795–2802. https://doi.org/10.1021/acs.jafc.9b07697.

[48] L. Zhao, D. Bi, X. Qi, Y. Guo, F. Yue, X. Wang, M. Han, Polydopamine-based surface modification of paclitaxel nanoparticles for osteosarcoma targeted therapy, Nanotechnology. 30 (2019). https://doi.org/10.1088/1361-6528/ab055f.

[49] Z. Meng, Y. Liu, K. Xu, X. Sun, Q. Yu, Z. Wu, Z. Zhao, Biomimetic Polydopamine-Modified Silk Fibroin/Curcumin Nanofibrous Scaffolds for Chemo-photothermal Therapy of Bone Tumor, ACS Omega. 6 (2021) 22213–22223. https://doi.org/10.1021/acsomega.1c02903.

[50] US FDA, Long Term Follow-Up After Administration of Human Gene Therapy Products Draft Guidance for Industry, Us Fda. (2020) 1–37.

https://www.fda.gov/BiologicsBloodVaccines/GuidanceComplianceRegulatoryInfor mation/Guid.

[51] G.A.R. Gonçalves, R. de M.A. Paiva, Gene therapy: advances, challenges and perspectives, Einstein (Sao Paulo). 15 (2017) 369–375. https://doi.org/10.1590/S1679-45082017RB4024.

[52] J.T. Bulcha, Y. Wang, H. Ma, P.W.L. Tai, G. Gao, Viral vector platforms within the gene therapy landscape, Signal Transduct. Target. Ther. 6 (2021). https://doi.org/10.1038/s41392-021-00487-6.

[53] L. Duan, K. Ouyang, X. Xu, L. Xu, C. Wen, X. Zhou, Z. Qin, Z. Xu, W. Sun, Y. Liang, Nanoparticle Delivery of CRISPR/Cas9 for Genome Editing, Front. Genet. 12 (2021). https://doi.org/10.3389/fgene.2021.673286.

[54] J. Pas, E. Wyszko, K. Rolle, L. Rychlewski, S. Nowak, R. Zukiel, J. Barciszewski, Analysis of structure and function of tenascin-C, Int. J. Biochem. Cell Biol. 38 (2006) 1594–1602. https://doi.org/10.1016/j.biocel.2006.03.017.

[55] K.S. Midwood, G. Orend, The role of tenascin-C in tissue injury and tumorigenesis, J. Cell Commun. Signal. 3 (2009) 287–310. https://doi.org/10.1007/s12079-009-0075-1.

[56] M. Grabowska, B.F. Grześkowiak, K. Szutkowski, D. Wawrzyniak, P. Głodowicz, J. Barciszewski, S. Jurga, K. Rolle, R. Mrówczyński, Nano-mediated delivery of double-stranded RNA for gene therapy of glioblastoma multiforme, PLoS One. 14 (2019) 1–21. https://doi.org/10.1371/journal.pone.0213852.

[57] D. Wawrzyniak, M. Grabowska, P. Głodowicz, K. Kuczyński, B. Kuczyńska, A. Fedoruk-Wyszomirska, K. Rolle, Down-regulation of tenascin-C inhibits breast cancer cells development by cell growth, migration, and adhesion impairment, PLoS One. 15 (2020) 1–25. https://doi.org/10.1371/journal.pone.0237889.

[58] Z. Wang, L. Wang, N. Prabhakar, Y. Xing, J.M. Rosenholm, J. Zhang, K. Cai, CaP coated mesoporous polydopamine nanoparticles with responsive membrane permeation ability for combined photothermal and siRNA therapy, Acta Biomater. 86 (2019) 416–428. https://doi.org/10.1016/j.actbio.2019.01.002.

[59] P. Zhang, Q. Xu, X. Li, Y. Wang, pH-responsive polydopamine nanoparticles for photothermally promoted gene delivery, Mater. Sci. Eng. C. 108 (2020) 110396. https://doi.org/10.1016/j.msec.2019.110396.

[60] H. Zhao, Z. Zhang, D. Zuo, L. Li, F. Li, D. Yang, A Synergistic DNA-polydopamine-MnO2Nanocomplex for Near-Infrared-Light-Powered DNAzyme-

Mediated Gene Therapy, Nano Lett. 21 (2021) 5377–5385. https://doi.org/10.1021/acs.nanolett.1c01727.

[61] L.R. Hirsch, R.J. Stafford, J.A. Bankson, S.R. Sershen, B. Rivera, R.E. Price, J.D. Hazle, N.J. Halas, J.L. West, Nanoshell-mediated near-infrared thermal therapy of tumors under magnetic resonance guidance, Proc. Natl. Acad. Sci. U. S. A. 100 (2003) 13549–13554. https://doi.org/10.1073/pnas.2232479100.

[62] D. Zhi, T. Yang, J. O'Hagan, S. Zhang, R.F. Donnelly, Photothermal therapy, J. Control. Release. 325 (2020) 52–71. https://doi.org/10.1016/j.jconrel.2020.06.032.

[63] M.F. Tsai, S.H.G. Chang, F.Y. Cheng, V. Shanmugam, Y.S. Cheng, C.H. Su, C.S. Yeh, Au nanorod design as light-absorber in the first and second biological near-infrared windows for in vivo photothermal therapy, ACS Nano. 7 (2013) 5330–5342. https://doi.org/10.1021/nn401187c.

[64] Y. Zhang, S. Zhang, Z. Zhang, L. Ji, J. Zhang, Q. Wang, T. Guo, S. Ni, R. Cai, X. Mu, W. Long, H. Wang, Recent Progress on NIR-II Photothermal Therapy, Front. Chem. 9 (2021) 1–26. https://doi.org/10.3389/fchem.2021.728066.

[65] M. Pérez-Hernández, P. Del Pino, S.G. Mitchell, M. Moros, G. Stepien, B. Pelaz, W.J. Parak, E.M. Gálvez, J. Pardo, J.M. De La Fuente, Dissecting the molecular mechanism of apoptosis during photothermal therapy using gold nanoprisms, ACS Nano. 9 (2015) 52–61. https://doi.org/10.1021/nn505468v.

[66] J.R. Melamed, R.S. Edelstein, E.S. Day, Elucidating the fundamental mechanisms of cell death triggered by photothermal therapy, ACS Nano. 9 (2015) 6–11. https://doi.org/10.1021/acsnano.5b00021.

[67] Y.J. Hou, X.X. Yang, R.Q. Liu, D. Zhao, C.X. Guo, A.C. Zhu, M.N. Wen, Z. Liu, G.F. Qu, H.X. Meng, Pathological mechanism of photodynamic therapy and photothermal therapy based on nanoparticles, Int. J. Nanomedicine. 15 (2020) 6827–6838. https://doi.org/10.2147/IJN.S269321.

[68] T. Dai, B.B. Fuchs, J.J. Coleman, R.A. Prates, C. Astrakas, T.G. St. Denis, M.S. Ribeiro, E. Mylonakis, M.R. Hamblin, G.P. Tegos, Concepts and principles of photodynamic therapy as an alternative antifungal discovery platform, Front. Microbiol. 3 (2012). https://doi.org/10.3389/fmicb.2012.00120.

[69] S. Liu, X. Pan, H. Liu, Two-Dimensional Nanomaterials for Photothermal Therapy, Adv. Mater. 132 (2020) 5943–5953. https://doi.org/10.1002/ANGE.201911477.

[70] Y. Liu, P. Bhattarai, Z. Dai, X. Chen, Photothermal therapy and photoacoustic imaging: Via nanotheranostics in fighting cancer, Chem. Soc. Rev. 48 (2019) 2053–

2108. https://doi.org/10.1039/c8cs00618k.

[71] B.F. Grześkowiak, D. Maziukiewicz, A. Kozłowska, A. Kertmen, E. Coy, R. Mrówczyński, Polyamidoamine dendrimers decorated multifunctional polydopamine nanoparticles for targeted chemo-and photothermal therapy of liver cancer model, Int. J. Mol. Sci. 22 (2021) 1–16. https://doi.org/10.3390/ijms22020738.

[72] A. Jędrzak, B.F. Grześkowiak, K. Golba, E. Coy, K. Synoradzki, S. Jurga, T. Jesionowski, R. Mrówczyński, Magnetite nanoparticles and spheres for chemo-and photothermal therapy of hepatocellular carcinoma in vitro, Int. J. Nanomedicine. 15 (2020) 7923–7936. https://doi.org/10.2147/IJN.S257142.

[73] B. Poinard, S.Z.Y. Neo, E.L.L. Yeo, H.P.S. Heng, K.G. Neoh, J.C.Y. Kah, Polydopamine Nanoparticles Enhance Drug Release for Combined Photodynamic and Photothermal Therapy, ACS Appl. Mater. Interfaces. 10 (2018) 21125–21136. https://doi.org/10.1021/acsami.8b04799.

[74] Z.H. Miao, H. Wang, H. Yang, Z.L. Li, L. Zhen, C.Y. Xu, Intrinsically Mn2+-Chelated Polydopamine Nanoparticles for Simultaneous Magnetic Resonance Imaging and Photothermal Ablation of Cancer Cells, ACS Appl. Mater. Interfaces. 7 (2015) 16946–16952. https://doi.org/10.1021/acsami.5b06265.

[75] K.C.L. Black, J. Yi, J.G. Rivera, D.C. Zelasko-Leon, P.B. Messersmith, Polydopamine-enabled surface functionalization of gold nanorods for cancer cell-targeted imaging and photothermal therapy, Nanomedicine. 8 (2013) 17–28. https://doi.org/10.2217/nnm.12.82.

[76] D. Maziukiewicz, B.F. Grześkowiak, E. Coy, S. Jurga, R. Mrówczyński, NDs@PDA@ICG conjugates for photothermal therapy of glioblastoma multiforme, Biomimetics. 4 (2019) 1–17. https://doi.org/10.3390/biomimetics4010003.

[77] T. Chemicznej, U.M. Curie-sk, Rozdział ELEKTRONOWEJ I JEJ WYBRANE W CHARAKTERYSTYCE, (n.d.) 20–31.

[78] C.C. Ho, S.J. Ding, The pH-controlled nanoparticles size of polydopamine for anti-cancer drug delivery, J. Mater. Sci. Mater. Med. 24 (2013) 2381–2390. https://doi.org/10.1007/s10856-013-4994-2.

[79] R. Tejido-Rastrilla, S. Ferraris, W.H. Goldmann, A. Grünewald, R. Detsch, G. Baldi, S. Spriano, A.R. Boccaccini, Studies on cell compatibility, antibacterial behavior, and zeta potential of Ag-containing polydopamine-coated bioactive glass-ceramic, Materials (Basel). 12 (2019). https://doi.org/10.3390/ma12030500.

[80] F. Bernsmann, B. Frisch, C. Ringwald, V. Ball, Protein adsorption on dopamine-melanin films: Role of electrostatic interactions inferred from ζ-potential measurements versus chemisorption, J. Colloid Interface Sci. 344 (2010) 54–60. https://doi.org/10.1016/j.jcis.2009.12.052.

[81] J. Fu, Z. Chen, M. Wang, S. Liu, J. Zhang, J. Zhang, R. Han, Q. Xu, Adsorption of methylene blue by a high-efficiency adsorbent (polydopamine microspheres): Kinetics, isotherm, thermodynamics and mechanism analysis, Chem. Eng. J. 259 (2015) 53–61. https://doi.org/10.1016/j.cej.2014.07.101.

[82] L. Su, Y. Yu, Y. Zhao, F. Liang, X. Zhang, Strong Antibacterial Polydopamine Coatings Prepared by a Shaking-assisted Method, Sci. Rep. 6 (2016) 1–8. https://doi.org/10.1038/srep24420.

[83] V. Ball, Impedance spectroscopy and zeta potential titration of dopa-melanin films produced by oxidation of dopamine, Colloids Surfaces A Physicochem. Eng. Asp. 363 (2010) 92–97. https://doi.org/10.1016/j.colsurfa.2010.04.020.

[84] H. Luo, C. Gu, W. Zheng, F. Dai, X. Wang, Z. Zheng, Facile synthesis of novel size-controlled antibacterial hybrid spheres using silver nanoparticles loaded with poly-dopamine spheres, RSC Adv. 5 (2015) 13470–13477. https://doi.org/10.1039/c4ra16469e.

[85] K. Żebrowska, E. Coy, K. Synoradzki, S. Jurga, P. Torruella, R. Mrówczyński, Facile and Controllable Growth of β-FeOOH Nanostructures on Polydopamine Spheres, J. Phys. Chem. B. 124 (2020) 9456–9463. https://doi.org/10.1021/acs.jpcb.0c06627.

[86] C. Zhang, H.C. Yang, L.S. Wan, H.Q. Liang, H. Li, Z.K. Xu, Polydopamine-coated porous substrates as a platform for mineralized β-FeOOH Nanorods with Photocatalysis under Sunlight, ACS Appl. Mater. Interfaces. 7 (2015) 11567–11574. https://doi.org/10.1021/acsami.5b02530.

[87] D. Cheng, Y. Zhang, X. Bai, Y. Liu, Z. Deng, J. Wu, S. Bi, J. Ran, G. Cai, X. Wang, Mussel-inspired fabrication of superhydrophobic cotton fabric for oil/water separation and visible light photocatalytic, Cellulose. 0123456789 (2020). https://doi.org/10.1007/s10570-020-03149-y.

[88] P. Ewels, T. Sikora, V. Serin, C.P. Ewels, L. Lajaunie, A Complete Overhaul of the Electron Energy-Loss Spectroscopy and X-Ray Absorption Spectroscopy Database: eelsdb.eu, Microsc. Microanal. 22 (2016) 717–724. https://doi.org/10.1017/S1431927616000179.

[89] P. Veverka, M. Pashchenko, L. Kubíčková, J. Kuličková, Z. Jirák, R. Havelek, K. Královec, J. Kohout, O. Kaman, Rod-like particles of silica-coated maghemite: Synthesis via akaganeite, characterization and biological properties, J. Magn. Magn. Mater. 476 (2019) 149–156. https://doi.org/10.1016/j.jmmm.2018.12.037.

[90] A. Urtizberea, F. Luis, A. Millán, E. Natividad, F. Palacio, E. Kampert, U. Zeitler, Thermoinduced magnetic moment in akaganéite nanoparticles, Phys. Rev. B - Condens. Matter Mater. Phys. 83 (2011) 1–7. https://doi.org/10.1103/PhysRevB.83.214426.

[91] J.Y. Cao, S.J. Dixon, Mechanisms of ferroptosis, Cell. Mol. Life Sci. 73 (2016) 2195–2209. https://doi.org/10.1007/s00018-016-2194-1.

[92] Y. Xie, W. Hou, X. Song, Y. Yu, J. Huang, X. Sun, R. Kang, D. Tang, Ferroptosis: Process and function, Cell Death Differ. 23 (2016) 369–379. https://doi.org/10.1038/cdd.2015.158.

[93] J. Li, F. Cao, H. liang Yin, Z. jian Huang, Z. tao Lin, N. Mao, B. Sun, G. Wang, Ferroptosis: past, present and future, Cell Death Dis. 11 (2020). https://doi.org/10.1038/s41419-020-2298-2.

[94] J. Kulbacka, J. Saczko, A. Chwilkowska, Stres oksydacyjny w procesach uszkodzenia komórek, Pol. Merkur. Lek. 27 (2009) 44–47.

[95] J. Xue, W. Zheng, L. Wang, Z. Jin, Scalable Fabrication of Polydopamine Nanotubes Based on Curcumin Crystals, ACS Biomater. Sci. Eng. 2 (2016) 489–493. https://doi.org/10.1021/acsbiomaterials.6b00102.

[96] X. Jiang, Y. Wang, M. Li, Selecting water-alcohol mixed solvent for synthesis of polydopamine nano-spheres using solubility parameter, Sci. Rep. 4 (2014) 15–18. https://doi.org/10.1038/srep06070.

[97] P.R.K. Mohan, G. Sreelakshmi, C. V. Muraleedharan, R. Joseph, Water soluble complexes of curcumin with cyclodextrins: Characterization by FT-Raman spectroscopy, Vib. Spectrosc. 62 (2012) 77–84. https://doi.org/10.1016/j.vibspec.2012.05.002.

[98] E.H. Ismail, D.Y. Sabry, H. Mahdy, M.M.H. Khalil, Synthesis and Characterization of some Ternary Metal Complexes of Curcumin with 1,10-phenanthroline and their Anticancer Applications, J. Sci. Res. 6 (2014) 509–519. https://doi.org/10.3329/jsr.v6i3.18750.

[99] R. Su, H. Yan, P. Li, B. Zhang, Y. Zhang, W. Su, Photo-enhanced antibacterial activity of polydopamine-curcumin nanocomposites with excellent photodynamic

and photothermal abilities, Photodiagnosis Photodyn. Ther. 35 (2021) 102417. https://doi.org/10.1016/j.pdpdt.2021.102417.

[100] X. Chen, L.Q. Zou, J. Niu, W. Liu, S.F. Peng, C.M. Liu, The stability, sustained release and cellular antioxidant activity of curcumin nanoliposomes, Molecules. 20 (2015) 14293–14311. https://doi.org/10.3390/molecules200814293.

[101] X. Chen, W. Yang, J. Zhang, L. Zhang, H. Shen, D. Shi, Alkalinity triggered the degradation of polydopamine nanoparticles, Polym. Bull. 78 (2021) 4439–4452. https://doi.org/10.1007/s00289-020-03312-2.

[102] S.V.K. Rompicharla, H. Bhatt, A. Shah, N. Komanduri, D. Vijayasarathy, B. Ghosh, S. Biswas, Formulation optimization, characterization, and evaluation of in vitro cytotoxic potential of curcumin loaded solid lipid nanoparticles for improved anticancer activity, Chem. Phys. Lipids. 208 (2017) 10–18. https://doi.org/10.1016/j.chemphyslip.2017.08.009.

[103] L. Mayol, C. Serri, C. Menale, S. Crispi, M.T. Piccolo, L. Mita, S. Giarra, M. Forte, A. Saija, M. Biondi, D.G. Mita, Curcumin loaded PLGA-poloxamer blend nanoparticles induce cell cycle arrest in mesothelioma cells, Eur. J. Pharm. Biopharm. 93 (2015) 37–45. https://doi.org/10.1016/j.ejpb.2015.03.005.

[104] D. Guzman-Villanueva, I.M. El-Sherbiny, D. Herrera-Ruiz, H.D.C. Smyth, Design and in vitro evaluation of a new nano-microparticulate system for enhanced aqueous-phase solubility of curcumin, Biomed Res. Int. 2013 (2013). https://doi.org/10.1155/2013/724763.

List of Tables